Late Visean to Bashkirian Platform Cyclicity in the Central Tengiz Buildup, Precaspian Basin, Kazakhstan: Depositional Evolution and Reservoir Development

Chapter *in* AAPG Memoir · January 2006

DOI: 10.1306/1215873M88374

CITATIONS
57

READS
1,208

6 authors, including:

Jeroen Kenter
TOTAL Pau, France
111 PUBLICATIONS **3,266** CITATIONS

SEE PROFILE

1

Kenter, J. A. M., P. M. Harris, J. F. Collins, L. J. Weber, G. Kuanysheva, and D. J. Fischer, 2006, Late Visean to Bashkirian platform cyclicity in the central Tengiz buildup, Precaspian Basin, Kazakhstan: Depositional evolution and reservoir development, *in* P. M. Harris and L. J. Weber, eds., Giant hydrocarbon reservoirs of the world: From rocks to reservoir characterization and modeling: AAPG Memoir 88/SEPM Special Publication, p. 7–54.

Late Visean to Bashkirian Platform Cyclicity in the Central Tengiz Buildup, Precaspian Basin, Kazakhstan: Depositional Evolution and Reservoir Development

J. A. M. Kenter[1]
Vrije Universiteit, Amsterdam, Netherlands

P. M. Harris
Chevron Energy Technology Company, San Ramon, California, U.S.A.

J. F. Collins
ExxonMobil Development Company, Houston, Texas, U.S.A.

L. J. Weber
ExxonMobil Development Company, Houston, Texas, U.S.A.

G. Kuanysheva
TengizChevroil, Atyrau, Kazakhstan

D. J. Fischer
TengizChevroil, Atyrau, Kazakhstan

ABSTRACT

The Tengiz buildup, an intensely cored and studied isolated carbonate platform in the Precaspian Basin, contains a succession of shallow-water deposits ranging from Famennian to Bashkirian in age. From a reservoir perspective, Tengiz can be subdivided into platform (central and outer) and rim-slope (flank) regions. The upper Visean, Serpukhovian, and Bashkirian form the main hydrocarbon-bearing interval in the platform. Depositional cycles (high-frequency sequences) in this interval are several to tens of meters thick for the Visean and Serpukhovian, and decimeter to meter scale for the Bashkirian. Cycles are made up of a succession of lithofacies overlying a sharp base that locally shows erosion, calcretes, meteoric diagenesis, and other evidence for subaerial exposure. At the base of the succession, tight peloidal mudstone and ash beds are associated with sequence boundaries and are thought to reflect low-energy conditions developed in deeper platform areas at lowstand and during

[1] *Present address*: Chevron Energy Technology Company, San Ramon, California, U.S.A.

DOI:10.1306/1215873M88374

initial flooding. Above this, beds with in-situ articulated brachiopods signal initial open-marine but still low-energy conditions. Succeeding crinoid-dominated intervals represent maximum marine flooding and overlying skeletal-peloidal grainstones highstand shoaling phases.

Visean and Serpukhovian cycles are generally easy to correlate from well to well over several kilometers distance. Volcanic ash beds are identified by gamma-ray spikes, and flooding intervals show as low-porosity zones. In contrast, Bashkirian cycles are thinner and incomplete, dominated by thin, peloidal mudstone intervals alternating with high-energy coated-grain and ooid grainstone, and are more difficult to correlate. High-frequency icehouse sea level fluctuations exposed the platform during each fall of sea level, and rapid flooding resulted in incomplete cycles and complex lateral facies changes that may explain relatively poor lateral continuity of log character.

The distribution of reservoir rock types in the central platform is determined by burial diagenetic modification of an earlier reservoir system that includes meteoric alteration and porosity enhancement below major sequence boundaries and reduced dissolution along higher order sequence boundaries associated with the presence of volcanic ash. The lateral continuity of tight layers at sequence boundaries probably greatly affected later fluid flow as well as the ultimate distribution of cements, dissolution, and bitumen in the central platform reservoir.

The burial diagenetic overprint included two major phases of reservoir modification. First, a corrosion and cementation phase significantly enhanced existing matrix porosity in the interior central platform while reducing porosity in the exterior central and outer platform by pore-filling equant calcite cement. This was followed by bitumen emplacement and associated corrosion. These processes not only exerted an overall porosity-reducing effect prior to and associated with bitumen invasion toward the exterior central platform, but also dampened or flattened the initial cyclic porosity variations and obscured relationships between pore types and permeability. The bitumen overprint is nearly absent in the innermost platform wells; bitumen concentrations are highest near the bases of the cycles, which may imply that the first fill of hydrocarbons migrated through the flanks laterally into the platform cycles.

INTRODUCTION

Tengiz Field History

The Tengiz field, located in western Kazakhstan, near the northeastern shore of the Caspian Sea (Figure 1), produces oil from an isolated carbonate platform (aerial extent of >110 km^2 [42 mi^2]) of Devonian and Carboniferous age. Tengiz was discovered in 1979 by the Ministry of Oil Industry of the Soviet Union. The discovery well Tengiz 1 (T-1) reached a total depth of 4095 m (13,435 ft). Development drilling of the Tengiz field commenced in 1983, and onsite construction of plant-processing facilities began in 1987. Field production officially began in April 1991. Since 1993, TengizChevroil, an in-country joint venture company run by Chevron, has operated Tengiz and the adjacent Korolev field.

Tengiz field produces a light, intermediate-sulfur, stabilized tank oil of approximately 47° API. As of mid-year 2005, more than 115 wells have been drilled on Tengiz. The highest rate wells are located in the platform margin and slope in fractured carbonates with low (<6%) matrix porosity. Platform wells exhibit higher porosity (as much as 18%), but matrix permeability is typically low (<10 md).

Regional Paleogeography

The Precaspian Basin is a large Paleozoic basin that occupies much of the area known today as the northern part of the Caspian Sea and adjacent landmass. During the Early Carboniferous, the Precaspian Basin was a major equatorial sag basin in the western part of Kazakhstan (Ross and Ross, 1985). Carbonate shelves formed along the basin margins, and isolated, broad

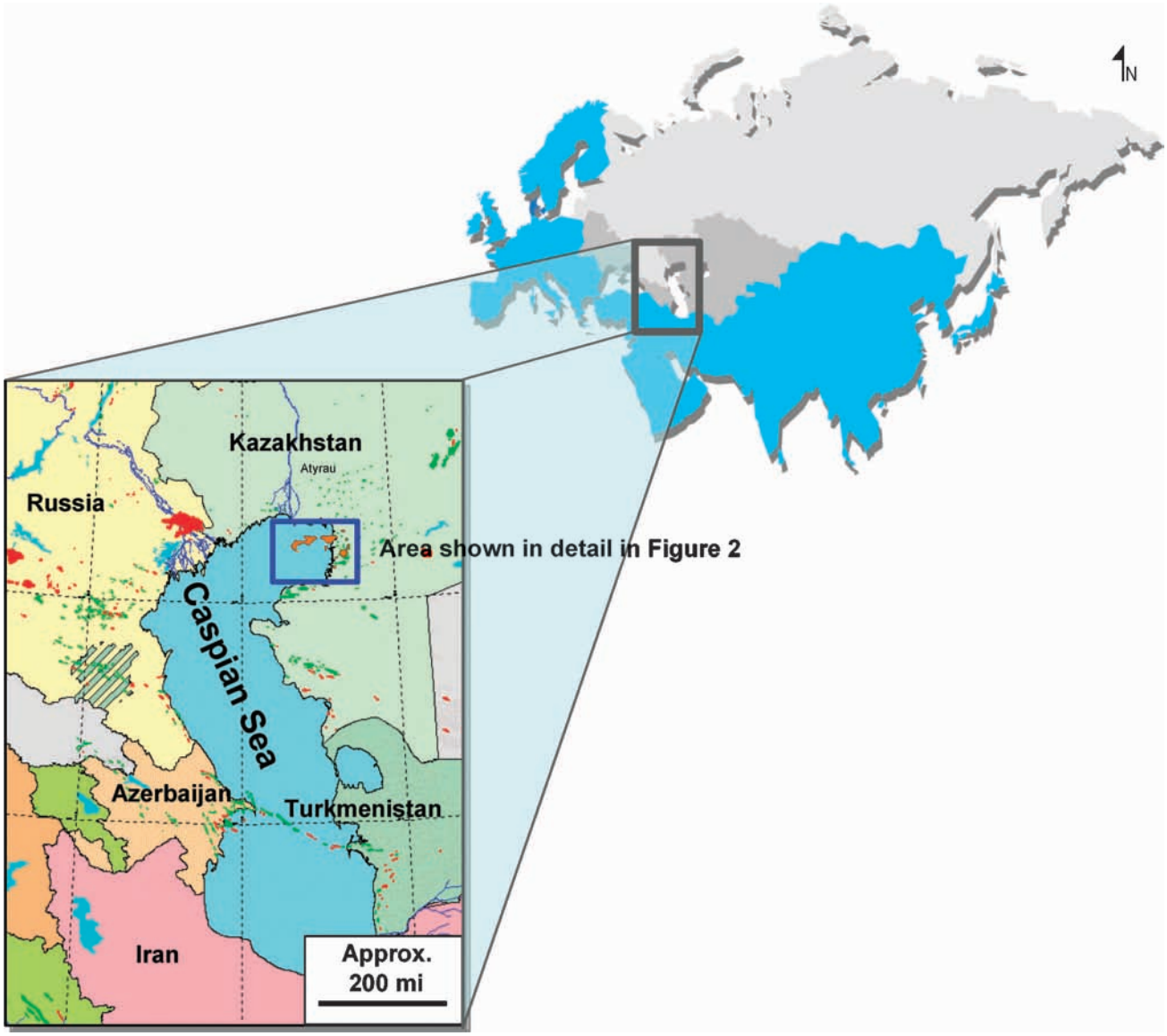

FIGURE 1. Index map locating North Caspian region and outlining area of the Tengiz field in blue, which is shown in more detail in Figure 2.

carbonate platforms grew on preexisting basement highs (Cook et al., 1997). Together with other nearby fields, Tengiz forms an archipelago of isolated carbonate platforms that grew on a regional pre-middle Devonian structural high near the southeastern margin of the basin (Figure 2). The initial carbonate platforms in the archipelago formed sometime after the Middle Devonian and continued more or less uninterrupted until the early Bashkirian. The total thickness of carbonate that accumulated at Tengiz during that time has not been drilled but is represented by approximately 1.2 s two-way traveltime on the most recent three-dimensional seismic survey (Figure 3). Following platform termination in the early Bashkirian, the platforms were encased in a series of lithologies associated with the closure of the Precaspian Basin. Initially, a veneer of Moscovian through Artinskian deep-water carbonates and volcaniclastics accumulated around and on top of the buildups. These deposits were followed by thick Kungurian evaporites, including halite that completely encased the platforms.

SUPERSEQUENCE FRAMEWORK

In 2001, a joint study by ExxonMobil, Chevron, and TengizChevroil established a stratigraphic framework for the Tengiz platform based on seismic, biostratigraphic, core, and well-log data. This study was published in late 2003 (Weber et al., 2003) and stands

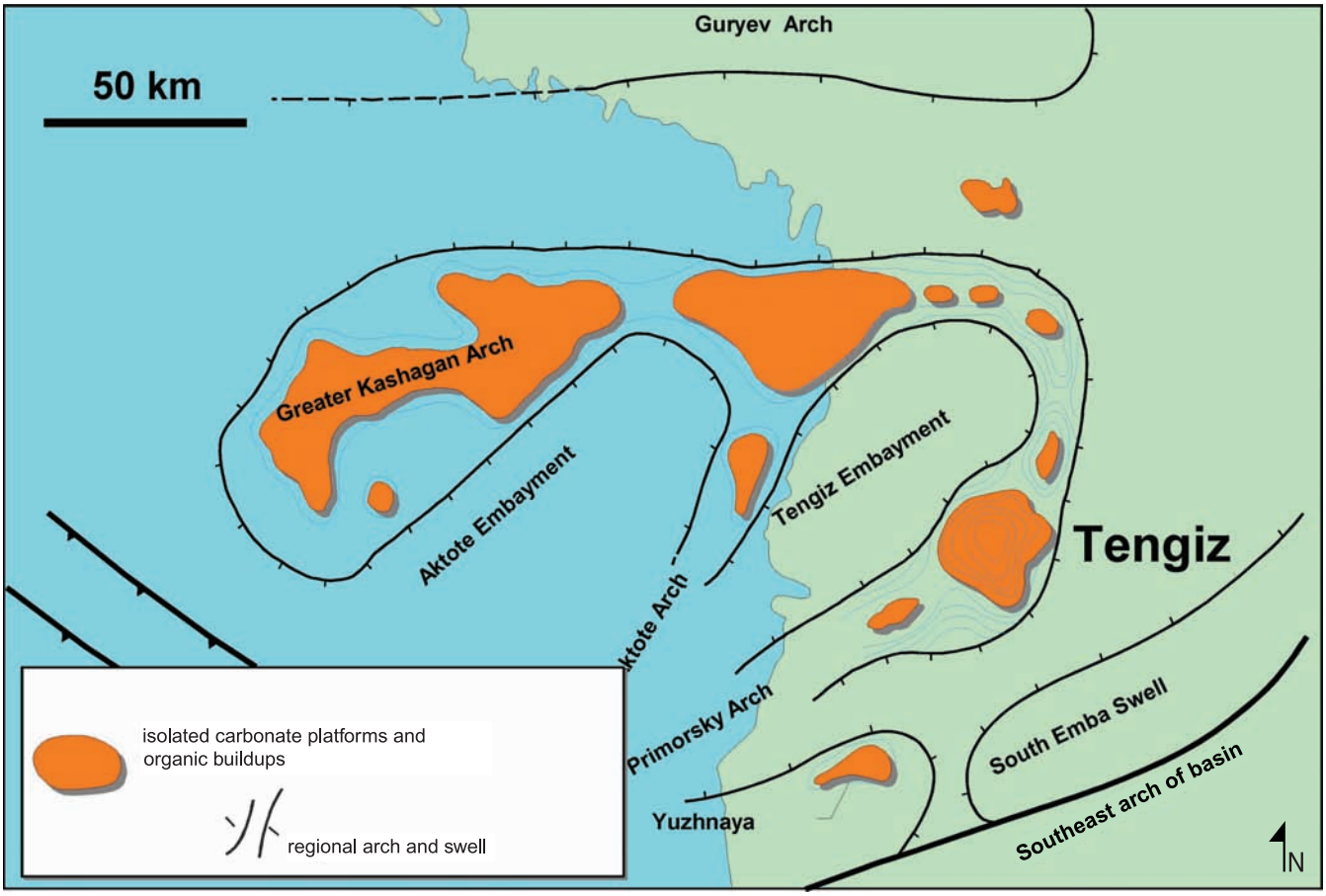

FIGURE 2. **Paleogeographic map showing the archipelago of isolated carbonate platforms, including Tengiz, that grew on a regional premiddle Devonian structural high near the southeastern margin of the Precaspian Basin.**

as the definitive stratigraphic reference for Tengiz. The framework consists of a hierarchy of sequences that have continued to be maintained as Tengiz drilling proceeds.

Through the main hydrocarbon-bearing interval at Tengiz (Famennian–Bashkirian), seven bounding discontinuity surfaces (sequence boundaries and maximum flooding surfaces [MFSs]) are recognized on seismic data (Weber et al., 2003) (Figure 4; Table 1). Two additional MFSs, Lvis1_MFS and Lvis2_MFS, are identified primarily from well control (cores and well logs). Four supersequences (Tournaisian–lower Visean, lower Visean–upper Visean, upper Visean–Serpukhovian, and Bashkirian) extend from the Famennian supersequence boundary (Fame_SSB) to the Bash_SSB (Weber et al., 2003). Each supersequence contains a transgressive sequence set (TSS) and a highstand sequence set (HSS) separated by an MFS. The upper two supersequences are the focus of this chapter. Three reservoir zones (Visean A, Serpukhovian, and Bashkirian) are contained in these supersequences and constitute the platform reservoir part of the Tengiz buildup.

Thin subaerial exposure caps on subtidal lithofacies form the most common type of cycle top in the Lvis_SSB to Bash_SSB succession on the Tengiz platform. The implication of this type of cycle boundary is that rapid base-level fall exposed subtidal lithofacies without development of an intervening tidal flat or peritidal succession. Alternatively, anchor points for tidal flats may not have been available because the depositional profile near the margin gradually deepened toward the platform break without the presence of a shallow barrier. In other words, the Tengiz platform was not conducive to producing extensive tidal-flat facies. Each cycle is more appropriately termed a "high-frequency sequence," capped by a high-frequency sequence boundary. Cycle boundaries also occur where subaerial exposure is not evident from core and thin-section description. Without evidence of subaerial exposure, upper bounding surfaces of these cycles define parasequences.

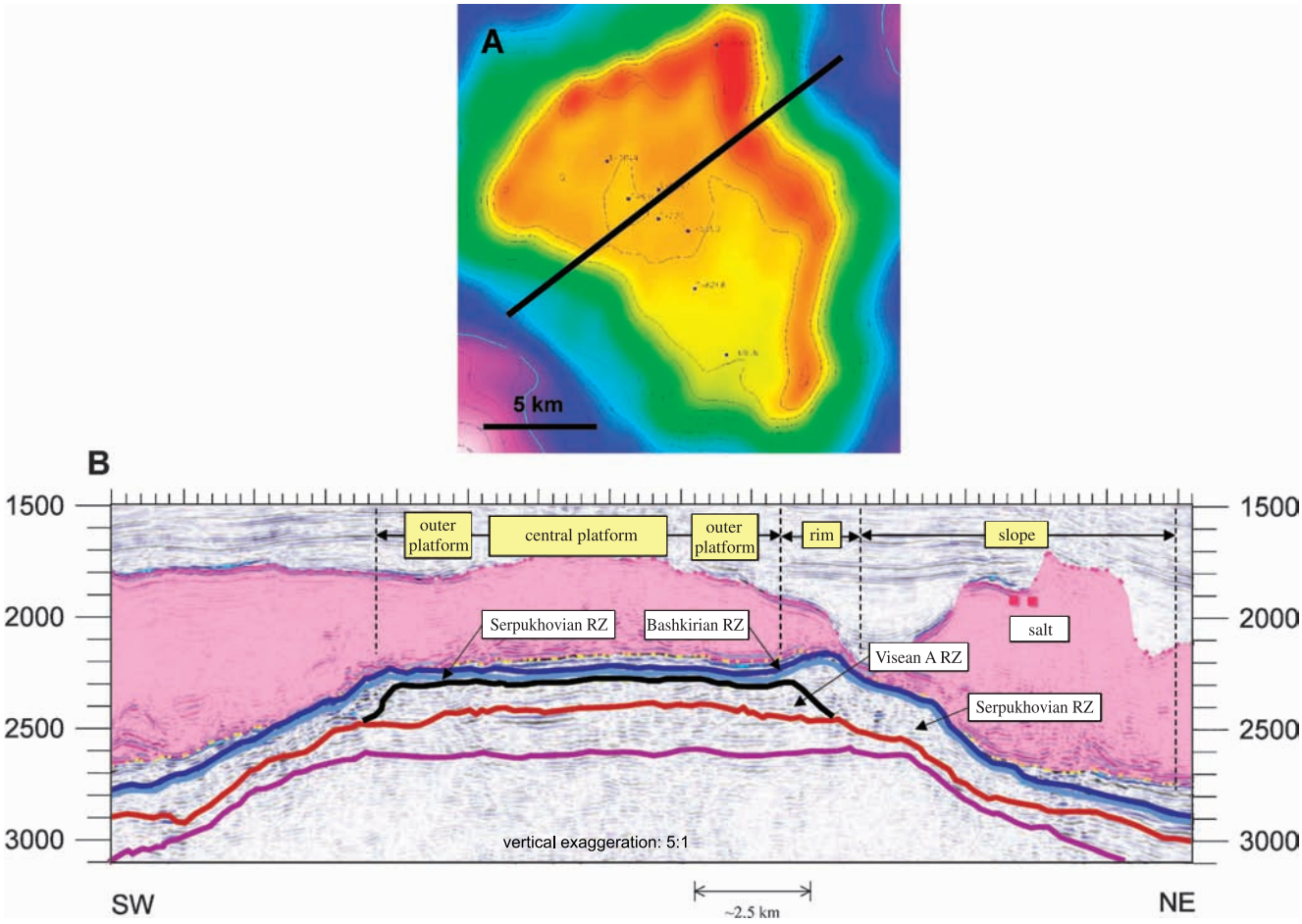

FIGURE 3. (A) Map of Tengiz showing the location of seismic line shown in (B). The map shows top reservoir (=top Bashkirian) structure with a contour interval of 100 m (330 ft). (B) Seismic profile showing general depositional areas of Tengiz buildup (central platform, outer platform, rim slope, or flank) and key reservoir zones (RZ). Vertical scale is two-way traveltime in milliseconds. See text for discussion.

Upper Visean–Serpukhovian Supersequence (Visean A and Serpukhovian Reservoir Zones)

The upper Visean–Serpukhovian supersequence is defined as the interval between the Lvis_SSB and the Serp_SSB (Figure 4). It includes the Mikhailovsky, Venevsky, Tarussky, Steshevsky, Protvinsky, and Zapaltyubinsky regional horizons (Weber et al., 2003). The Zapaltyubinsky zone is not generally recognized on the Tengiz platform but is observed in wells that penetrate the slope and basin. The Zapaltyubinsky may therefore represent a basinward shift in sedimentation and form a lowstand sequence set (Weber et al., 2003). However, rim failure processes (see Collins et al., 2006) have obscured stratal patterns that clearly define the formation of such a depositional body. On the platform, the upper Visean–Serpukhovian supersequence is approximately 250 m (820 ft) thick; however, equivalent slope deposits (see Collins et al., 2006) may exceed 600 m (1968 ft), where in-situ microbial boundstone and allochthonous debris aprons of platform- and slope-derived grainy carbonate and breccia accumulated (Figure 3). The upper Visean–Serpukhovian supersequence spans 14 m.y. (Gradstein et al., 2004).

The Lvis2_MFS separates the TSS of the supersequence from the overlying HSS (Figure 5). The TSS consists of five composite sequences that are dominantly aggradational and do not extend beyond the platform break of the underlying lower Visean–upper Visean supersequence. Small-scale backsteps are possible, but not proven, at or near the platform break through the TSS. Deeper water, low-energy open-marine, platform lithofacies in these sequences include crinoid grainstone-packstone and poorly sorted, thick-walled brachiopod grainstone-packstone. Shallower water, high-energy, open-marine to back shoal lithofacies

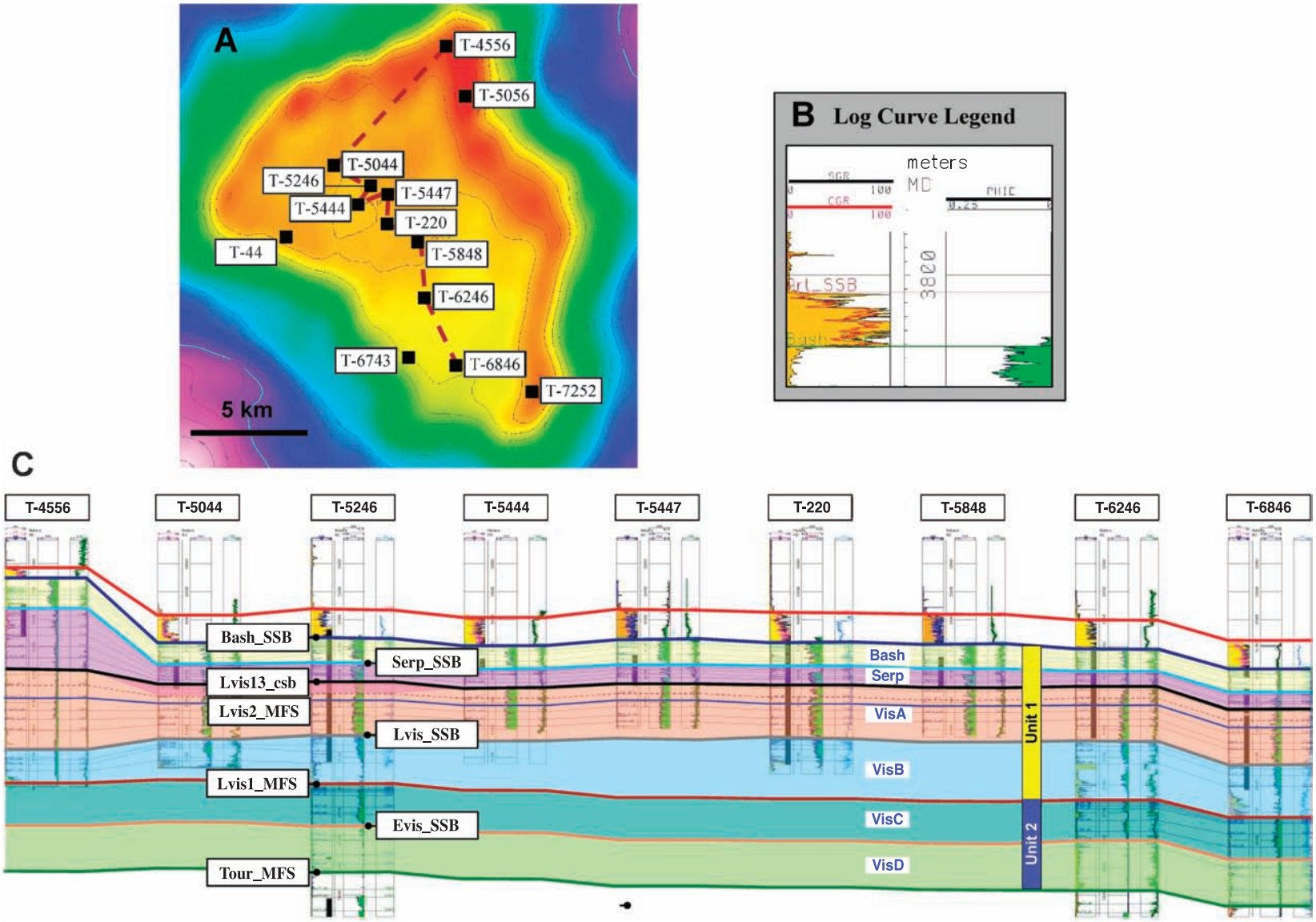

FIGURE 4. (A) Map of Tengiz showing the location of cross section shown in (C). The map shows top reservoir (=top Bashkirian) structure with a contour interval of 100 m (330 ft). (B) Legend for log curves shown in cross section of (C). Gamma-ray (SGR and CGR) is shown on the left and porosity (PHIE) on the right. (C) Cross section through Tengiz showing major stratigraphic surfaces and reservoir zonation scheme. Stratigraphic surfaces, in ascending order, are Tournaisian (Tour_MFS); early Visean (Evis_SSB); late Visean (Lvis1_MFS, Lvis_SSB, and Lvis13_csb); Serpukhovian (Serp_SSB); and Bashkirian (Bash_SSB). Reservoir zones bracketed by these surfaces are Visean D (VisD), Visean C (VisC), Visean B (VisB), Visean A (VisA), Serpukhovian (Serp), and Bashkirian (Bash). The Visean A, Serpukhovian, and Bashkirian are the subject of this study.

Table 1. Summary of sequence-stratigraphic nomenclature for Tengiz.*

Stage	*Reservoir Zones*		*Sequence*	*Top Surface*	*Sequence Number*
Bashkirian	Unit 1	Bashkirian	Bash6	Bash_SSB	1
			Bash4	Bash4_csb	2
			Bash2.5	Bash2.5_csb	3
			Bash1	Bash1_csb	4
Serpukhovian		Serpukhovian	Serp5	Serp_SSB	5
			Serp4	Serp4_csb	6
			Serp3	Serp3_csb	7
			Serp2	Serp2_csb	8
			Serp1	Serp1_csb	9
Late Visean		Visean A	Lvis13	Lvis13_csb	10
			Lvis12	Lvis12_csb	11
			Lvis11	Lvis2_MFS	12
			Lvis10.5	Lvis10.5_sb	13
			Lvis10	Lvis10_csb	14
			Lvis9.5	Lvis9.5_sb	15
			Lvis9	Lvis9_csb	16
		Visean B	Lvis8	Lvis_SSB	17
			Lvis7	Lvis7_csb	18
			Lvis6	Lvis6_csb	19
			HRZ	Lvis5_csb	20
	Unit 2	Visean C	Lvis4	Lvis1_MFS	21
			Lvis3	Lvis3_sb	22
			Lvis2	Lvis2_sb	23
			Lvis1	Lvis1_sb	24
Early Visean			Evis9	Evis9_sb	25
			Evis8	Evis8_sb	26
			Evis7	Evis7_sb	27
			Evis6	Evis6_sb	28
		Visean D	Evis5	Evis_SSB	29
			Evis4	Evis4_sb	30
			Evis3	Evis3_sb	31
			Evis2	Evis2_sb	32
			Evis1	Evis1_sb	33
Tournasian		Tournasian	Tour6	Tour_MFS	34
			Tour5	Tour5_sb	35
			Tour4	Tour4_sb	36
			Tour3	Tour3_sb	37
			Tour2	Tour2_sb	38
			Tour1	Tour1_sb	39
Famennian	Unit 3	Famennian A	Fame2	Fame_SSB	40
		Famennian B	Fame1	Fame_MFS	41

**This framework was established by Weber et al. (2003), and picks in wells have, since then, been refined as a result of new wells and progressed knowledge of the field.*

include well-sorted grainstone and grainstone-packstone consisting of algae, foraminifera, peloids, and coated grains.

The upper Visean–Serpukhovian HSS is subdivided into an aggradational and progradational phase. The aggradational interval from Lvis2_MFS to Serp1_csb (composite sequence boundary) is composed of three composite sequences (Figure 5). Significant progradation is observed in four subsequent composite sequences from the Serp1_csb to the Serp_SSB as shallow platform lithofacies fill available accommodation space and prograde to the present-day location of the

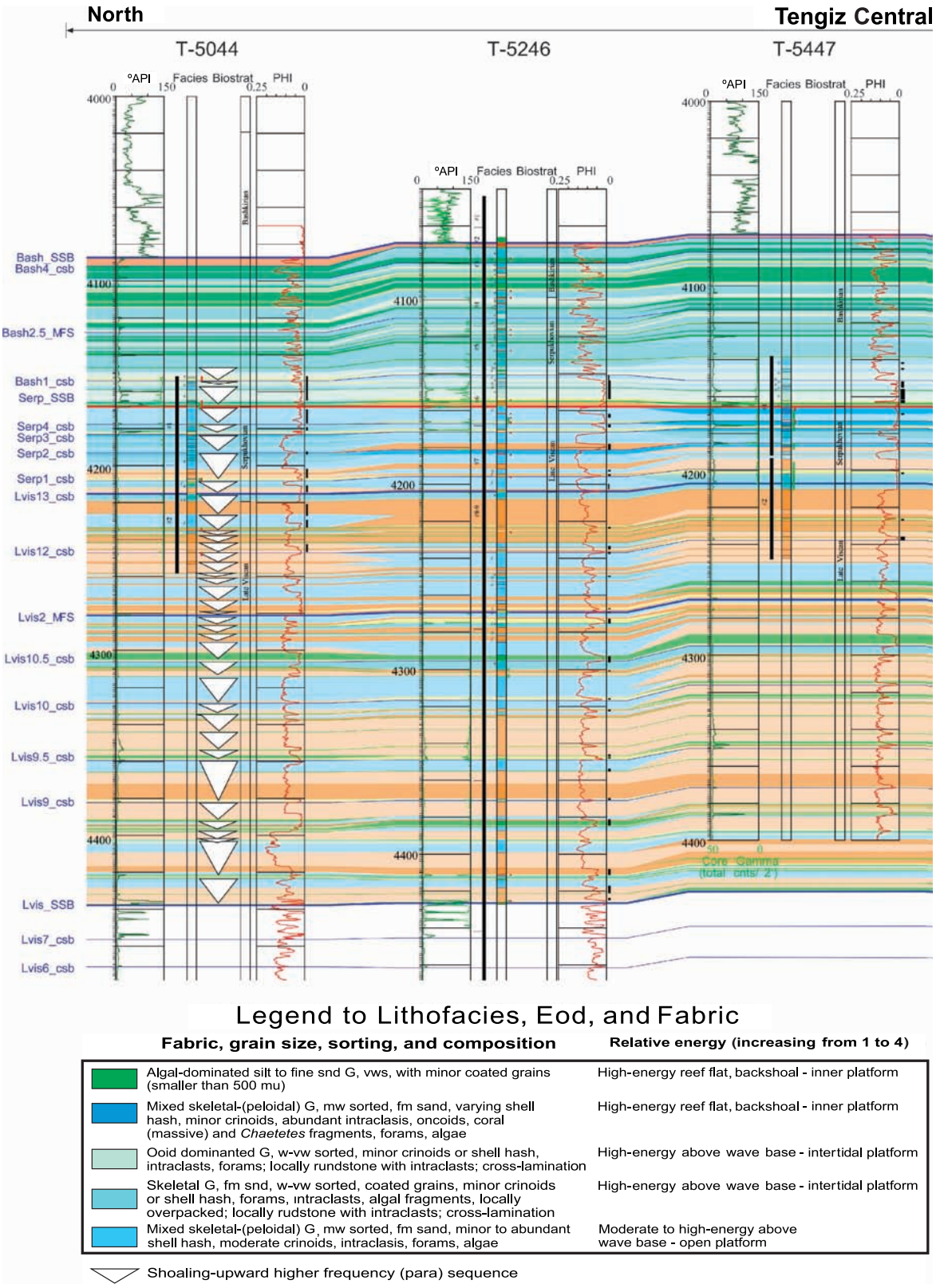

FIGURE 5. North–south cross section through wells T-5044, T-5246, T-5447, T-220, T-6246, and T-6846; well locations are shown in Figure 4A. Cross section show detailed lithofacies and cycle correlations in the central platform region in the Visean A (VisA), Serpukhovian (Serp), and Bashkirian (Bash) supersequences. The lithofacies legend was simplified from that of Weber et al. (2003) by reducing the number of facies types and relating them to the level of energy during deposition. Sequence stratigraphy is adopted from Weber et al. (2003); triangles identify higher order sequences (fourth and higher order) correlated from well to well. See text for further explanation and discussion.

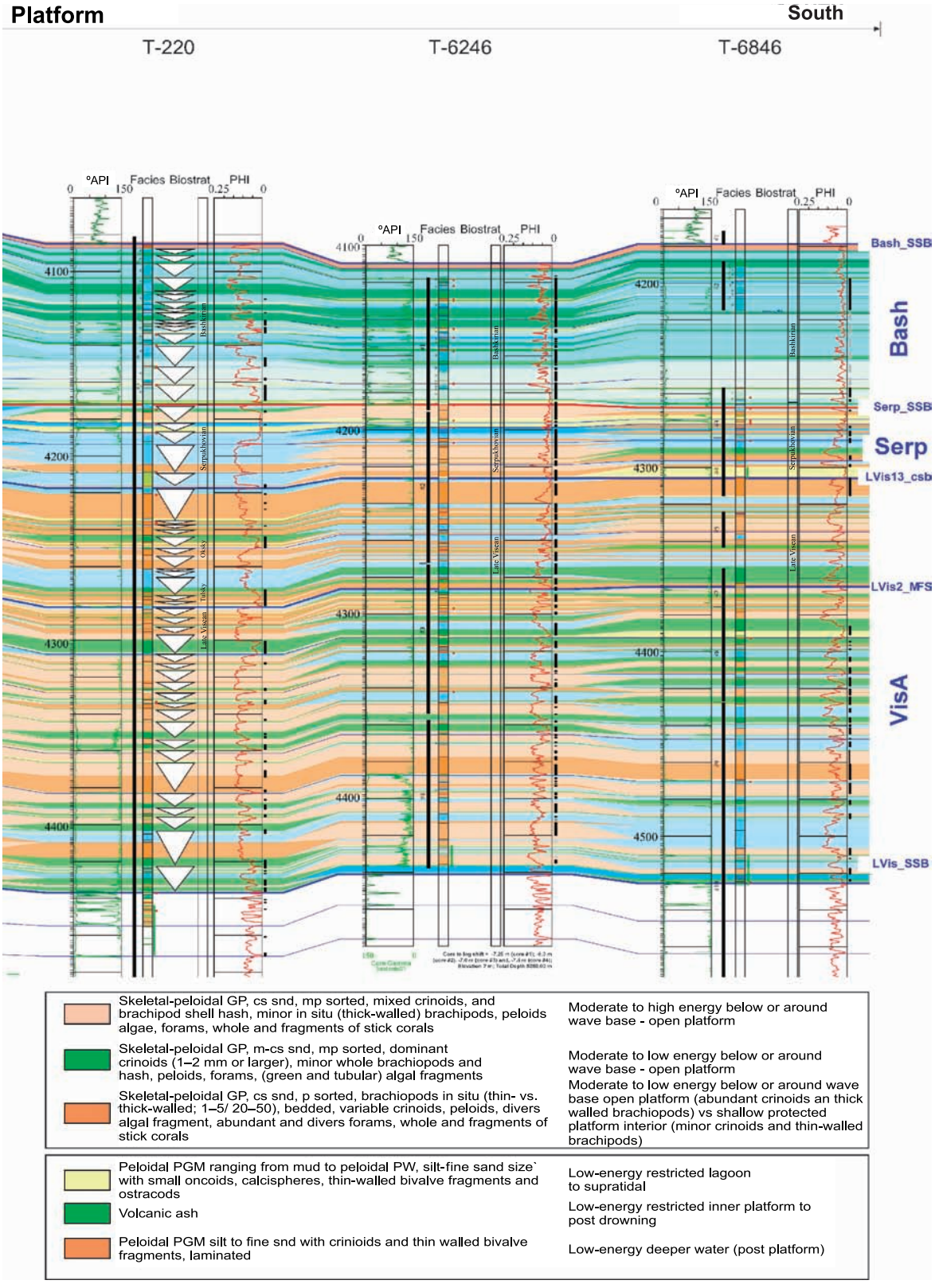
Platform
South
T-220
T-6246
T-6846
°API
Facies Biostrat
PHI
Bash_SSB
Serp_SSB
LVis13_csb
LVis2_MFS
LVis_SSB
Bash
Serp
VisA
Bashkirian
Serpukhovian
Late Visean
Oksky
Tulsky
Skeletal-peloidal GP, cs snd, mp sorted, mixed crinoids, and brachipod shell hash, minor in situ (thick-walled) brachipods, peloids algae, forams, whole and fragments of stick corals
Moderate to high energy below or around wave base - open platform
Skeletal-peloidal GP, m-cs snd, mp sorted, dominant crinoids (1–2 mm or larger), minor whole brachiopods and hash, peloids, forams, (green and tubular) algal fragments
Moderate to low energy below or around wave base - open platform
Skeletal-peloidal GP, cs snd, p sorted, brachiopods in situ (thin- vs. thick-walled; 1–5/ 20–50), bedded, variable crinoids, peloids, divers algal fragment, abundant and divers forams, whole and fragments of stick corals
Moderate to low energy below or around wave base open platform (abundant crinoids an thick walled brachiopods) vs shallow protected platform interior (minor crinoids and thin-walled brachipods)
Peloidal PGM ranging from mud to peloidal PW, silt-fine sand size` with small oncoids, calcispheres, thin-walled bivalve fragments and ostracods
Low-energy restricted lagoon to supratidal
Volcanic ash
Low-energy restricted inner platform to post drowning
Peloidal PGM silt to fine snd with crinioids and thin walled bivalve fragments, laminated
Low-energy deeper water (post platform)

platform break. As much as 400–500 m (1600–1900 ft) of depositional topography was filled on the slope as shallow-water platform lithofacies prograded over predominantly slope boundstone of microbial origin (Figure 3). During the progradational part (Serpukhovian) of the upper Visean–Serpukhovian HSS, the Tengiz buildup was an overall flat-topped platform with a substantial slope apron collecting debris primarily sourced from autochthonous boundstone growing on the outermost platform and upper slope and, to a lesser extent, from the platform top. The platform interior is dominated by grainy textures (packstone and grainstone), with packstone dominating in the deeper subtidal areas and well-sorted grainstone in the higher energy shallow subtidal parts of the platform.

Bashkirian Supersequence (Bashkirian Reservoir Zone)

The Bashkirian supersequence occurs between the Serp_SSB and the Bash_SSB (Figures 4, 5) and spans approximately 10 m.y. (Gradstein et al., 2004). The oldest Bashkirian horizon (i.e., Bogdanovsky) and most of the overlying Syuransky horizon do not appear to be present on the Tengiz platform (Brenckle and Milkina, 2001). The Akavassky and Askynbashsky horizons are generally present on the Tengiz platform above the Syuransky horizon. Although more work is necessary, results suggest that the early Bashkirian at Tengiz is transgressive, i.e., TSS of the Bashkirian supersequence (Figure 5). The HSS of the Bashkirian supersequence is very thin and condensed. Biostratigraphic analysis of core and cuttings typically dates the Bash_SSB as the top of the early Bashkirian. The late Bashkirian is condensed and represents starved sedimentation on an isolated platform, probably deposited in deep water (Weber et al., 2003).

Throughout most of the central part of the Tengiz platform, the Bashkirian supersequence is uniform in thickness (80–100 m; 262–330 ft). The Bashkirian platform break is generally aggradational through three composite sequences (Bash 1, 2.5, and 4) and coincident with the underlying platform break at the Serp_SSB. In isolated areas along the eastern margin of the platform, the Bashkirian section thickens to about 150 m (492 ft) (e.g., T-5056 and T-7252), with some of this thickening resulting from a facies change. Well-log correlations in these areas indicate that the uppermost composite sequence is locally 30–60 m (98–196 ft) thick (Weber et al., 2003), seismic data shows locally mounded seismic facies, and cores show skeletal packstone and local microbial boundstone on top of Serpukhovian microbial cement boundstone several hundreds of meters thick. The remaining thickening could be explained by differential compaction between the massive and mechanically strong boundstone and the compacted central platform. The latter is supported by the petrographic observation that most grainstones are overcompacted.

VISEAN A, SERPUKHOVIAN, AND BASHKIRIAN PLATFORM ARCHITECTURE

The Visean A, Serpukhovian, and Bashkirian reservoir zones are significant because they account for the bulk of the oil production from the platform part of the buildup. The platform is subdivided into different paleogeographic or depositional areas: central platform, outer platform, and rim slope (flank) (Figure 3). This chapter focuses on details of the central platform part of the Visean A, Serpukhovian, and Bashkirian intervals.

To refine the central platform stratigraphy, a careful comparison of core and thin sections in a series of north–south wells (T-5044, T-5246, T-5447, T-220, T-6246, and T-6846) produced a detailed lithofacies correlation across the central platform region in the Visean A, Serpukhovian, and Bashkirian reservoir zones (Figure 5). Several general observations can be made on the cycle stacking pattern, overall depositional framework, and facies patterns visible in Figure 5; they are summarized here and discussed in more detail in subsequent sections.

The succession of Visean A, Serpukhovian, and Bashkirian reservoir zones are, respectively, the TSS, HSS, and TSS of the two supersequences previously mentioned, and each consists of several composite and higher order sequences (cycles). Cycle stacking patterns (shoaling cycles as indicated by triangles in Figure 5) in the Visean A and Serpukhovian reservoir zones (and, respectively, TSS and HSS intervals) show a repetition of a thick cycle (15–20 m; 49–66 ft) with commonly a basal crinoid- and brachiopod-rich sand followed by a series of thinner cycles (2–8 m; 6.6–26 ft). Those crinoid- and brachiopod-rich facies are interpreted as generally deeper water and relatively low energy and commonly extend all across the platform, which would suggest significant flooding following a lowstand of relative sea level. Ten to twelve composite sequences, each containing two to six higher order sequences (cycles), are shown in Figure 5. The boundaries of these composite sequences do not always exactly match those by Weber et al. (2003), although the number of composite sequences is essentially the same.

The composite sequences described herein bundle into four larger sequences that each have a thick and laterally continuous brachiopod or crinoid interval near the base. Minor differences are observed between wells, but in general, the stacking pattern described above is very consistent. In the Bashkirian interval (mostly interpreted as TSS), the stacking pattern is more complex and shows a lower interval with thick cycles (~10 m; ~33 ft), followed by an interval dominated by thin (2–4-m; 6.6–13-ft) cycles, and an interval near the top of intermediate cycles (4–8 m; 13–26 ft). No clear stacking pattern is observed, and although lateral thickness variations are significant, the succession of thick, thin, and intermediate cycle intervals seems to be laterally continuous.

The moderate differences between the sequences established by Weber et al. (2003) and those described herein may lead to slight modifications of the platform sequence-stratigraphy framework. One potential modification is changing the MFS in the Visean A–Serpukhovian supersequence from its position at Lvis2_MFS as previously discussed to the base of the thick brachiopod interval observed between Lvis12_csb and Lvis13_csb, which marks a shift from a series of thinning cycles below to thick cycle above and an overall change of generally deeper facies below to higher energy shallow-water facies above (Figure 5).

These sequences of the Visean A, Serpukhovian, and Bashkirian intervals span a transition from greenhouse to icehouse cyclicity as suggested by observed trends in cycle thickness and general depositional environment. Another important observation is that sequences and cycles (third order and higher order) display a high degree of lateral continuity and constant thickness across the central platform area into the outer platform zones over distances of more than 10 km (6 mi) north to south. Careful inspection of this railroad pattern suggests the presence of a very low-angle top lap and possible truncation of underlying cycles at the Serp_SSB surface (the cross section of Figure 5 is flattened on this level). The truncation is variable but generally increasing to the south, indicating northward paleodip.

In general, it can be stated that the central platform area as documented in this chapter is several kilometers inboard from the physical break between platform and flank. The outer platform contains areas that remain poorly defined because of a lack of core penetrations and/or uncertainty of the physical and sedimentological character of the central platform-to-flank transition. Core penetrations close to the western edge of the platform are uncommon, but those available, wells T-44, T-6846, and T-6743, suggest moderate but substantial differences from the central platform area and, therefore, a potentially discontinuous transition from platform to flank. The situation is more complicated toward the eastern margin, where apparent top-lap geometry of the Serpukhovian and Bashkirian platform develops over a Serpukhovian boundstone slope. In the underlying Visean A platform, the transition may be comparable to that recognized from the western margin, wherein the Serpukhovian and Bashkirian central to outer platform transition seems to be gradual and changes from deeper outer platform with intercalated boundstone intervals into boundstone upper slope. As a consequence, the lateral facies associations below the pseudo-top-lap may be significantly different from those above. See Collins et al. (2006) for further discussion related to these transitions.

Lithofacies Types in the Central and Outer Platform

Core penetrations available for the Tengiz sequence-stratigraphic framework developed by Weber et al. (2003) were limited to TengizChevroil wells T-220, T-5246, T-6846, and incomplete cores from numerous older Russian wells (figure 3 of Weber et al., 2003). The present study builds on that of Weber et al. (2003) by adding the information from cores that nearly completely span the Visean A, Serpukhovian, and Bashkirian in several key wells in the central (T-5044, T-5447) and southwestern outer platform (T-6246) (Figure 4A). These complete core penetrations for the first time allowed a detailed comparison of each individual cycle (and facies types within) in the study window. Evaluation of core observations, petrography, and wire-line and core gamma logs (porosity was excluded during this phase) resulted in a coherent catalog of 10 key lithofacies types that are ranked primarily based on the relative hydrodynamic energy during deposition (Table 2). This information was extracted through environmental indicators like grain size, sorting, matrix type, sedimentary structures, and grain types (biota). The resulting 10 facies or rock types can be grouped into three or four composite rock types, reflecting major differences in energy conditions during deposition. The catalog was also designed to assist in the characterization of plugs and petrography of the key wells at 1-ft (0.3-m) intervals and serve as a direct link between geological parameters to reservoir properties.

Cyclic Lithofacies Variations

In the central platform, lithofacies stack into shallowing-upward cycles. The two supersequences and three reservoir zones making up the Lvis_SSB to

Table 2. Summary of lithofacies, pore types, porosity, and bitumen content for central platform wells T-220 and T-6246.*

Facies			*Fabric*	*EoD*
Abbreviation	*General Description*	*New Facies Code Number*	*Simplified Fabric Code*	
Algal grainstone (AG)	Algal dominated silt to fine sand G, very well sorted, with minor coated grains (smaller than 500 μm)	46	Grainstone	High-energy reef flat, backshoal-inner platform
Skeletal intraclast grainstone (SIG)	Mixed skeletal-(peloidal) G, moderately well sorted, fine to medium sand, varying shell hash, minor crinoids, abundant intraclasts, oncoids, coral (massive) and *Chaetetes* fragments, forams, algae	44	Grainstone	High-energy reef flat, backshoal-inner platform
Coated grain grainstone-rudstone (CgGR)	Ooid-dominated G, well to very well sorted, minor crinoids or shell hash, intraclasts, forams; locally rundstone with intraclasts; cross-lamination	43	Grainstone	High energy above wave base-intertidal platform
Ooid grainstone (OG)	Skeletal G, fine to medium sand, well to very well sorted, coated grains, minor crinoids or shell hash, forams, intraclasts, algal fragments, locally overpacked; locally rudstone with intraclasts; cross-lamination	42	Grainstone	High energy above wave base-intertidal platform
Well-sorted skeletal grainstone (SPG)	Mixed skeletal-(peloidal) G, moderately well sorted, fine to medium sand, minor to abundant shell hash, moderate crinoids, intraclasts, forams, algae	41	Grainstone	Moderate to High energy above wave base-open platform
Poorly sorted skeletal-peloid grainstone-packstone (SPP)	Skeletal-peloidal GP, coarse sand, moderately to poorly sorted, mixed crinoids and brachiopod shell hash, minor in-situ (thick-walled) brachiopods, peloids, algae, forams, whole and fragments of stick corals	32	Grainstone-packstone	Moderate to high energy below or around wave base-open platform
Crinoid skeletal-peloid grainstone-packstone (CSP)	Skeletal-peloidal GP, medium to coarse sand, moderately to poorly sorted, dominant crinoids (1–2 mm or larger), minor whole brachiopods and hash, peloids, forams, (green and tubular) algal fragments	31	Grainstone-packstone	Moderate to low energy below or around wave base-open platform
Brachiopod skeletal-peloid grainstone-packstone (BSP)	Skeletal-peloidal GP, coarse sand, poorly sorted, brachiopods in-situ (thin vs. thick-walled; 1-5/20-50), bedded, variable crinoids, peloids, divers algal fragment, abundant and divers forams, whole and fragments of stick corals	2	Grainstone-packstone	Moderate to low energy below or around wave base open platform (abundant crinoids an thick-walled brachiopods) versus shallow protected platform interior (minor crinoids and thin-walled brachiopods)
Peloid packstone-wackestone (PPW)	Ranging from mud to peloidal PW, silt-fine sand size with small oncoids, calcispheres, thin-walled bivalve fragments and ostracods	13	Packstone-grainstone	Low-energy restricted; restricted lagoon to supratidal
Volcanic ash (VA)	Volcanic ash	12	Clay mudstone	Low-energy restricted inner platform to postdrowning
All				
	Grain-supported mud-lean; high energy	41–46		
	Grain-supported muddy; intermediate energy	2, 31, 32		
	muddy; low energy	13		

**Lithofacies, also shown in Figure 5, are based on Weber et al. (2003), but simplified by reducing the number of facies and relating them to the level of energy during deposition. The vertical arrangement of lithofacies in this table resembles the ideal and most complete succession of lithofacies in a shoaling cycle or sequence. Pore types are 1 = interparticle; 2 = intraparticle; 3 = fenestral; 4 = shelter; 5 = growth framework; 6 = intercrystalline; 7 = moldic; 8 = microporosity; 9 = fracture; 10 = channel; 11 = vug; and 12 = enhanced dissolution. Note that bitumen analyses for well T-6246 are not yet complete. See text for discussion.*

T-220						T-6246			
N	Porosity			Bitumen (% Rock Volume)		N	Porosity		
	Dominant Pore Types	Range (%)	Mean (%)	Range	Mean		Dominant Pore Types	Range (%)	Mean (%)
24	11, 1, 6, 2	2.25–17.59	13.08	0.16–0.31	0.23	54/48	1, 7, 6, 11, 2, 9	0.84–14.80	4.90
18		0.18–16.35	4.46	0.08–0.41	0.28	22/22	1, 2, 7	0.97–12.07	4.58
78	11, 1, 7	0.42–23.66	10.09	0.13–6.86	1.35	36/36	1, 7, 11, 6, 9, 2	0.37–14.91	4.43
100	11, 1, 7, 2	0.78–21.36	11.79	0.01–2.73	0.40	103/78	1, 7, 6, 11, 2, 9	0.41–20.11	4.74
188	11, 1, 7, 6	0.19–23.18	11.64	0.04–6.36	0.23	217/114	1, 11, 2, 6, 7, 8	1.21–16.18	6.81
217	11, 1, 6, 7, 2	0.50–17.33	12.56	0.06–4.04	0.35	262/90	1, 11, 2, 9, 6, 7	0.97–15.3	6.91
83	11, 6, 1, 7, 9	0.34–14.79	5.37	0.05–5.54	2.58	79/14	1, 2, 11, 6, 7, 8	1.30–18.48	8.28
199	11, 1, 6, 2	1.45–17.53	10.51	0.09–5.49	0.68	207/27	11, 1, 6, 9, 2, 7	0.63–16.5	8.42
53	11, 9, 1, 6, 7, 2	0.07–17.55	3.62	0.11–3.72	0.67	49/14	1, 2, 11, 6, 7, 9	1.02–15.5	8.16
3									
971	11, 1, 6, 7, 2, 9	0.07–23.66	10.44	0.01–6.87	0.74	1031	1, 11, 2, 6, 7, 9	0.37–20.11	6.89
408	11, 1, 7, 2, 6	0.18–23.66	11.15	0.01–6.87	0.24	432	1, 11, 7, 6, 2, 9, 8	0.37–20.11	5.77
510	11, 6, 1, 2, 7	0.34–19.34	10.58	0.05–5.54	0.84	549	11, 1, 2, 6, 7, 9, 8	0.63–18.48	7.67
53	11, 9, 1, 6, 7, 2	0.07–17.55	3.62	0.11–3.72	0.67	48	1, 2, 11, 6, 7, 9	1.02–15.5	8.16

Bash_SSB interval comprise more than 50 cycles ranging in thickness from 2 to 15 m (6.6 to 49 ft) (Table 1; Figure 5). Commonly, cycles are bounded by thin volcanic ash layers less than a few centimeters in thickness that have been altered by burial diagenesis to resemble shale partings. Closely spaced volcanic ash partings are sometimes observed near bounding surfaces. Thicker ash beds do occur in some parts of the section (e.g., just above the Lvis_SSB and the Serp_SSB) and may exceed 1 m (3.3 ft) in thickness. Laminated ash beds were likely deposited (and preserved) during periods of low energy, either during exposure of the platform top or during the initial flooding and development of low-energy lagoonal deposits. The presence of thick (decimeter to meter) intervals of volcanic ash indicates major periods of exposure and/or deep initial flooding. These are therefore key surfaces that guided the selection of the supersequence boundaries.

When presented in the context of their depositional setting related to energy (i.e., bottom agitation) at the time of deposition, lithofacies roughly form a succession of low to higher energy from the base to top of a depositional cycle (see Table 1). One caveat in relating the lithofacies with energy level is that there is no one-to-one correspondence. For example, similar low-energy facies occur both in deeper subtidal as well as in more restricted shallow depositional environments. For discussion purposes, such a succession is shown in Table 1 and partly demonstrates lithofacies stacking from base to top. A brief description is provided in the sections immediately following, whereas the implications for the general depositional system (spatial distribution of lithofacies types and cycle thickness) are discussed in subsequent sections.

In brief, the description of lithofacies types and associated depositional energy, from base to top, is as follows: cycles generally start with a thin peloid packstone-wackestone that exhibits subaerial exposure features and are commonly interbedded with thin volcanic ash layers. These lithofacies are overlain by brachiopod and/or crinoid skeletal-peloid grainstone-packstone, which are, in turn, overlain by poorly sorted skeletal-peloid grainstone-packstone and/or well-sorted skeletal grainstone. This succession is, in turn, overlain by coated-grain grainstone-rudstone and/or ooid grainstone and locally a skeletal intraclast grainstone or algal grainstone. Obviously, deviations from this generalization exist, and cycle thickness, stacking patterns, and relative contribution of each facies type vary within and across the major sequences.

Peloid Packstone-wackestone (PPW) and Volcanic Ash (VA)

Peloid packstone-wackestone caps many shallowing-upward carbonate cycles and can overlie any of the other lithofacies. Usually less than 0.5 m (1.6 ft) thick, this lithofacies exhibits rhizoliths, laminated crusts, alveolar fabric, uncommon fenestrae, low-diversity microfauna (ostracods and calcispheres), and uncommon megascopic biota (Figure 6). Peloid packstone-wackestone includes the development of a pedolithic zone that occurs at most cycle boundaries, which is interpreted to include both the top of a cycle prior to exposure and the exposure event itself, as well as the initial reflooding event with intermittent exposure. Peloid packstone-wackestone nearly always has volcanic ash interbeds or dispersed volcanic ash (Figure 6A) and, probably as a result, is tight and well cemented. Volcanic ash is locally also dispersed within high-energy facies immediately below the Serp_SSB and below the Serp1_csb in well T-5447 (Figure 5). Those intervals are similarly tight and well cemented. The frequent occurrence of volcanic ash interbeds argues for nearly continuous fallout during deposition of the sequences; ash layers accumulated only during subaerial or low-energy conditions, thereby marking cycle boundaries on the gamma-ray logs. The preservation of volcanic ash is related to terrestrial fallout deposition during exposure and during initial low-energy conditions while the platform was submerged, probably in a shallow, restricted lagoon.

Brachiopod and Crinoid Skeletal-peloid Grainstone-packstone (BSP and CSP)

An inferred rise in relative sea level resulted in slightly deeper conditions and deposition of skeletal grainstone to packstone at the base of a cycle. The basal part of the cycles can be either brachiopod skeletal-peloid grainstone-packstone or crinoid skeletal-peloid grainstone-packstone, but brachiopod skeletal-peloid grainstone-packstone is dominant.

Brachiopod skeletal-peloid grainstone-packstone is interpreted to represent the continued flooding of the platform in relative low-energy conditions. Thick accumulation of such deposits could indicate deeper water or ongoing restriction caused by emergent outer platform shoals or barriers. The facies is initiated during initial flooding of the platform and is most robust during times of maximum flooding. Brachiopod skeletal-peloid grainstone-packstone is poorly sorted, composed of large, commonly in growth position, thick-walled brachiopods, variable crinoids, diverse algal fragments and foraminifera, and/or corals (Figure 7). Brachiopod

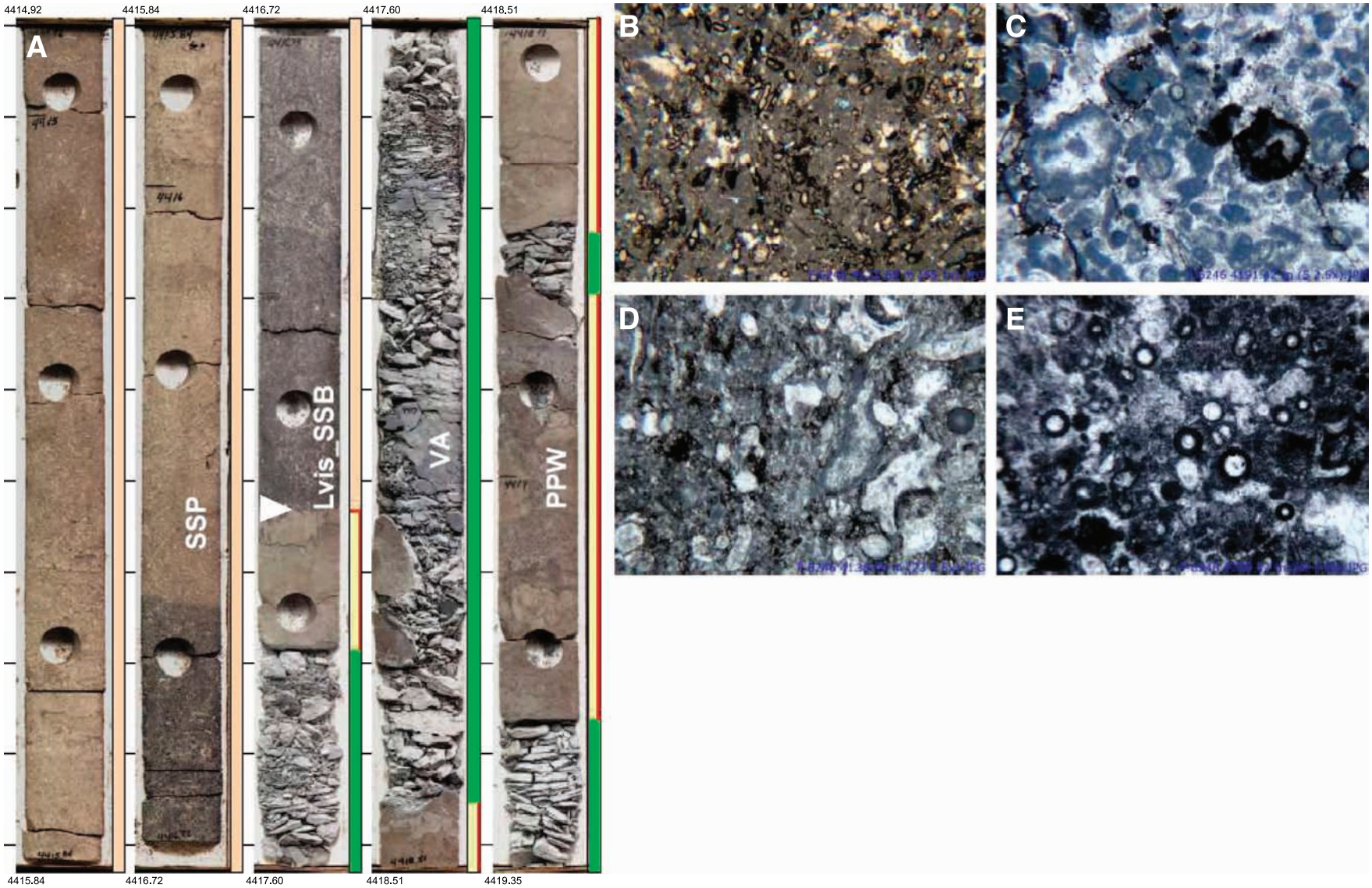

FIGURE 6. (A) Core photos from well T-5246 show peloid packstone-wackestone (PPW) alternating with volcanic ash layers (VA) below the Lvis_SSB. The boundary that shows evidence for subaerial exposure is overlain by poorly sorted skeletal-peloid grainstone-packstone (SPP) with elevated bitumen cement in the lower 70 cm (27 in.) (see Table 2 and Figure 5 for additional lithofacies information). Photomicrographs show the range of PPW textures. Common skeletal grains are tubular algal fragments (B, D), calcispheres (B, E), and minor coated skeletal grains and aggregrate grains (C, D). Width of photomicrographs is 4.20 and 1.58 mm (0.16 and 0.062 in.) (B, C–E, respectively).

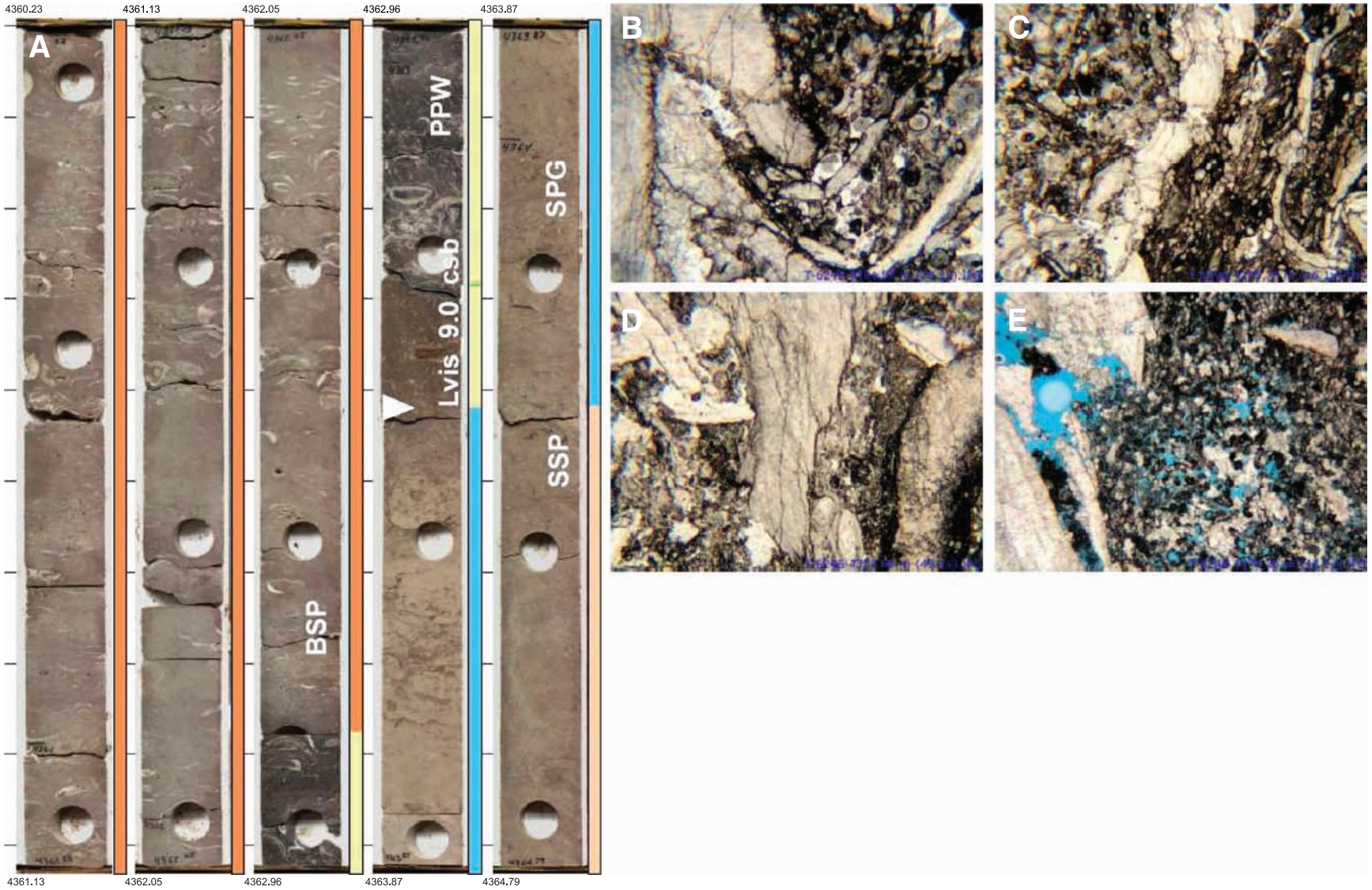

FIGURE 7. (A) Core photos from well T-5246 show shoaling succession of skeletal-peloid grainstone-packstone (SSP) and well-sorted skeletal grainstone (SPG) immediately below the Lvis_9.0_csb. The boundary is overlain by peloid packstone-wackestone (PPW) and a thick interval of brachiopod-skeletal-peloid grainstone-packstone (BSP). Concentrations of in-situ brachiopods and local development of intraparticle and shelter porosity are clearly visible in the BSP interval. Photomicrographs (B–E) show the generally poorly sorted texture and microfractured nature of BSP. Brachiopods are dominant constituents and range from small thin-walled (less than 2 cm [0.8 in.] long and 1 mm [0.04 in.] thick) to large and thick-walled species (respectively, 5–15 cm [1.9–5.9 in.] and 1–10 mm [0.04 and 0.40 in.]). Note the sutured, stylotized contacts of the brachiopods. Other common grain types are crinoid ossicles, peloids, algal fragments, and benthic foraminifera. Width of photomicrographs is 4.20 mm (0.16 in.).

skeletal-peloid grainstone-packstone intervals are generally continuous across the platform, appear to thin toward the outer platform, and have the highest frequency and volume in the upper part of the Visean A (between Lvis_13 and Lvis_10.5), where they generally form the basal parts of most cycles (Figure 5). Intervals of brachiopod skeletal-peloid grainstone-packstone occur sporadically in the lower part of the Visean A platform. Two very distinct and thick-bedded (4–10-m; 13–33-ft) intervals, one right above the Lvis9_csb and one below the Lvis13_csb, blanket the entire platform.

Crinoid skeletal-peloid grainstone-packstone is coarse and poorly to moderately sorted crinoid-dominated skeletal-peloidal sand. The crinoids commonly have destructionally micritized outer surfaces; other common components are mostly broken brachiopods, green and red algal fragments, and foraminifera (Figure 8). Crinoid skeletal-peloid grainstone-packstone intervals are generally not continuous across the platform and seem to preferentially occur near the platform margin (wells T-6846, T6246, T-8, and T-44). Crinoid skeletal-peloid grainstone-packstone is interpreted as being deposited in moderate to low energy below or around wave base and may represent the time of maximum flooding. These intervals represent the maximum open-marine influx during the cycle, and only one interval (right above Lvis_10.5) covers the entire platform (Figure 5).

Poorly Sorted Skeletal-peloid Grainstone-packstone (SPP) and Well-sorted Skeletal Grainstone (SPG)

Poorly sorted skeletal-peloid grainstone-packstone and well-sorted skeletal grainstone generally occur above brachiopod skeletal-peloid grainstone-packstone and crinoid skeletal-peloid grainstone-packstone, exhibit progressively better sorting and less mud, and therefore have been interpreted as shallow-water wave-agitated sand shoal deposits (Figures 9, 10, respectively). These grainstone lithofacies dominate the cycles for most of the Visean A reservoir and commonly show lateral shifts from one facies into the other. In the T-5246 well, well-sorted skeletal grainstone dominates the cycles, and there seems to be a general subtle increase away from the central platform (Figure 5). Immediately above the Lvis2_MFS, a southward thinning interval of well-sorted skeletal grainstone covers the entire platform.

Coated-Grain Grainstone (CgGR), Ooid Grainstone, (OG), and Skeletal-intraclast Grainstone (SIG)

In a complete cycle, the previously described lithofacies are overlain by cross-bedded or uniformly laminated, well-sorted coated-grain and/or ooid grainstone, which are interpreted as high-energy shallow subtidal open-platform to intertidal deposits (Figures 11, 12, respectively). Ooids are generally small, ranging from 0.5 to 1.0 mm (0.02 to 0.04 in.), and were most probably calcitic in origin from their radial structure. Coated grains are commonly skeletal fragments with coatings that are micritic and mainly constructional. Coated-grain grainstone has uncommon occurrences in the Visean A but is common in the Serpukhovian reservoir (Figure 5), where it is concentrated in the northern part of the platform amplifying a general trend from higher energy in the north to lower energy (and/or open marine) toward the south. Coated-grain and/or ooid grainstones are locally overlain by a relatively thin interval of coarse-grained lithoclastic rudstone-grainstone, skeletal-intraclast grainstone, with centimeter-size subangular to well-rounded intraclasts and *Chaetetes* (demosponge) fragments, which are commonly coated by micrite (Figure 13). Some intervals display clast-supported flat pebbles, indicative of beach environments. Dominant grain types range from coated grains to ooids and algal grains.

Algal Grainstone (AG)

Finally, very well-sorted and cross-bedded, silt to fine sand-size, algal grainstone occurs near the top of the Bashkirian sequences and locally in the Visean A sequence (Figures 5, 14). Algal grainstone intervals were also observed in the outermost platform (Serpukhovian) of the T-4556 well and may indicate the occurrence of this facies in a high-energy outer platform setting. Elsewhere on the platform, algal grainstone alternates with more open-marine well-sorted skeletal grainstone or coated-grain grainstone-rudstone; in these instances, algal grainstone is interpreted as being deposited in the intertidal zone near the top of cycles, perhaps sourced from the outer platform and filling the remaining accommodation space.

Lithofacies Mosaics

Figure 15 shows hypothetical depositional models of higher order depositional cycles for both the Bashkirian sequence (Figure 15A) as well as the Visean A and Serpukhovian sequences (Figure 15B). The models show grain compositional and textural trends from the central platform through the outer platform and into the upper flank and indicate some associated bathymetric relief during the Visean A and Serpukhovian. In the central platform, Visean A and Serpukhovian platform cycles are vertically and laterally relatively predictable and show a succession, from base to top, that reflects depositional energy. Near

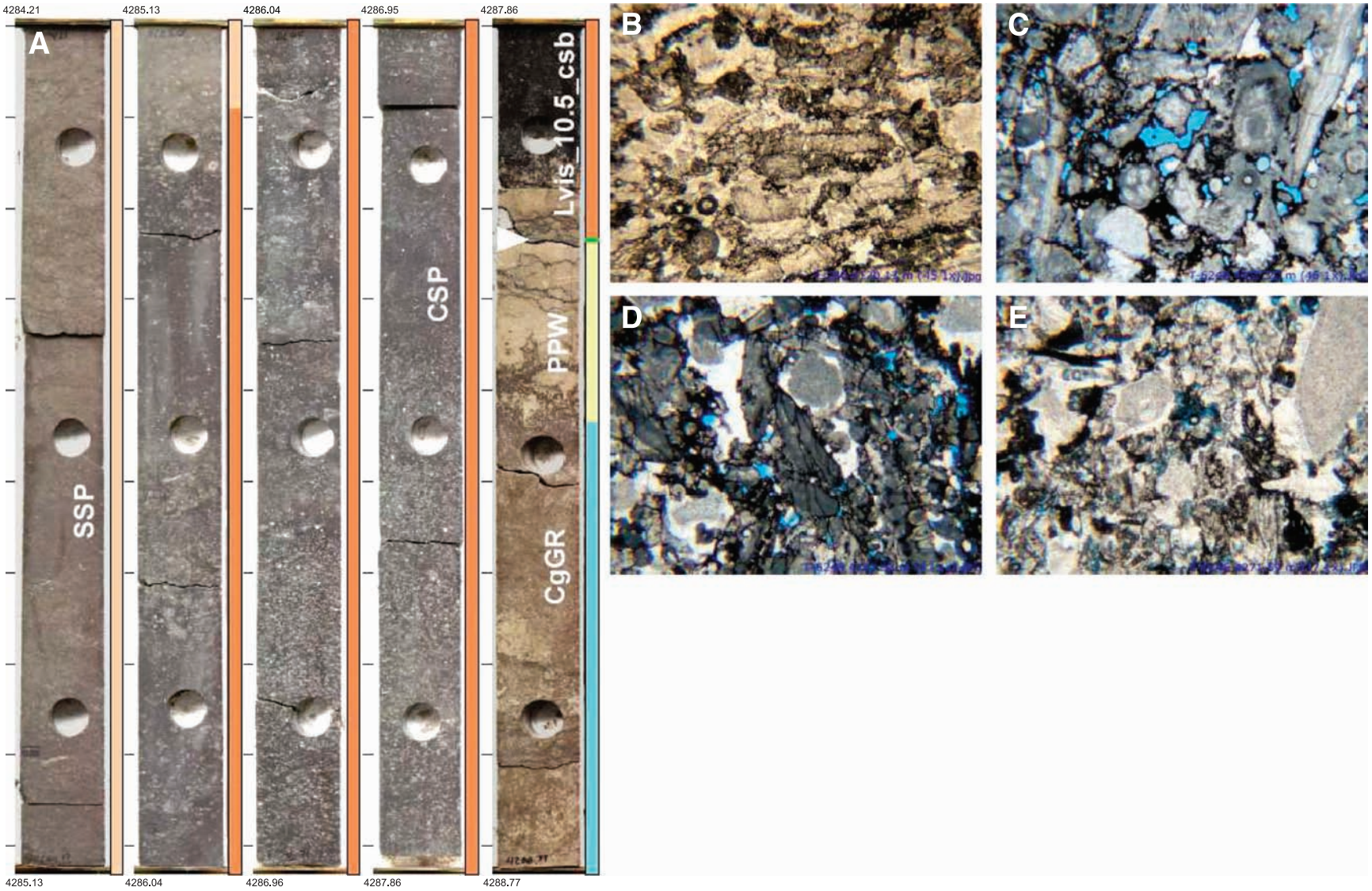

FIGURE 8. (A) Core photos from well T-5246 show succession of well-sorted coated-grain grainstone (CgGR) overlain by peloid packstone-wackestone (PPW) and capped by the Lvis_10.5_csb. The boundary is, in turn, overlain by crinoid skeletal-peloid grainstone-packstone (CSP) and poorly sorted skeletal-peloid grainstone-packstone (SPP) (see Table 2 and Figure 5 for additional lithofacies information). The CSP interval is only moderately stained by bitumen here in T-5246, whereas toward the outer platform, it is commonly completely stained black. Crinoid skeletal-peloid grainstone-packstone is coarse and poorly to moderately sorted crinoid-dominated skeletal-peloidal sands (B) with destructionally micritized outer surfaces (C) and common components as (mostly broken) brachiopods, (green and red) algal fragments and foraminifera (B–E). Common grain types are crinoid ossicles, brachiopod hash and whole valves, peloids, algal fragments (notably *Koninckopora*), benthic foraminifera. Width of photomicrographs is 4.20 mm (0.16 in.).

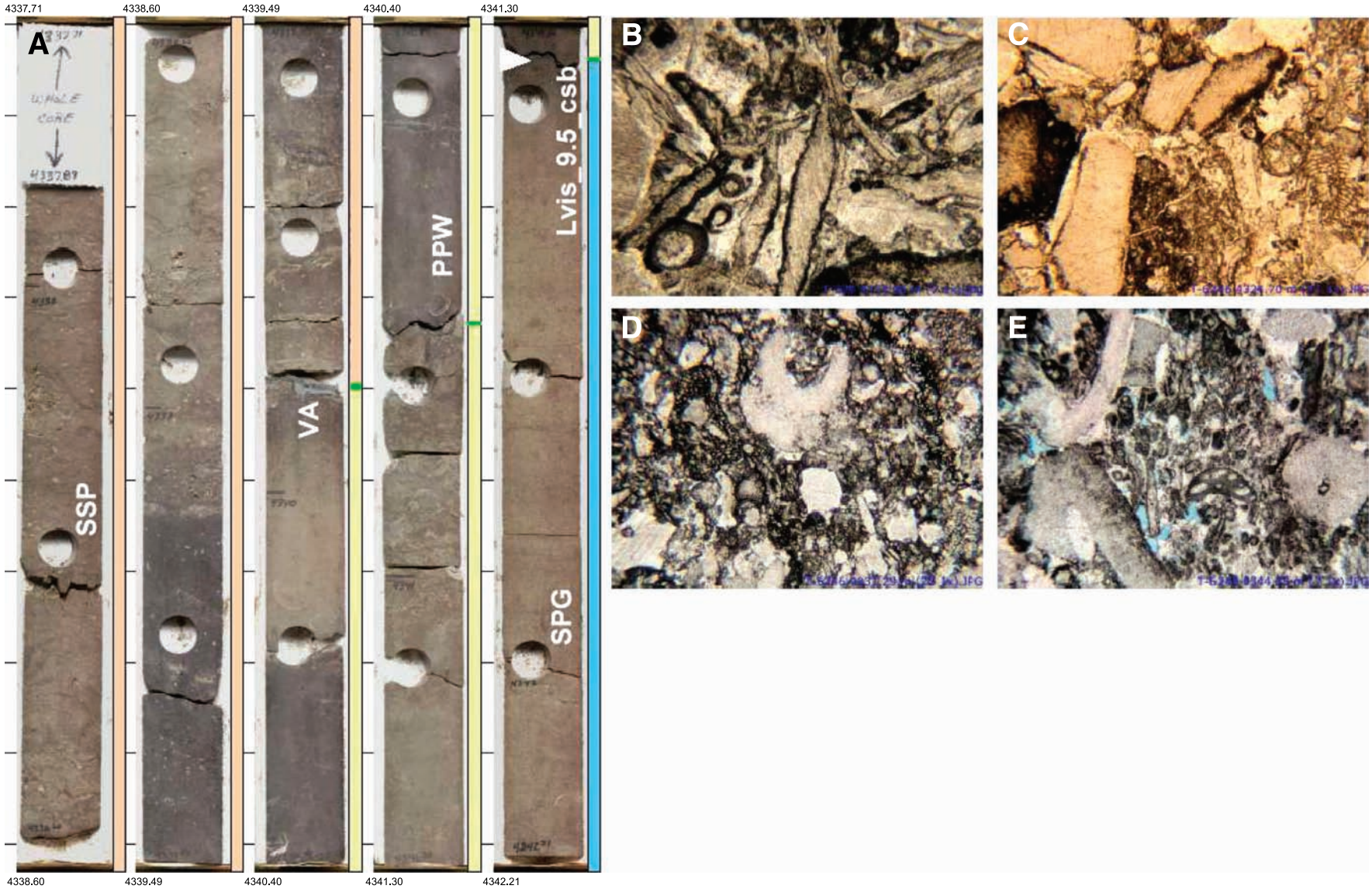

FIGURE 9. (A) Core photos from well T-5246 show a thick interval of poorly sorted skeletal-peloid grainstone-packstone (SPP) at the top. The lower half of the core contains a shoaling succession of well-sorted skeletal grainstone (SPG) capped by Lvis_9.5_csb. The boundary is overlain by peloid packstone-wackestone (PPW) with a thin volcanic ash (VA) interbed near the top (see Table 2 and Figure 5 for additional lithofacies information). The skeletal-peloid grainstone-packstone (SSP) and well-sorted skeletal grainstone (SPG) are generally located above the B- and CSP; because they exhibit progressively better sorting and less mud, they have been interpreted as shallow-water wave-agitated sand shoal deposits. Common grain types found in SPP shown in (B–E) are crinoid ossicles, brachiopod hash, peloids, algal fragments, and benthic foraminifera. Grains are commonly coated by thin micrite rims and are poorly sorted. Width of photomicrographs is 4.20 mm (0.16 in.).

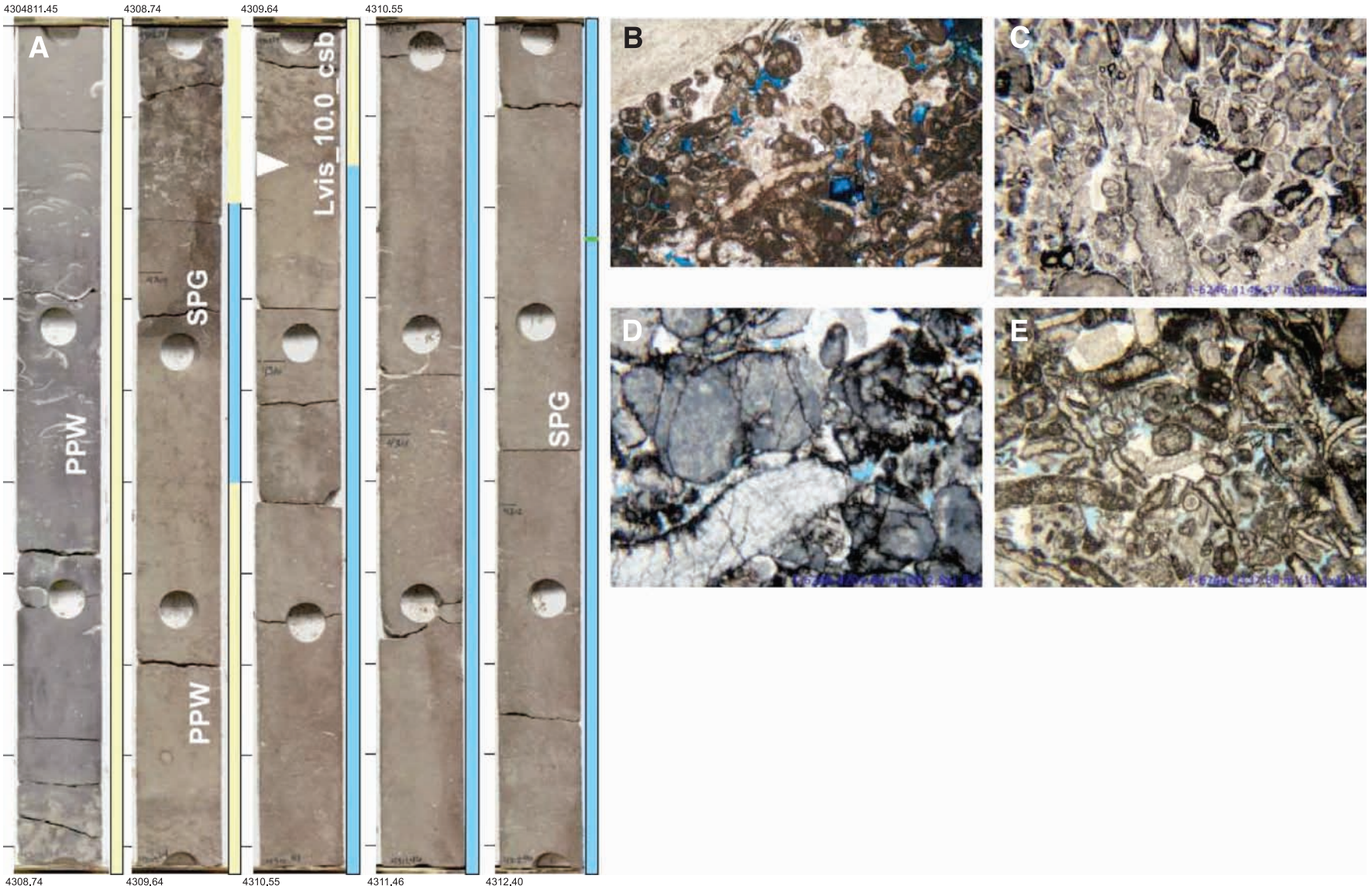

FIGURE 10. (A) Core photos from well T-5246 show shoaling succession of well-sorted skeletal grainstone (SPG) capped by Lvis_10.0_csb. The boundary is overlain by thin peloid packstone-wackestone (PPW), well-sorted skeletal grainstone (SPG), and peloid packstone-wackestone (PPW), with large thin-walled brachiopods (see Table 2 and Figure 5 for legend). Well-sorted skeletal grainstones (SPG) are generally located above the BSP and CSP lithofacies, exhibit better sorting and less mud, and have been interpreted as shallow-water wave-agitated sand shoal deposits. Photomicrographs (B–E) show common grain types of SPG: crinoid ossicles, brachiopod hash, peloids, algal fragments, and benthic foraminifera. Width of photomicrographs is 4.20 mm (0.16 in.) (B, C, E) and 1.58 mm (0.06 in.) (D).

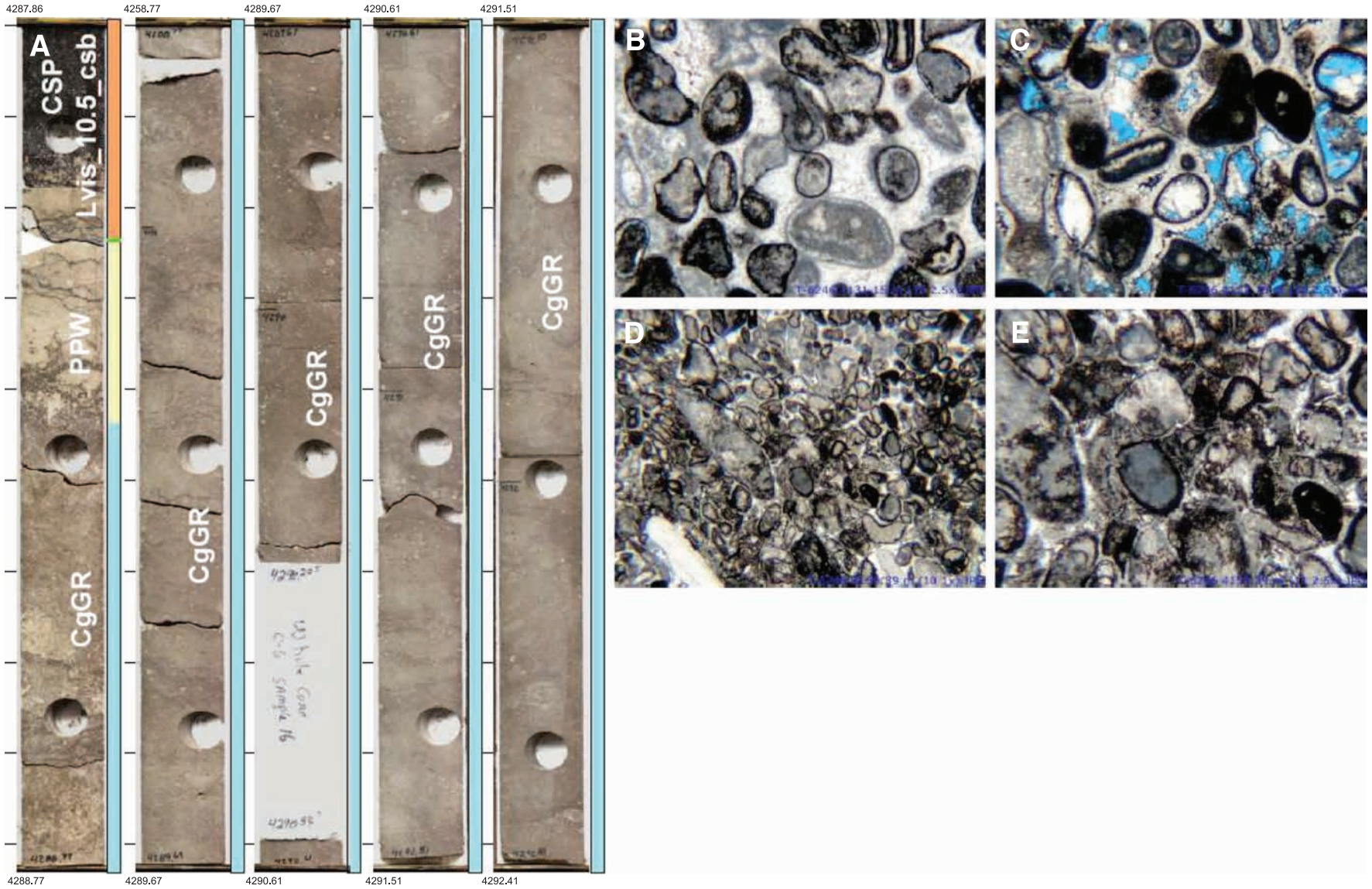

FIGURE 11. (A) Core photos from T-5246 show shoaling succession of a thick interval of cross-beds, but laminations are obscured by bioturbation, well-sorted coated-grain grainstone (CgGR), which is overlain by a thin peloid packstone-wackestone (PPW). The Lvis_10.5_csb is overlain by coarse and poorly to moderately sorted crinoid-dominated skeletal-peloidal sands (CSP) (see Table 2 and Figure 5 for legend). In a complete cycle, mixed skeletal-peloidal sands (mostly SPG) are overlain by cross-bedded or uniformly laminated, well-sorted coated-grain and/or ooid grainstone (CgGR and OG), interpreted as high-energy shallow subtidal open platform to intertidal deposits. Common grain types in CgGR shown in (B–E) are well-sorted peloids, coated skeletal grains, algal fragments (tubular), and benthic foraminifera; crinoid ossicles and brachiopod hash are minor grains. Width of photomicrographs is 4.20 mm (0.16 in.) (D) and 1.58 mm (0.06 in.) (B, C, E).

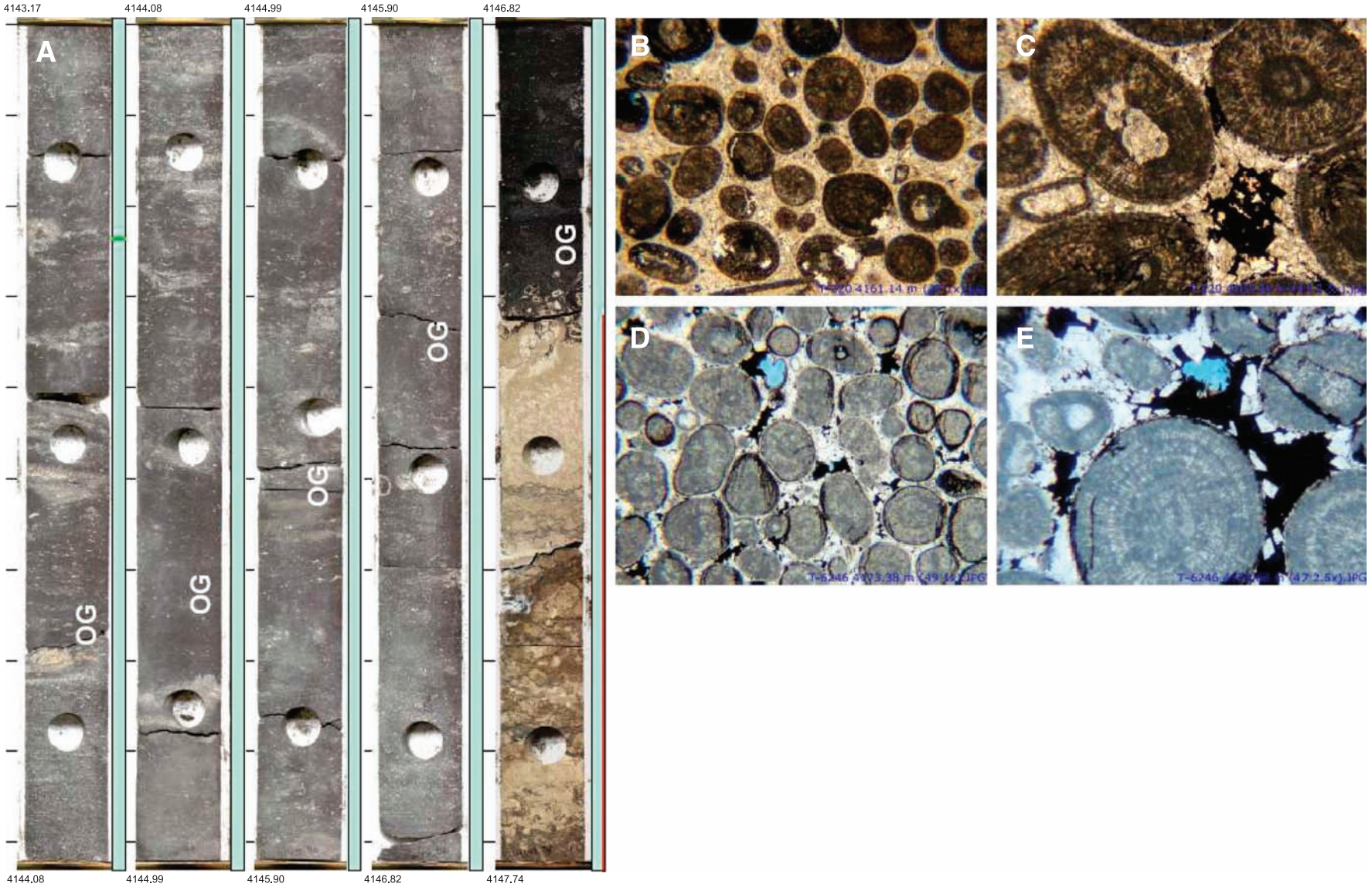

FIGURE 12. (A) Core photos from T-5246 show part of an approximately 5–6-m (16–19-ft)-thick interval of cross-bedded, well-sorted ooid grainstone (OG). An exposure surface, with small intraclasts, separates a dark, bitumen-rich interval above from the underlying better cemented, yellow-cream-colored interval in the rightmost core slab (see also Table 2 and Figure 5 for legend). In the Bashkirian, a complete cycle of mixed skeletal-peloidal sands (mostly SPG) is generally overlain by cross-bedded ooid grainstone lithofacies (OG) interpreted as high-energy shallow subtidal open platform to intertidal deposits. Photomicrographs (B–E) show the dominant grain types of ooids and coated skeletal grains; algal fragments (tubular) and benthic foraminifera also occur. Width of photomicrographs is 4.20 mm (0.16 in.) (B, D) and 1.58 mm (0.06 in.) (C, E).

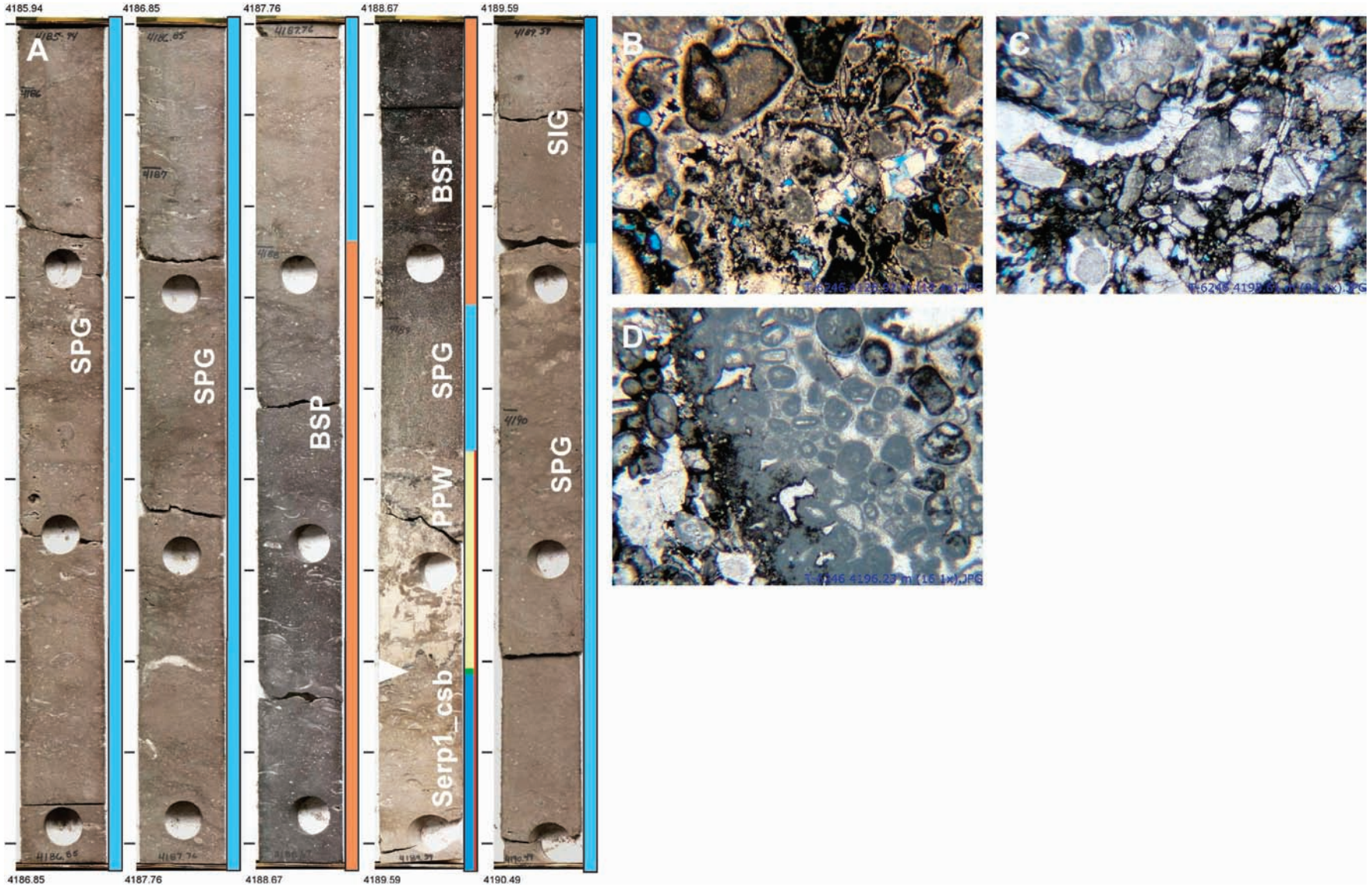

FIGURE 13. (A) Core photos from T-5246 show a shoaling succession of well-sorted skeletal grainstone (SPG), overlain by a relatively thin interval of coarse-grained skeletal-intraclast grainstone (SIG), and capped by the Serp1_csb. The boundary is overlain by thin intervals of PPW and SPG, brachiopod-skeletal-peloid grainstone-packstone (BSP), and another interval of SPG (see Table 2 and Figure 5 for legend). (B–D) Skeletal-intraclast grainstone (SIG) typically has centimeter-size subangular to well-rounded intraclasts and *Chaetetes* fragments, which are commonly coated by micrite. Other grains are coated grains, ooids, and algal fragments. Width of photomicrographs is 4.20 mm (0.16 in.).

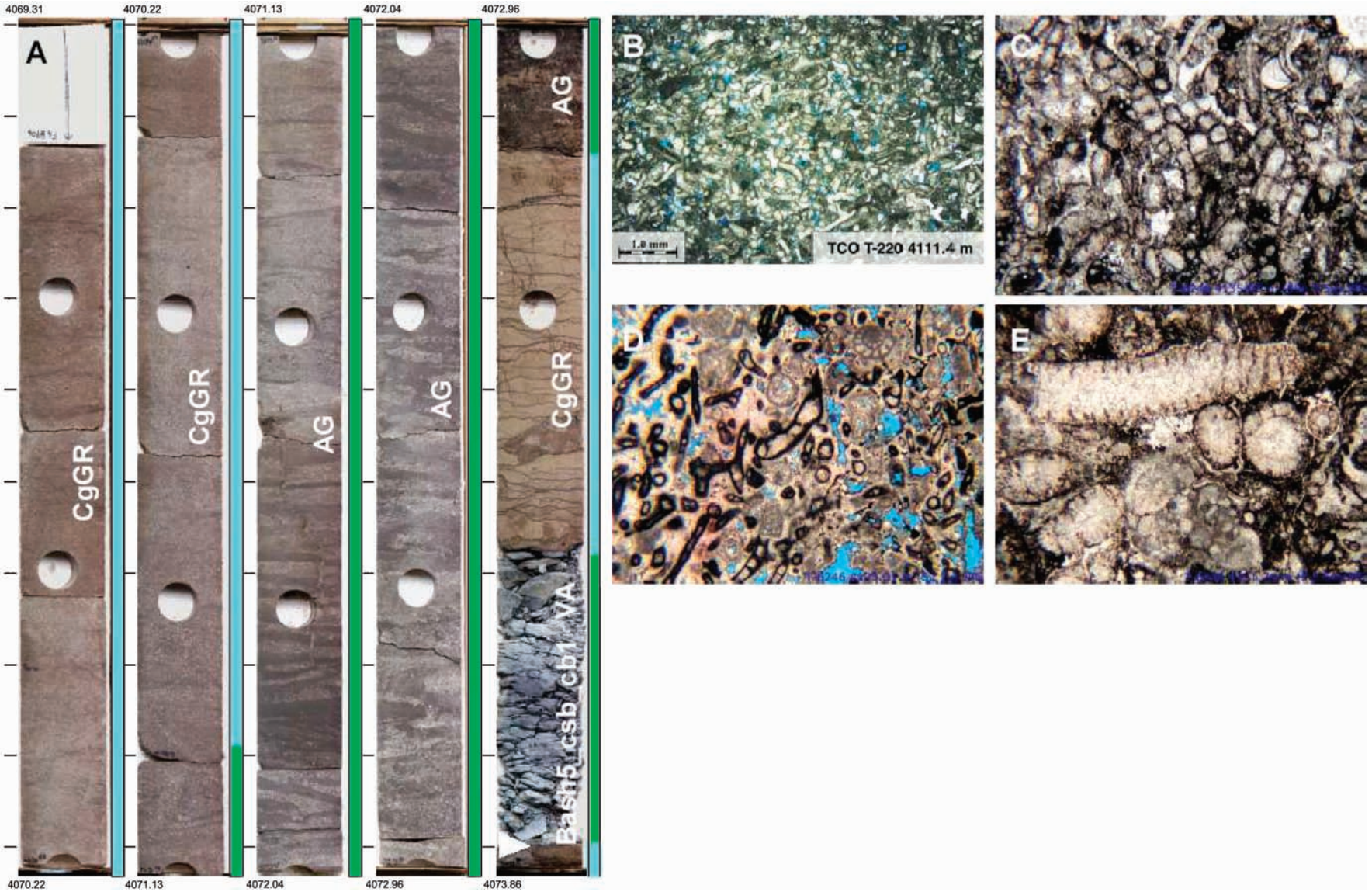

FIGURE 14. (A) Core photos from T-5246 show a thick interval of very well-sorted and cross-bedded, silt- to fine sand-size algal grainstone (AG) underlain and overlain by well-sorted coated-grain grainstone (CgGR); an interbed of volcanic ash (VA) occurs at the bottom (see Table 2 and Figure 5 for legend). Photomicrographs (B-E) show dominant grain types of AG: algal fragments, peloids, and uncommon benthic foraminifera. Typical algal species are *Donezella* (B, C), paleoberesellids such as *Kamaena* (D), and beresellids such as *Beresella* (E). Paleoberesellids are typically Visean and beresellids and *Donezella* occur in the Serpukhovian to Bashkirian. Width of photomicrographs is 4.20 and 1.58 mm (0.16 and 0.06 in.) (B, C-E, respectively).

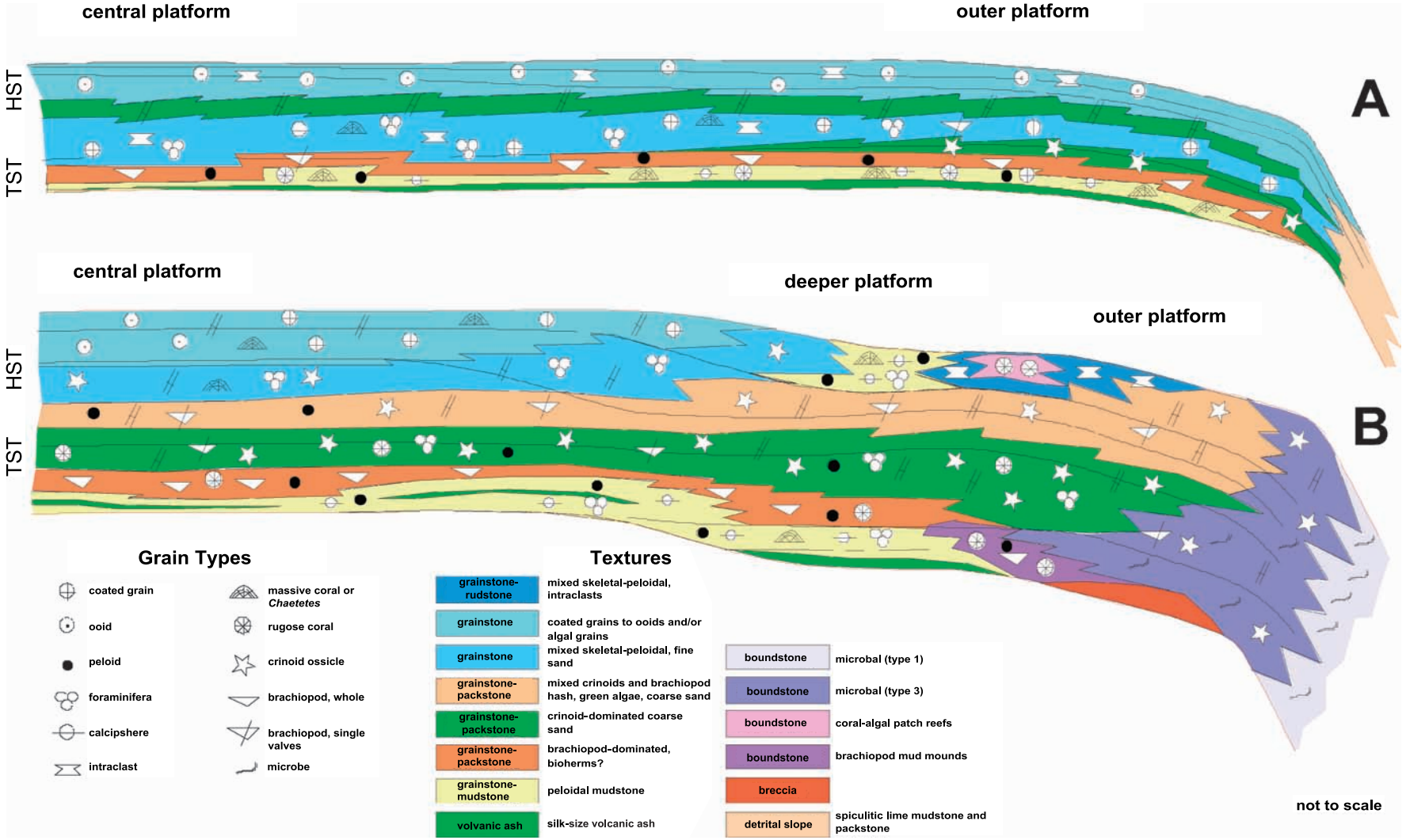

FIGURE 15. Models of hypothetical higher order depositional cycles for the Bashkirian (A) and the Visean A–Serphuhovian (B) showing grain composition and textural trends from the central Tengiz platform through the outer platform and into the flank. TST = transgressive systems tract; HST = highstand systems tract. See text for discussion.

the base, a thin, peloid packstone-wackestone that exhibits subaerial exposure features is commonly interbedded with thin volcanic ash layers. These lithofacies are overlain by brachiopod bioherms and/or crinoid skeletal-peloid grainstone-packstone, which are, in turn, overlain by poorly sorted skeletal-peloid grainstone-packstone and/or well-sorted skeletal grainstone. These lithofacies reflect lowstand and early transgressive restriction providing the environment for trapping volcanic ash fallout (peloid packstone-wackestone) and maximum flooding during the crinoid skeletal-peloid grainstone-packstone. This succession is succeeded by highstand deposits that indicate shoaling to (nearly) sea level: coated-grain grainstone-rudstone and/or ooid grainstone and locally a skeletal intraclast grainstone or algal grainstone. In the outer platform toward the east, cycles lack the lagoonal base and have a microbial boundstone interval (type 3 microbial boundstone; see Collins et al., 2006) instead, which is superceded by thicker poorly sorted mixed skeletal-peloidal and crinoid sand bodies. Some cycles include thin deposits of high-energy coated-grain grainstone-rudstone and/or ooid grainstone and skeletal intraclast grainstone or algal grainstone. Brachiopod bioherms, crinoid skeletal-peloid grainstone-packstone, and poorly sorted skeletal-peloid grainstone-packstone and/or well-sorted skeletal grainstone are absent.

The overlying Bashkirian cycles (Figure 15A) are thinner and, in the central platform, show alternating lagoonal peloid packstone-wackestone with subaerial exposure features and interbedded with thin volcanic ash layers, coated-grain grainstone-rudstone and/or ooid grainstone and skeletal intraclast grainstone. Above the Bash2.5_MFS, coated-grain grainstone-rudstone and/or ooid grainstone alternate with algal grainstone intervals, and volcanic ash beds are nearly absent. However, toward the outer platform areas, low-energy transgressive deposits (brachiopod skeletal-peloid grainstone-packstone, crinoid skeletal-peloid grainstone-packstone, poorly sorted skeletal-peloid grainstone-packstone) thicken and may even include microbial boundstone intervals (T-4556), while high-energy cycle tops (coated-grain grainstone-rudstone, ooid grainstone) are thinning or absent (T-6743).

Obviously, deviations from the generalizations of Figure 15 exist, as will be discussed in the following sections. Cycle thickness, stacking patterns, and relative contribution of each facies type vary within and across the major sequences. As an example, the bathymetric profile changes toward the Visean A–Serphukhovian outer platform to a deeper setting that brings microbial boundstone on the platform during flooding. In contrast, the Bashkirian sequence shows a flat-topped platform with parallel facies zones dominated by higher energy grainy lithofacies types. High-frequency cycles are much thinner in the Bashkirian, at meter scale, and show mostly alternating coated grain grainstone, ooid grainstone, and algal grainstone with sedimentary structures. The Bashkirian rim was probably flat during deposition and shows thinning of platform facies that border a nearly starved slope system.

Visean A and Serpukhovian: Trends and Depositional Environments

Visean A cycles consist almost entirely of grainy facies (packstone and grainstone) that feature depositional environments ranging from restricted low-energy brachiopod skeletal-peloid grainstone-packstone to moderate- to low-energy deeper subtidal environments characterized by more poorly sorted and open-marine poorly sorted skeletal-peloid grainstone-packstone as well as crinoid skeletal-peloid grainstone-packstone and high-energy well-sorted grainstone shoals (well-sorted skeletal grainstone and uncommon coated-grain grainstone-rudstone).

General trends in lithofacies distribution, cycle thickness, and stacking suggests the presence of three intervals in the Visean A and Serpukhovian reservoir zones, each displaying certain depositional trends (Figure 5). These are the intervals between the Lvis_SSB and Lvis10.5_csb, Lvis10.5_csb and Lvis13_csb (which straddles the second-order Lvis2_MFS), and Lvis13_csb to the Serp_SSB.

In the Lvis_SSB to Lvis10.5_csb interval, the platform cycles are dominated by the poorly sorted, open-marine poorly sorted skeletal-peloid grainstone-packstone, with minor intercalations of brachiopod skeletal-peloid grainstone-packstone and/or crinoid skeletal-peloid grainstone-packstone. Crinoid skeletal-peloid grainstone-packstone intercalations generally occur near the base of cycles, whereas well-sorted skeletal grainstone intercalations appear near the top. Cycle caps are thin, decimeter-thick, micropeloidal packstone-mudstone intervals that have, in nearly all cases, one or two thin volcanic ash interbeds, but generally display moderate subaerial exposure. Cycle thickness ranges from 1–2 m (3.3–6.6 ft) near the base to more than 15 m (49 ft) in the middle of the interval with an average of 5–8 m (16–26 ft). Poorly sorted skeletal-peloid grainstone-packstone intervals are dominant in the central platform around wells T-220 and T-5848 but gradually are partially replaced by higher energy sand shoals (well-sorted skeletal

grainstone) toward the outer platform areas (well T-5246 to the north and wells T-6246 and T-6846 to the southwest). Crinoid-rich intervals represent maximum, open-marine flooding and the deepest lithofacies. These occur preferentially in the outer platform toward the southwest and seem to thin and pinch out toward the central platform. One interval, however, runs contrary to this trend and appears to blanket the entire platform at the top of the Lvis_SSB to Lvis10.5_csb interval. Similarly, one nearly 10-m (33-ft)-thick and very continuous brachiopod skeletal-peloid grainstone-packstone interval covers the platform right above the Lvis9_csb boundary. This general depositional picture suggests an overall low-energy platform, subtidal or below wave base, with slightly shallower outer platform sand shoals and a dominant southern open-marine influence. The cycles in this succession never filled the total accommodation space, despite the relatively low-amplitude sea level oscillations.

The Lvis10.5_csb to Lvis13_csb interval, which straddles the supersequence flooding surface (Lvis2_MFS), shows a similar central versus outer platform facies pattern as the previous interval but has much thinner, 2–5-m (6.6–16-ft)-thick cycles and frequent brachiopod skeletal-peloid grainstone-packstone intervals. These brachiopod interbeds seem to thin away from the platform center and are replaced by higher energy mixed skeletal-peloidal sands to the south and high-energy, well-sorted sands to the north. In addition, the section has a crinoid-rich base, a thick interval of high-energy sand shoals in the middle, and a thick brachiopod interval (more than 10 m) near the top. Each of these intervals is continuous across the entire platform. The crinoid-dominated base indicates maximum deepening of the platform coinciding with the Lvis_MFS surface. Although relative depositional conditions did not change and accommodation space was still underfilled, it suggests that sea level fluctuations increased in frequency.

The Lvis13_csb to the Serp_SSB interval in the HSS of the supersequence has similar thin cycles, 2–5 m (6.6–16 ft) in thickness, but those show more pronounced subaerial exposure near the cycle tops. Furthermore, there is an overall trend of higher energy coated-grain and ooid sand shoal deposits with elevated amounts of dispersed volcanic ash toward the north (wells T-5447, T-5044, and T-5444) and slightly deeper, lower energy, environments toward the south, near the outer platform (wells T-6246 and T-6846). Cycles were nearly completely filled in the northern platform area, multiple ash layers occur near sequence boundaries, and there is an increased expression of exposure toward the Serp_SSB. These observations suggest the development of a slightly deeper and lower energy outer platform toward the southeastern margin (possibly caused by structural tilting). The thinning of cycles, increasing exposure of cycle tops, and lateral facies differentiation during the Serpukhovian coincide with the development of an unusual deeper water outer platform toward the northeastern to eastern margins of the Tengiz platform, where upper slope facies consisting of algal-microbial, skeletal-microbial, and microbial boundstone prograded several kilometers out into the basin on a preexisting Visean A and B shelf edge. In these regions of the outer platform, which generally have lower energy and probably deeper water facies, exposure expression is reduced or absent (see Figure 15).

Bashkirian: Trends and Depositional Environments

Bashkirian cycles are thinner and less systematic than those recognized in the Visean A and Serpukhovian, most likely because of rapid sea level fluctuations produced during global icehouse conditions. The Bashkirian consists of three intervals, of which the lower (Serp_SSB to Bash1_csb) is essentially a 15–20-m (49–66-ft)-thick ooid sand body covering the entire platform (Figure 5). This unit is nearly tabular in shape, has locally thin, mixed skeletal-peloidal open-marine intercalations, and is cyclic with thin mudstone cycle caps and associated exposure surfaces. In the central platform, the lower half of the interval commonly contains high bitumen content and has low porosity; toward the southwestern outer platform (T-6246) and north (T-5246), nearly the entire section has bitumen and strongly reduced porosity. The middle part of the Bashkirian is bounded above by a stratigraphic surface (Bash2.5_MFS) that was not part of the original framework published by Weber et al. (2003). The Bash1_csb to Bash2.5_MFS is dominated by thin (a few meters) shoaling cycles of sorted skeletal subtidal open-marine sands, overlain by high-energy intertidal coated grain to ooid sand shoals, and capped by thin peloidal packstone-mudstone intervals with general extensive subaerial exposure and intercalated centimeter- to decimeter-thick volcanic ash beds. In the uppermost part of the Bashkirian (Bash2.5_MFS to Bash_SSB), ooid to coated grain sands occur in the basal part of shoaling cycles and are overlain by silt-size (high-angle), cross-bedded, well-sorted algal sands. Lagoonal packstone-mudstone intervals and associated volcanic ash beds are uncommon or

lacking completely. The algal fragments are silt-size, dominant, and probably tubular red algae in origin.

The waning of ooid domination and introduction of algal silt above the Bash2.5_MFS may indicate a general deepening stratigraphic trend toward the Bash_SSB, which is consistent with an interpretation of the subsequent drowning of the platform (Weber et al., 2003). Cross-bedding was possibly generated by oceanic currents sweeping the deeper water platform top during the progressively longer highstands; the platform was still exposed during shorter lowstands associated with high-frequency and high-amplitude (as much as 40–60-m [131–196-ft]) sea level changes of the icehouse world. Expressions of subaerial exposure, such as dissolution, recrystallization, and preservation of ash layers are also nonuniform from cycle to cycle. Despite this, Bashkirian cycles retain some similarities to Visean A and Serpukhovian cycles, such as the presence of high-energy shoals and deeper platform skeletal grainstone and the association of semirestricted to restricted facies near sequence boundaries. In the Bashkirian, high-energy shoals are represented by oolites, pisolites, and coated grains, whereas the deeper and restricted facies are similar to those present in the Serpukhovian and Visean A.

Interplay between Minor Tilting and Deposition

A remarkable observation from the cross section in Figure 5 is that the railroad-track pattern of sequence and cycle boundaries below the Serp_SSB is nearly perfectly parallel, with the exception of the section in T-6846. Another observation is the presence of a minor angular unconformity of several degrees between the Serp_SSB and the underlying cycle breaks, wherein both the Serp_SSB and cycle breaks dip to the south a few degrees. In addition, the Serp_SSB appears to have variable erosional relief of as much as 5 m (16 ft) across the platform as indicated by the apparent increased erosion in well T-5447. These observations suggest several things. First, fairly gradual and constant vertical aggradation across the central platform resulted in a flat platform top with minimal local relief as a result of immediate compensation of possible variations in depositional topography. In addition, the platform was tilted to the south prior to the Serp_SSB, subsequently eroded (based on the missing Bogdanovsky and Suryansky biozones), generating as much as 5-m (16-ft) relief, and finally, tilted a few more degrees along the same axis during the post-Bashkirian. Well T-6846 shows about a 5-m (16-ft) thicker section relative to other wells of Figure 5 between the Lvis10.5_csb and Lvis_SSB, a nearly 5-m (16-ft) thicker section between the Lvis13_csb and Lvis10.5_csb, probable minor erosion at the Lvis13_csb, and several additional meters missing section below the Serp_SSB. Although not proven, these differences may indicate that the southwestern margin tilted downward some 10 m (33 ft) or more prior to the Serp_SSB and was eroded at the time of the Serp_SSB following minor tilting to the north.

RESERVOIR QUALITY AND DIAGENESIS

Pore Types

Air permeability data from approximately 11,000 plugs clearly suggest the presence of three general reservoir environments based on plug-scale matrix properties: central platform, outer platform, and rim slope (flank) (Collins et al., 2006). The Visean A, Serpukhovian, and Bashkirian central platform reservoir can be regarded as having distinctly different gross reservoir properties that are generally well behaved as a whole. Porosity-permeability crossplots and porosity histograms suggest different behavior between the northern wells (T-220 and T-5246) and southern wells (T-6246 and T-6846) in the central platform (Figure 16). Trends of generally lower mean porosities and better behaved porosity-permeability relationships occur in the southern wells, whereas bimodal porosity distributions occur in the northern wells. Pore-type characterization of nearly 2000 plugs (and associated thin sections) from the nearly bitumen-free T-220 well and the moderately bitumen-cemented T-6246 well show the presence of varied pore types like moldic, vugs, microporosity, interparticle porosity, intercrystalline, and intraparticle porosity and the general absence of fractures (Figure 17).

The porosity classification scheme of Choquette and Pray (1970) defined numerous carbonate pore types, either fabric selective (including interparticle, intraparticle, intercrystalline, and moldic) or not fabric selective (including fracture and vug). There were implications for porosity-permeability relationships, of course, but this was not emphasized. Lucia's (1995, 1999) landmark study showing the direct link between rock type, porosity type, and reservoir quality (porosity-permeability relationships or transforms) changed the context of some of these classic pore types. Lucia (1995, 1999) recognized interparticle pore types and vuggy pore types. Interparticle pores, which have a more straightforward porosity-permeability transform that can be tied to rock type, grain size, and sorting, are instances where the pore space occurs between particles and is not significantly larger that the particles.

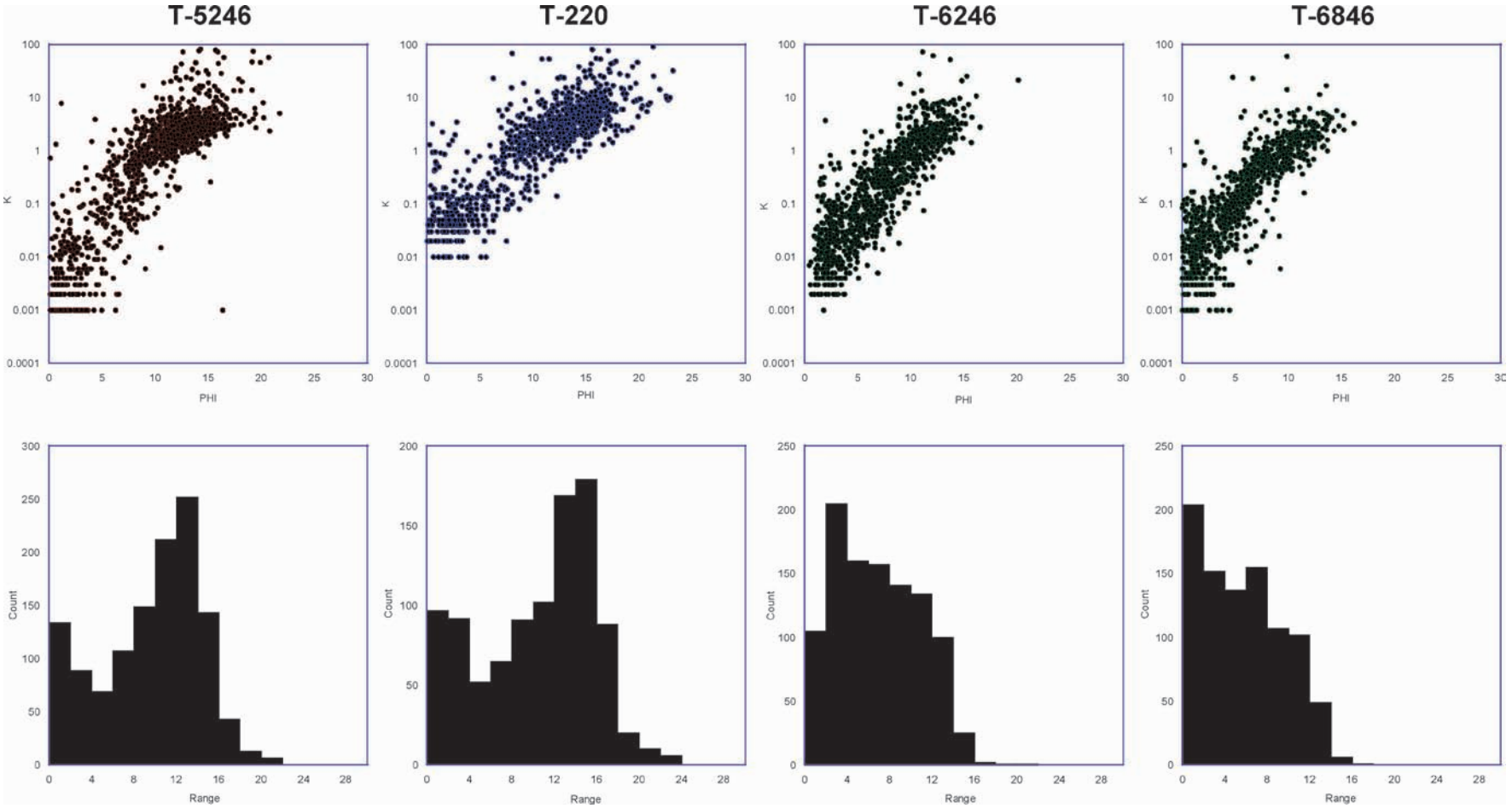

FIGURE 16. Subtle porosity-permeability differences are observed between four wells in the central platform; see Figure 4 for well locations and Figure 5 for their facies and stratigraphy. K-Phi plots (top) and porosity histograms (bottom) suggest different behavior between the northern wells (T-220 and T-5246) and southern wells (T-6246 and T-6846) with generally lower mean porosities and better behaved permeability-porosity relationships in the southern wells and bimodal porosity distributions in the northern wells.

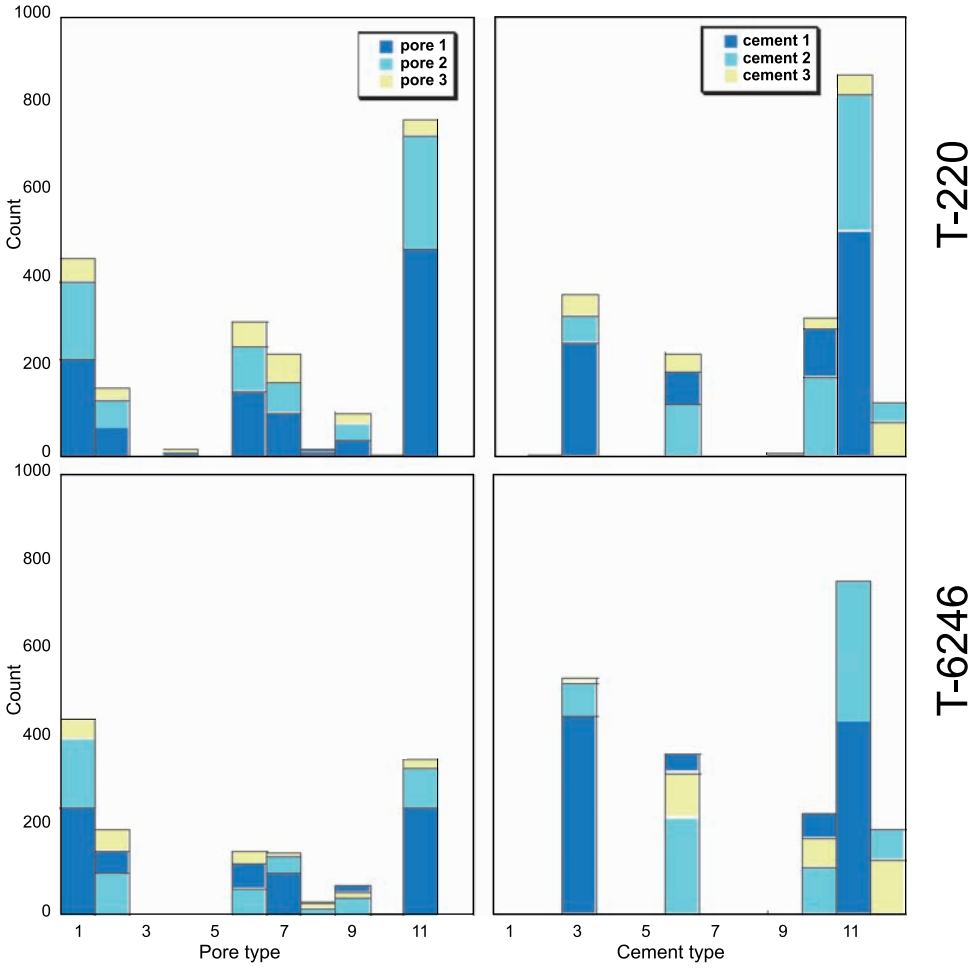

FIGURE 17. Pore and cement types recognized in the T-220 and T-6246 wells are generally similar. However, relative contributions by vuggy, intercrystalline, and moldic pore types are significantly higher in T-220 for all facies types than in T-6246, which may be related to the larger average grain size and higher contribution by the mud-lean rock types in T-6246. Similarly, cement types in T-6246 show a higher abundance (frequency) of equant calcite and syntaxial cements than in T-220. This may suggest a larger volume of deep burial cements filling pores at T-6246, but clearly, more quantitative data are required for such assessment. Pore types across the bottom of the figures are 1 = interparticle; 2 = intraparticle; 3 = fenestral; 4 = shelter; 5 = growth framework; 6 = intercrystalline; 7 = moldic; 8 = microporosity; 9 = fracture; 10 = channel; 11 = vug; and 12 = enhanced dissolution. Cement types are 1 = fibrous; 2 = bladed; 3 = equant to rhombic; 4 = coarse crystalline; 5 = botryoidal; 6 = syntaxial; 7 = micritic; 8 = meniscus; 9 = microstalactitic; 10 = poikilotopic; 11 = neomorphic spar; and 12 = grain rims. Plotted are relative dominance of pore or cement types in terms of visual presence with the number indicating their ranking. See text for discussion.

Vuggy pore types are typically larger than the grains or occur within the grains, and these can be separate or touching. Separate vugs are connected through the interparticle pore system, whereas touching vugs themselves form an interconnected system.

At Tengiz, separate vugs that add to porosity but not permeability include moldic and intraparticle porosity, so these must be subtracted from total porosity to use interparticle transforms. Touching pore types include some vugs (solution-enlarged interparticle pores) and fractures, which add porosity and permeability independently from the interparticle component, such that interparticle transforms must be modified. Clearly, real-world reservoirs in limestone can be even more complex with the addition of microfractures, intercrystalline porosity, or microporosity connecting separate vugs, and/or the problem of assessing in two dimensions with petrography the three-dimensional complexity of porosity. The following sections describe the pore types commonly observed in Tengiz samples and their relative abundance in the central platform.

Pore types were identified in the Tengiz cores and thin sections generally following the terminology of Choquette and Pray (1970) to first assess their relation to lithofacies and then explore the relation

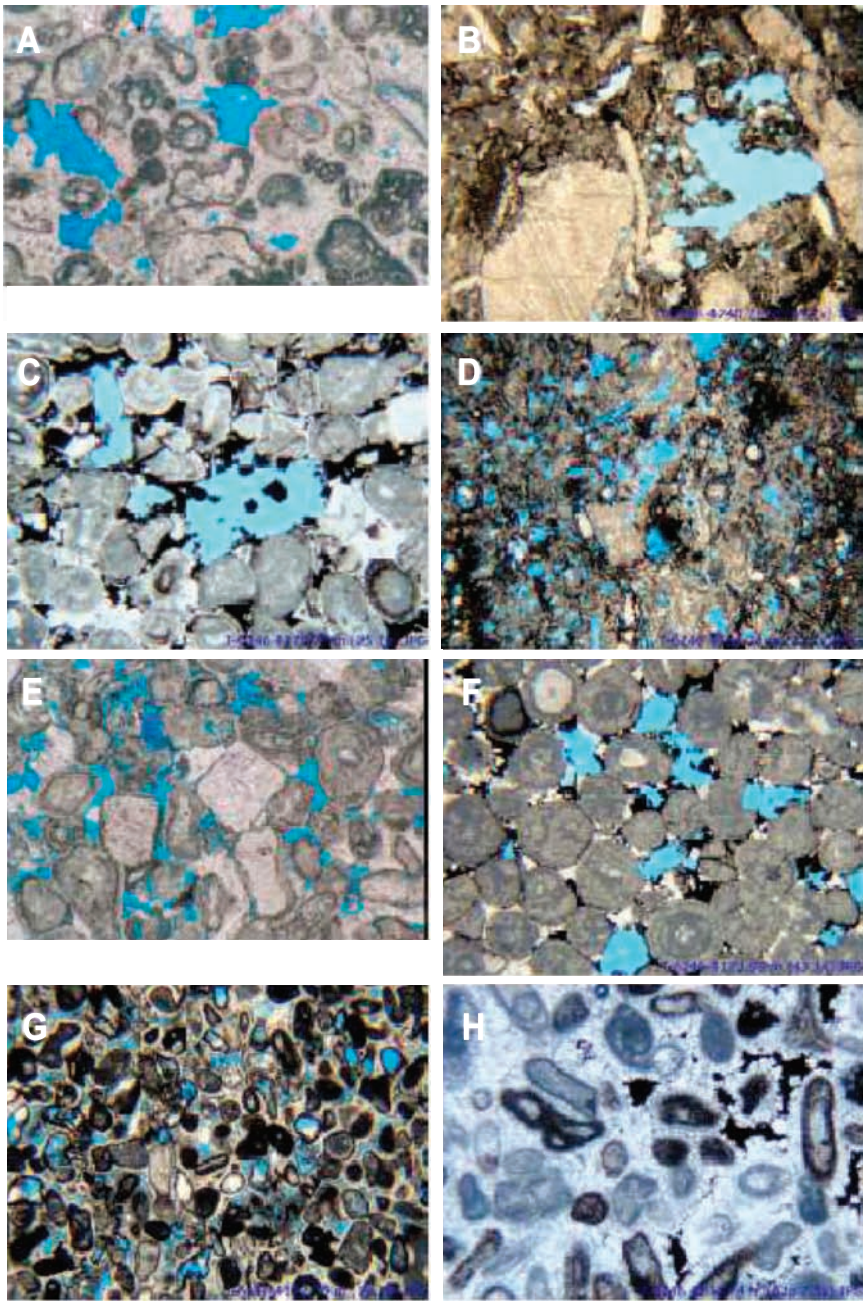

FIGURE 18. Photomicrographs illustrating the dominant pore types in the central platform area. (A) Vugs are nonfabric-selective pores commonly larger than the dominant grain size (although different interpretations exist in the literature). Examples of vugs shown here are the result of enhanced dissolution in a grainstone following early equant rim cementation. (B) Vugs developed in a packstone-grainstone, dissolving both grains and matrix but leaving crinoid ossicles and brachiopod fragments intact. (C) Overpacked ooid grainstone with vugs that postdate early cementation but predate blocky calcite and bitumen emplacement. Vugs are a dominant pore type in the central platform and seem to be mostly related to deep-burial dissolution instead of initial meteoric processes. (D) Advanced stage of enhanced dissolution of moldic and interparticle porosity (and minor intraparticle) leading to the destruction of cement bridges and development of vugs. (E) Skeletal and coated grain grainstone dominated by interparticle porosity with minor cement fill. (F) Overpacked ooid grainstone with minor blocky calcite and bitumen occluding solution-enhanced interparticle porosity. (G) Skeletal and peloid grainstone with rims of equant spar lining interparticle pores and minor moldic porosity. (H) An example where the interparticle porosity is completely occluded by equant to rhombic spar and bitumen cement. Width of photomicrographs is 4.20 and 1.58 mm (0.16 and 0.06 mm) (A–G, H, respectively). See text for discussion.

between lithofacies and reservoir quality (Table 2). Common pore types in the Tengiz central platform are vugs, interparticle, microporosity, intercrystalline, moldic, and intraparticle with generally the highest permeability occurring in vuggy-dominated matrix. The most common pore type is vuggy, which is, in part, fabric selective, being found in matrix, grainy areas (solution-enhanced interparticle pores), or associated with stylolites (Figure 18A–C). The second most common pore type is interparticle porosity (Figure 18D–H), followed by microporosity (Figure 19A, B).

Vuggy porosity includes moldic porosity when considered in terms of porosity-permeability transforms (Lucia, 1995, 1999). Figure 19C–E shows successive stages of the development of moldic porosity at Tengiz: in its early phase where micrite grains are gradually being dissolved following partial fill of interparticle porosity by equant to rhombic spar cement (Figure 19C); a phase of progressive dissolution shown by corrosion of the mold boundaries, nearly breaking through at contacts and corroding earlier cement (Figure 19D); and an advanced stage where enhanced dissolution left only micrite envelopes. Intraparticle porosity, which is also included as vugs in terms of porosity-permeability transforms, is shown in Figure 19D–F.

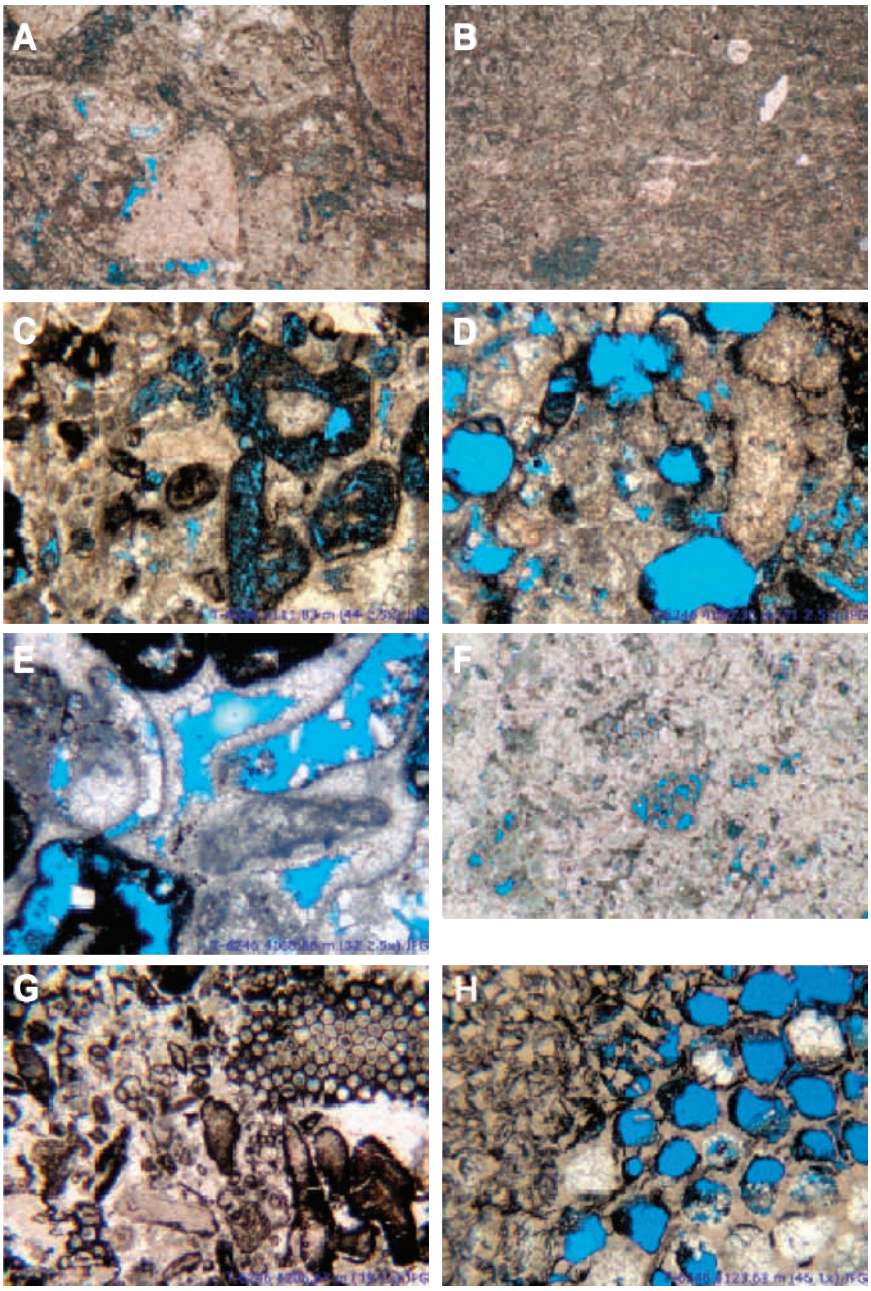

FIGURE 19. Photomicrographs illustrating additional dominant pore types in the central platform area. (A, B) Examples of microporosity, pore size smaller than 25 μm, developed in grains (A) and matrix (B). This type of pore is generally difficult to observe in thin sections because of their thickness, commonly about 25–45 μm. (C) Moldic porosity in its early phase: micrite grains are gradually being dissolved following partial fill of interparticle porosity by equant to rhombic spar cement. (D) Moldic porosity showing evidence for enhanced dissolution shown by corrosion of the mold boundaries, nearly breaking through at contacts and corroding earlier cement. (E) Moldic porosity showing further stage of enhanced dissolution leaving only micrite envelopes. Bitumen-stained micrite appears to slow down dissolution. Interparticle porosity is partially filled with calcite cement. (F) Intraparticle porosity developed in benthic foraminifera. (G) Intraparticle porosity developed in a green alga, *Koninckopora*. (H) Intraparticle porosity developed in a *Chaetetes* fragment (not all pores are filled by blue epoxy). Width of photomicrographs is 4.20 mm (0.16 in.) (A, B, F, G) and 1.58 mm (0.06 in.) (C, D, E, H). See text for discussion.

Examples of an advanced stage of dissolution of moldic and interparticle porosity leading to the destruction of cement bridges and development of vugs with minor blocky calcite and bitumen occluding porosity are shown in Figure 18D and F. Commonly, moldic porosity co-occurs with interparticle porosity as shown in Figure 18G; interparticle porosity is completely occluded by equant to rhombic spar and bitumen in some samples (Figure 18H). Microporosity in grains or matrix is difficult to observe in Tengiz samples because pore sizes are much smaller than the thickness of a typical thin section. Microporosity includes fine intercrystalline porosity because both are generally beyond normal petrographic resolution and, therefore, difficult to distinguish. Fractures and fissures are generally uncommon in the central platform, and where present, they are mostly occluded by cement. In some few cases where the fractures remain open, they range from microhairline fissures to sharp microfractures (Figure 20A–F). Stylolites are generally stained by bitumen and commonly associated with small vugs (Figure 21A–C). Examples demonstrate that such dissolution postdates stylolite formation.

Parameters Controlling Porosity and Permeability

The relative contributions by vuggy, moldic, and intercrystalline porosity are significantly higher for all facies types in well T-220 than in well T-6246. In contrast, the relative contribution by interparticle porosity is higher at T-6246, a change that is most likely related to the higher percentage of grainy, mud-lean

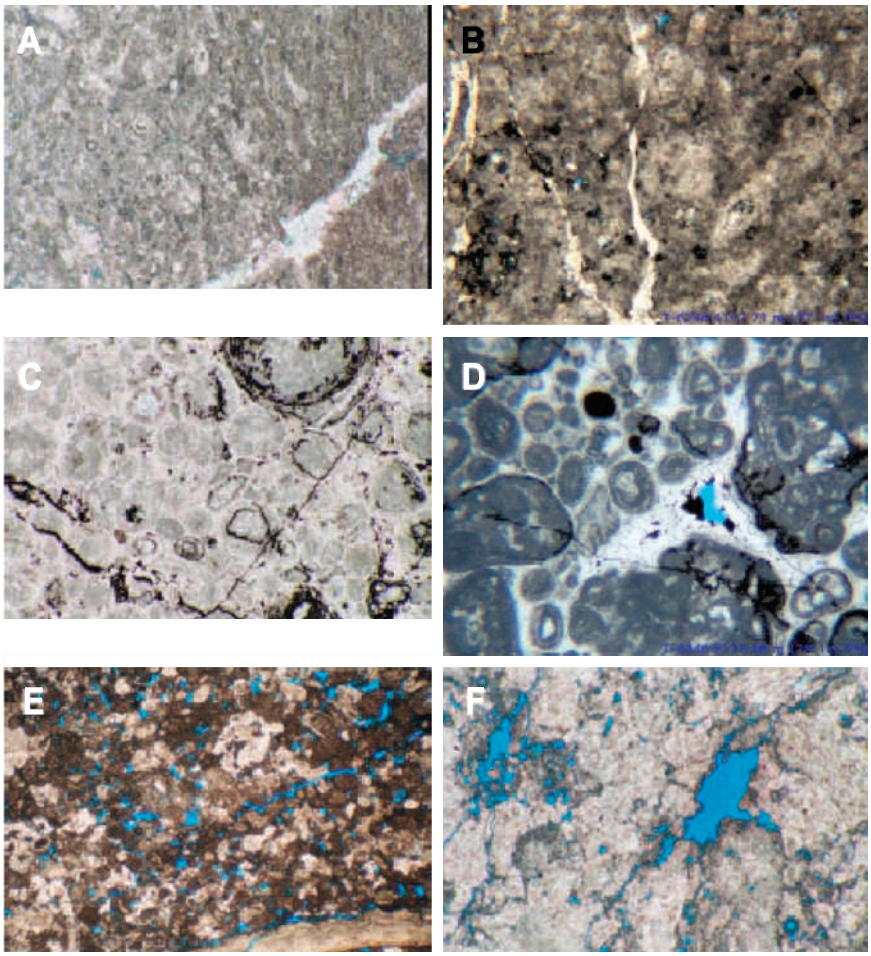

FIGURE 20. Photomicrographs illustrating dominant pore types in the central platform area. (A, B) Generating thin sections from core plugs with open fractures is difficult if not impossible. Shown here are examples of thin fractures that are filled by blocky calcite cement. (C, D) Examples of hairline fissures or fractures filled by bitumen. Note that the fissure in (C) postdates blocky calcite interparticle cement fill but predates bitumen emplacement and confirms the very late timing of bitumen invasion. (E, F) An exception to the rule: vague outline of open fractures that have been enhanced by late-stage dissolution in a skeletal-peloidal grainstone with high interparticle porosity. Fractures may connect vugs as shown in these samples. Width of photomicrographs is 4.20 mm (0.16 in.). See text for discussion.

rock types in that well (Figure 22). Nevertheless, at a gross scale, none of the individual pore types or combination of pore types seem to have a significant first-order relationship with primary depositional facies nor have any significant control on porosity or permeability. This suggests that the central platform area could be regarded as one single reservoir region wherein changing pore types and lithofacies do not significantly impact true reservoir connectivity. This suggestion is rather surprising and seemingly contradicts Lucia's (1995, 1999) reservoir rock-type classification that suggests pore types control permeability behavior.

Although the observations above suggest minimal first-order control by pore type or facies, several second-order relationships should be acknowledged. Porosity distributions and pore-type contributions for the muddy lagoonal facies (peloid packstone-wackestone), moderately sorted grainy facies with mud matrix (brachiopod skeletal-peloid grainstone-packstone, crinoid skeletal-peloid grainstone-packstone, and poorly sorted skeletal-peloid grainstone-packstone) and mud-lean well-sorted grainy facies (well-sorted skeletal grainstone, coated-grain grainstone-rudstone, ooid grainstone, skeletal intraclast grainstone, and algal grainstone) that make up the cyclic pattern shown in Figure 5 do show subtle but significant differences (Figure 22). Pore type contributions in the grainy facies groups are very similar, but muddy lagoonal facies have a higher contribution of intraparticle and fracture porosity. The grainy facies in well T-6246 have a higher contribution of interparticle porosity but also differ in the overall distribution of porosity. These distributions are remarkably different between the two wells with bimodal and generally higher porosities in grainy facies and low porosities in lagoonal facies in well T-220, whereas the porosity distributions in well T-6246 show highly reduced and flattened distributions for the mud-lean facies compared to T-220 (Figure 23). Similarly, the mud-rich grainy facies have reduced porosity, but the lagoonal mudstone has higher porosity, displaying a bimodal distribution that is possibly related to a higher contribution of fracture porosity. The above suggests that T-220 porosity has a relatively higher contribution by pore types that are the result of corrosive processes, like vug and moldic porosity, an observation that can be made for T-5246 as well.

In addition to pore type, observations were made on the type of pore-filling agents, which resulted in two significant trends. First, the distribution of pore-filling cement types for both wells T-220 and T-6246

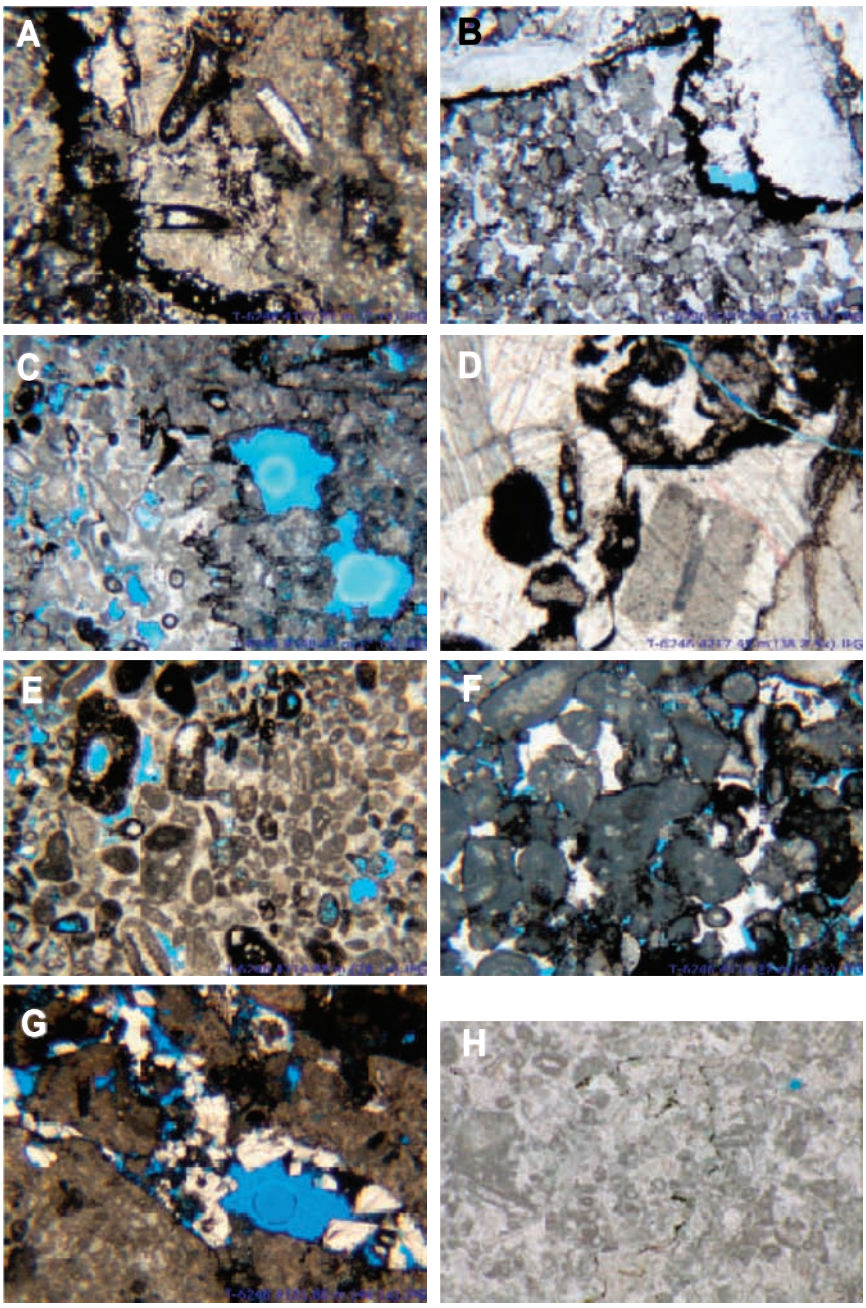

FIGURE 21. Photomicrographs illustrating the dominant pore types in the central platform area. (A) Pressure solution stylolite with dark-brown micrite and possibly bitumen. (B) As in (A), but dissolution associated with stylolite. (C) As in (A, B), but here, dissolution postdating stylolite formation is clearly visible; note that the vug is not breaking through the bitumen seam. (D) Poikilotopic syntaxial overgrowth cements on crinoid ossicles are locally dominant and reduce interparticle porosity. However, invasion by bitumen and associated dissolution was able to corrode cement and crinoid ossicles. (E) Coated grainstone where equant to rhombic spar is occluding interparticle pore space, probably replacing earlier marine cements, and only sparse molds and remaining interparticle pores remain. (F) Micritized coated grainstone with evidence for minor corrosion of grain boundaries followed by burial blocky calcite that occludes part of the interparticle porosity. Micrite is locally invaded by bitumen. (G) Detail of partially open fracture that was occluded by blocky calcite cement and followed by bitumen. (H) Porosity in poorly sorted grainstone was occluded by cement and completely recrystallized to fine calcite spar cement. Width of photomicrographs is 4.20 mm (0.16 in.) (A–C, E–H) and 1.58 mm (0.06 in.) (D). See text for discussion.

appears to be comparable, with the exception of a relatively higher contribution by equant and syntaxial calcite at T-6246 (Figure 17). Another obvious difference between the T-220 and T-6246 wells is the amount of bitumen; Figure 5 shows qualitatively higher amounts of bitumen in T-6246 (and T-6846) than in T-220. For well T-220, bitumen volume is mostly associated with muddy grain-rich to mud-rich facies (Figure 24A) and dominant pore types like interparticle, intercrystalline, and vug with minor contributions by intraparticle, moldic, and fracture (Figure 24B). Bitumen content shows a negative relationship with porosity (Figure 24C) and permeability (Figure 24D).

Figure 25 better shows the influence of bitumen volume on the porosity versus permeability relationship in well T-220 (no such data are yet available for T-6246). Increasing bitumen content above a threshold of approximately 0.5% rock volume is negatively correlated with K-Phi. Although bitumen commonly occurs in grainy facies with matrix pore types, it also occurs with late diagenetic pore types like vugs as well as with nonmatrix pore types like fractures. Bitumen content significantly impacts the cyclic and stratigraphic porosity variations as shown by Figure 26; it also causes the observed decrease in porosity toward the outer platform. Porosity logs corrected for bitumen volume are easier to correlate and confirm that the distribution of bitumen increases toward the outer platform (Figure 26). Clearly, bitumen reduced the porosity toward the outer part of the central platform and even more so into the outer platform itself (Figures 4, 5).

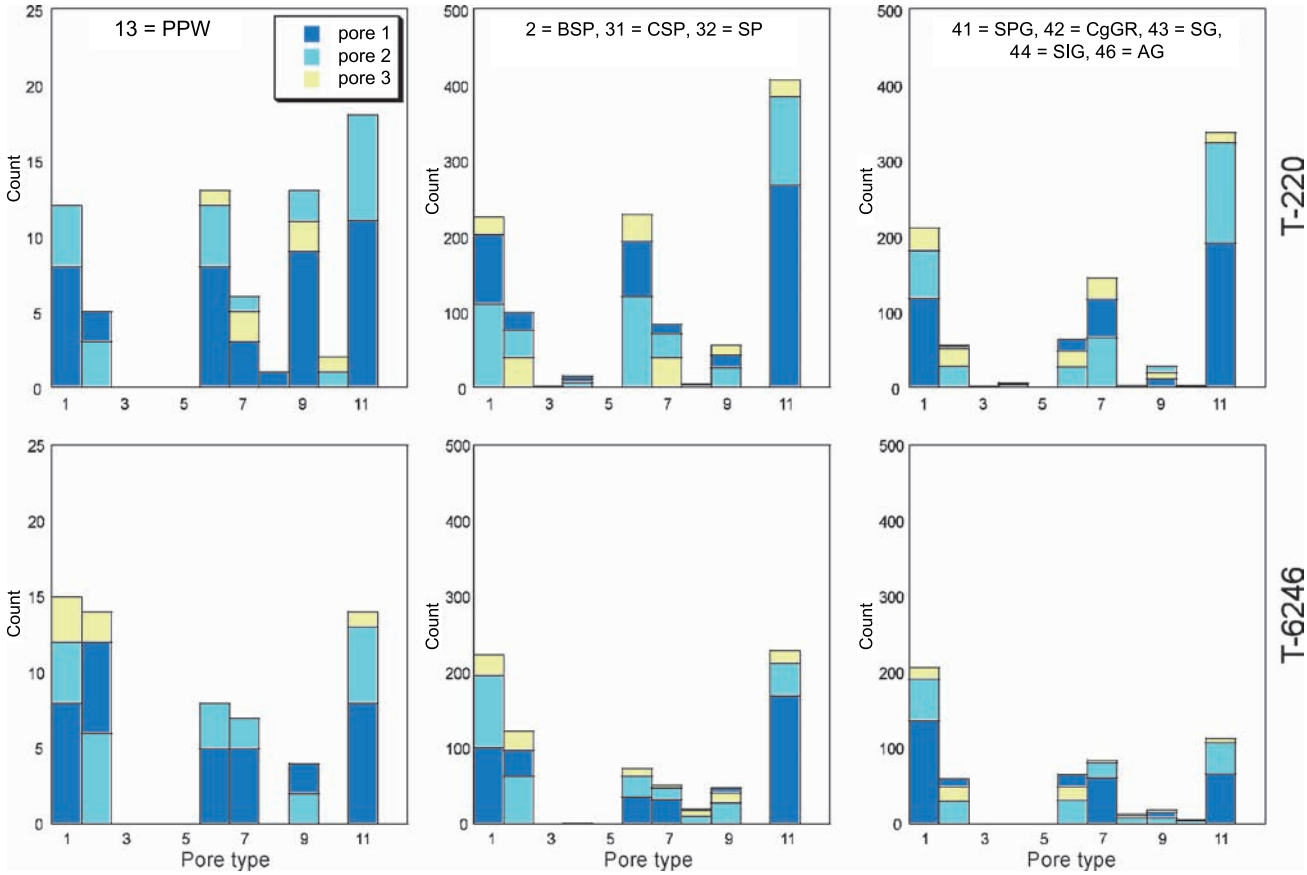

FIGURE 22. Pore-type contributions for muddy lagoonal facies (13 = PPW) and moderately sorted grainy facies with mud matrix (2 = BSP, 31 = CSP, 32 = SPP) and mud-lean, well-sorted grainy facies (41 = SPG, 42 = CgGR, 43 = OG, 44 = SIG, 46 = AG) in both T-220 and T-6246 wells. Pore types are 1 = interparticle; 2 = intraparticle; 3 = fenestral; 4 = shelter; 5 = growth framework; 6 = intercrystalline; 7 = moldic; 8 = microporosity; 9 = fracture; 10 = channel; 11 = vug; and 12 = enhanced dissolution. Plotted are relative dominance of pore types in terms of visual presence with the number indicating whether pore types were first, second, or third in importance. See text for discussion.

Volcanic ash also produces low-porosity (tight) zones. These tight zones tend to occur around cycle boundaries and within intervals that have dispersed volcanic ash. One mechanism explaining these observations associates volcanic ash with inhibited downward fluid percolation during early diagenesis associated with sequence and cycle boundaries. This condition generally reduced the effect of meteoric dissolution. In addition, silica leached from the volcanic ash was, in some cases, redeposited as chert and silica cement below the sequence boundaries, thereby adding to the porosity reduction of the associated lagoonal intervals. Finally, the dissolution associated with the bitumen emplacement did not affect those tight zones.

Processes and Timing of Diagenesis

The present-day distribution of reservoir quality in the central and (southwestern) outer platform in the Lvis_SSB to Bash_SSB platform succession (Visean A, Serpukhovian, and Bashkirian reservoir zones) was determined by the combined effect of late diagenetic modification, specifically bitumen invasion and associated corrosion, of an earlier reservoir system whose porosity and permeability distribution was established by highly cyclic depositional and early diagenetic processes (Figure 27). Early diagenesis includes meteoric alteration in cyclic platform facies associated with major sequence boundaries and reduced dissolution along sequence and high-order cycle boundaries associated with the presence of volcanic ash. Diagenetic processes associated with subaerial exposure produced both an increase and reduction of porosity (Figure 27). Brown fibrous, mycrostalactitic, meniscus, and pendant cements are commonly associated with meteoric vadose and marine vadose diagenesis, and these are observed in Tengiz cores to several meters below a suspected exposure surface (Figure 28A–D). Possible examples of alveolar fabrics indicating soil formation below an exposure surface are shown in Figure 28E. Early dissolution related to

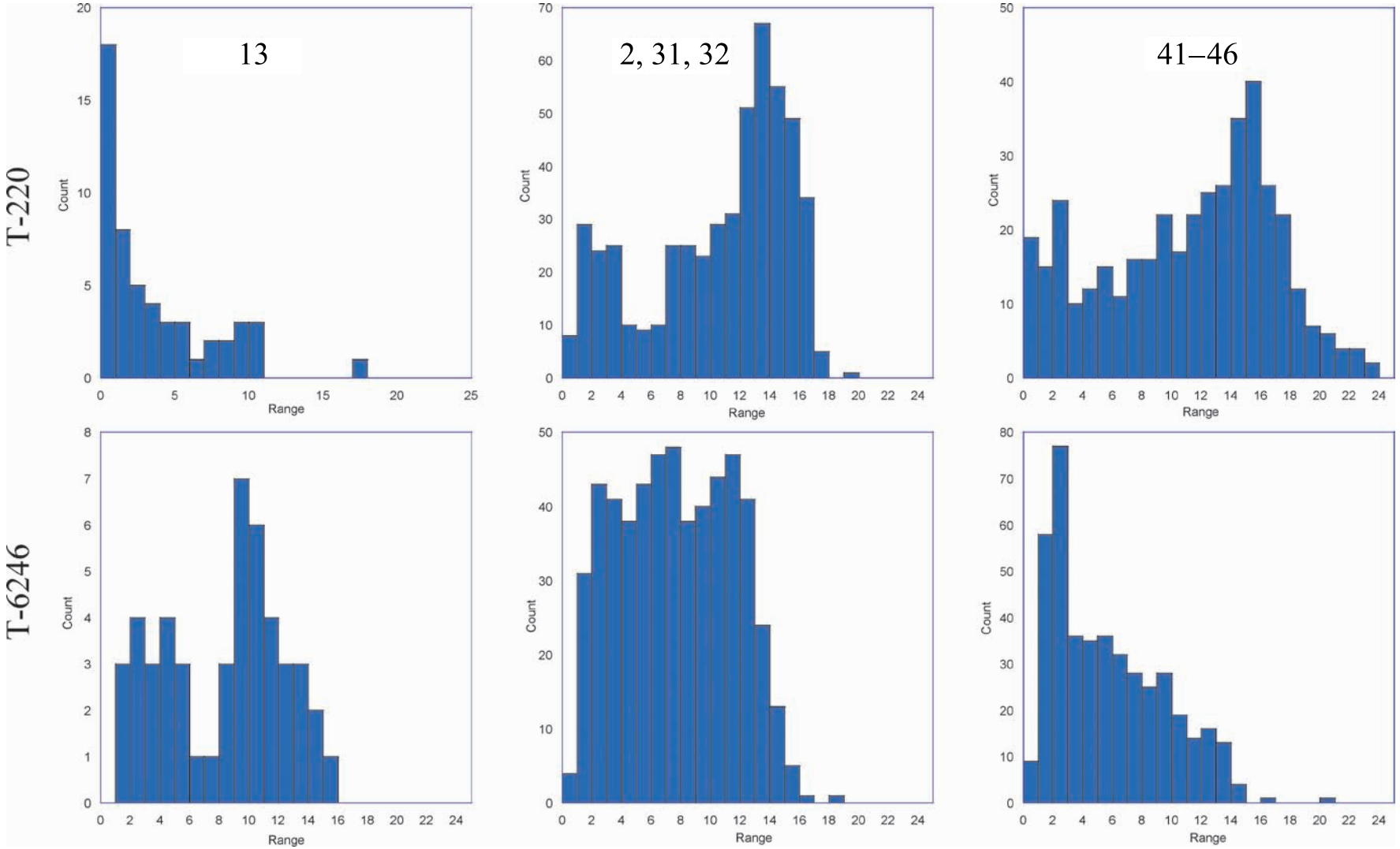

FIGURE 23. Porosity distributions for the major facies types in T-220 and T-6246: muddy lagoonal facies (13 = PPW), moderately sorted grainy facies with mud matrix (2 = BSP, 31 = CSP, 32 = SPP), and mud-lean well-sorted grainy facies (41 = SPG, 42 = CgGR, 43 = OG, 44 = SIG, 46 = AG). See text for discussion.

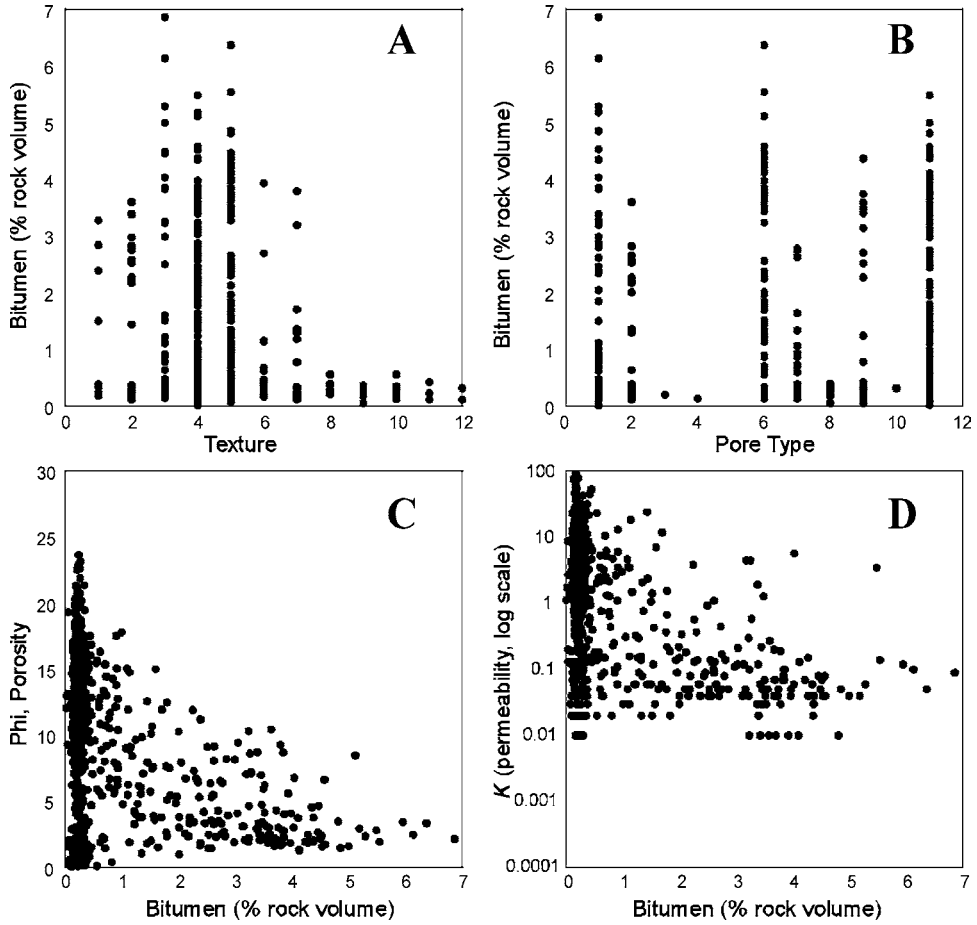

FIGURE 24. **Relationship between bitumen (Bit rock), rock fabric (PP fabric), pore type (pore 1), porosity (Phi), and permeability (*K*) in well T-220 (no such data are yet available for T-6246). Bitumen content is mostly associated with grainy mud-lean to mud-rich facies (A) and dominantly in interparticle, intercrystalline, and vug pore types with minor contributions by intraparticle, moldic, and fracture pores (B). Bitumen contents above 0.5% rock volume shows a negative relationship with porosity (C) and permeability (D). Pore types are 1 = interparticle; 2 = intraparticle; 3 = fenestral; 4 = shelter; 5 = growth framework; 6 = intercrystalline; 7 = moldic; 8 = microporosity; 9 = fracture; 10 = channel; 11 = vug; and 12 = enhanced dissolution. Textures are 1 = rudstone; 2 = grainstone-rudstone; 3 = grainstone; 4 = grainstone-packstone; 5 = packstone-grainstone; 6 = packstone; 7 = packstone-wackestone; 7 = wackestone-packstone; 8 = wackestone; 9 = wackestone-mudstone; 10 = mudstone-wackestone; 11 = mudstone; and 12 = boundstone. See text for discussion.**

exposure may have led to early compaction as shown by the frequent occurrence of fitted fabrics (Figure 28H), where the thin cement rim is included in the compaction and postdated by blocky calcite cement and bitumen.

Later stage diagenesis includes pressure solution culminating in stylolites with concentrations of dark-brown micrite and bitumen (Figure 21A, B). Dissolution is sometimes observed postdating the stylolite formation (Figure 21C). Poikilotopic syntaxial overgrowth cements on crinoid ossicles are locally a dominant cement, reducing interparticle porosity (Figure 21D). Later burial processes also reduced porosity by cementation and recrystallization (Figure 21E–H). Examples show progressive occlusion of pore space during this process, which includes cementation of pore space created by fracturing (Figure 21G).

Burial dissolution events that added porosity are of great interest and paramount importance to the Tengiz reservoir and its interpretation with respect to porosity modeling (Figure 29A–F). A very common observation in samples that have interparticle porosity is enhanced (late-burial?) dissolution that enlarges and connects interparticle pore space into larger vugs. These vugs are lined by bitumen, attesting to the timing of the dissolution relative to bitumen emplacement (Figure 29A). Grain boundaries are commonly corroded by this dissolution event, as is syntaxial overgrowth cement in some cases (Figure 29B, C). Extensive late deep burial dissolution prior to oil migration has been

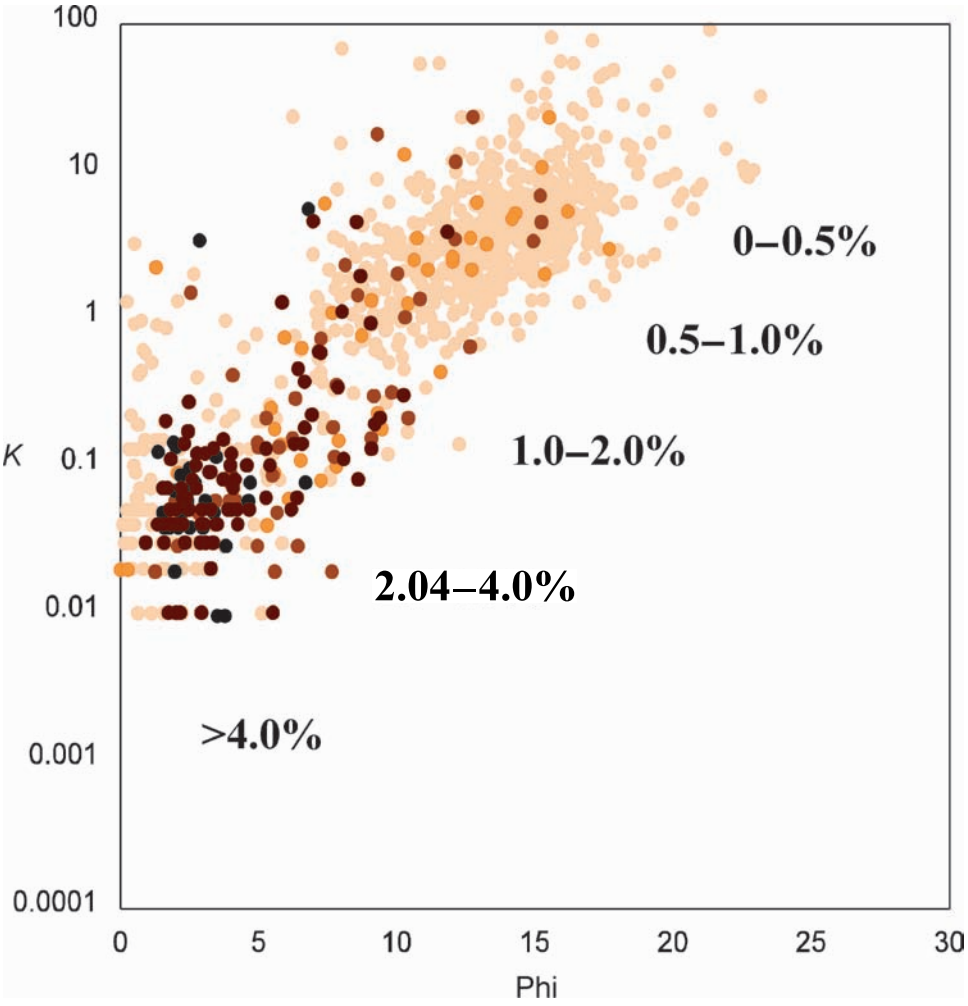

FIGURE 25. Influence of bitumen volume on the porosity (PHI) versus permeability (*K*) relationship in well T-220 (no such data are yet available for T-6246). Increasing bitumen content is negatively correlated with K-Phi above a certain threshold of about 0.5% rock volume. Although bitumen is common in grainy facies with matrix pore types, it also occurs with late secondary pore types like vugs indicative of dissolution as well as with nonmatrix pore types like fracture porosity. See text for discussion.

reported as a major reservoir porosity generation mechanism in, at least, several other carbonate fields (Moore, 2001; Esteban and Taberner, 2003; Zampetti et al., 2003; Sattler et al., 2004). Most of these authors suggest corrosion by mixing of formation fluids with an external fluid at higher temperatures, and such process may be responsible for the burial corrosion in the Tengiz central platform as well. Similarly, the corrosion event postdating the bitumen invasion (and cementation) may represent yet another such leaching phase with different fluids. Fluid-inclusion and stable isotope studies will shed light on the origin of the substantial burial corrosion at Tengiz; see Collins et al. (2006) for discussion of preliminary geochemical data and a probable dissolution model.

Recrystallization is also an important process in the central platform diagenesis. As an example, Figure 29D is a grainstone that was recrystallized to equant and blocky spar. This recrystallization followed early partial cementation of interparticle porosity and was, in turn, followed by late dissolution that produced moldic porosity. Note that early moldic porosity was occluded by blocky calcite (see micrite envelope), whereas this later dissolution phase generated the open molds that are lined by bitumen. More common are finely recrystallized fabrics associated with intercrystalline and minor moldic porosity, as well as the presence of scattered bitumen (Figure 29E, F). Although the recrystallization phase seems to postdate (corrode and truncate) blocky calcite cementation, the exact timing remains unclear because of the destructive nature of the process.

The important diagenetic overprint in the Tengiz central platform as outlined in Figure 27 can be summarized as follows. Syn- and postdepositional dissolution in meteoric environments generated moldic, enlarged interparticle and intraparticle, and microporosity pore types, as well as vuggy microkarst. Cementation of lagoonal intervals associated with the presence of discrete and dispersed volcanic ash significantly reduced porosity and created permeability baffles around cycle and sequence boundaries. Intermediate shallow burial produced commonly observed fitted fabrics and low- to medium-amplitude stylolites. The lateral continuity and persistence of tight layers around sequence and cycle boundaries as well as in local high-energy intervals probably greatly affected later fluid flow and, thus, the ultimate distribution of cements, dissolution, and bitumen in the central platform reservoir. The late diagenetic overprint was responsible for the enhanced dissolution, increasing any existing

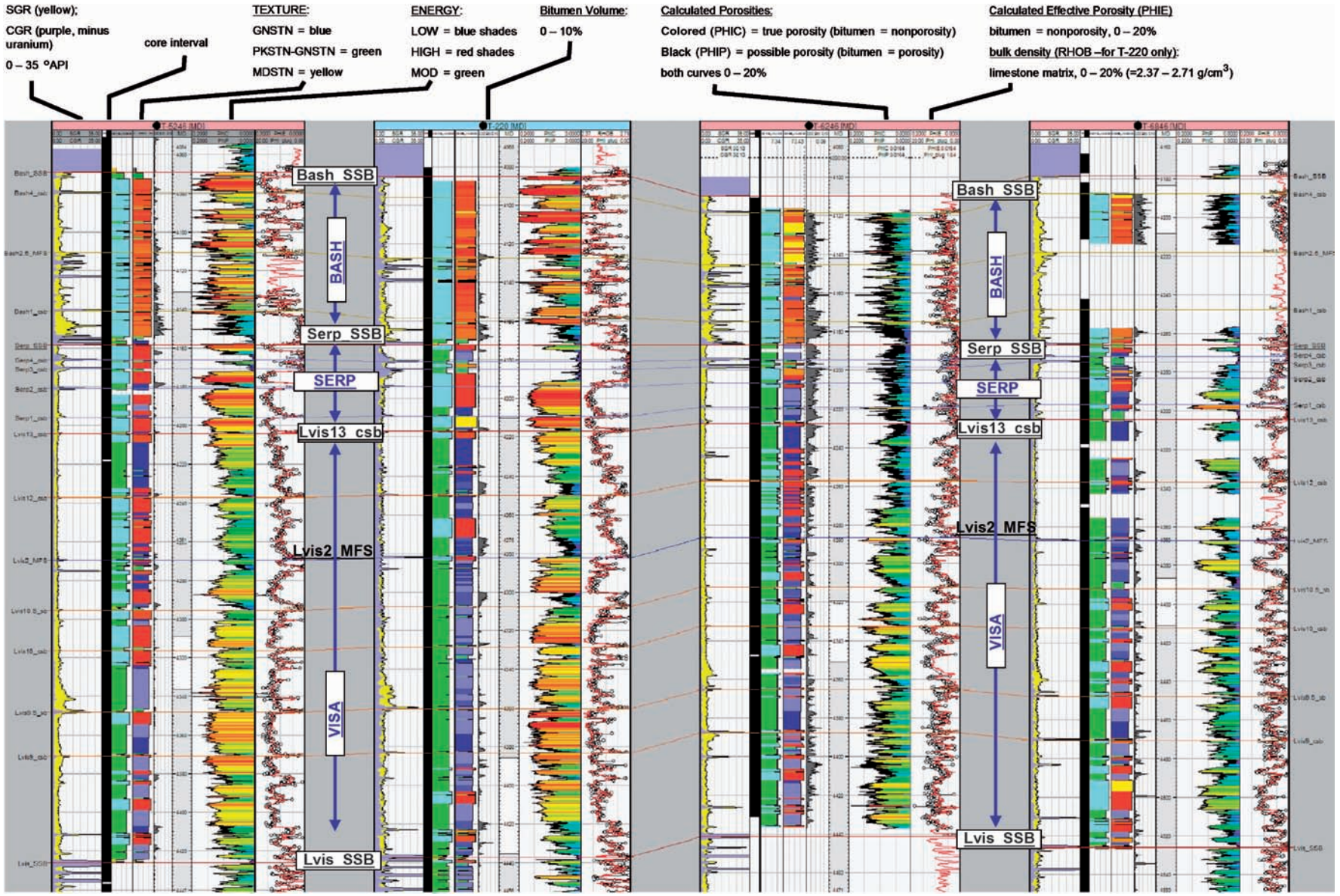

FIGURE 26. Subtle but significant differences in petrophysical and geological properties are observed between these four wells in the central platform (see Figure 4 for well locations and Figure 5 for additional correlations). K-Phi plots and porosity histograms suggest different behavior between northern central platform wells (T-220 and T-5246) and southern central platform wells (T-6246 and T-6846), with generally lower mean porosities and better behaved permeability-porosity relationships in the southern wells and bimodal porosity distributions in the northern wells. Bash = Bashkirian; Serp = Serpukhovian; VisA = Visean A. See text for further discussion.

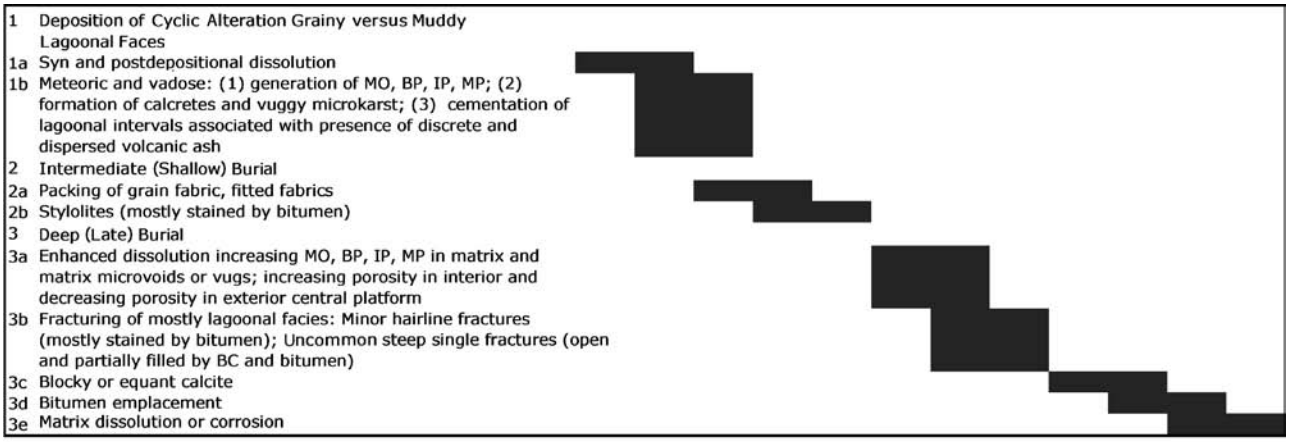

Porosity Creation Events

1b Meteoric and vadose dissolution below parasequence and sequence boundaries

3a Late-burial enhanced dissolution affecting BP, MO, MP, and MVUG but depending on primary fabric and early pore networks — thereby following primary facies distribution

3e Late-burial postbitumen emplacement matrix dissolution or corrosion

Porosity Reduction Events

1 Trapping of volcanic ash in discrete layers and as dispersed agent is associated with elevated cementation calcite and silica) — both in low-energy and moderate high-energy environment of deposition and not clear spatial distribution

3c Blocky or equant calcite

3d Emplacement of bitumen related to generation of pore network of contemporanous and/or earlier matrix and fracture dissolution thereby following primary facies distribution

FIGURE 27. Paragenetic sequence for the central platform. Significant syndepositional, intermediate (shallow)-burial, and deep (late)-burial events are listed in chronological order. In the lower part of the figure, those events that are particularly important to porosity creation and destruction are listed. MO = moldic; BP = interparticle; IP = intraparticle; MP = microporosity; MVUG = micro vug. See text for discussion.

porosity in the matrix and forming vugs and minor fractures, whereas equant calcite cement reduced porosity away from the interior central platform. The subsequent bitumen invasion exerted an overall porosity-reducing effect increasing toward the outer platform. These late-burial events that increased and reduced porosity significantly dampened or flattened initial vertical, nearly cyclic, porosity variations linked to primary depositional properties.

Spatial Distribution of Central Platform Reservoir Quality

In the absence of any significant first-order control by pore type or lithofacies, the following sections describe the reservoir quality in the context of the transition from central to outer platform environments. This lateral change is likely a result of the early cyclic depositional and diagenetic processes, including the preservation of volcanic ash, coupled with late-burial dissolution and bitumen emplacement.

Figure 30 presents a model that summarizes porosity generation and reduction events in the central Tengiz platform from the standpoint of gamma-ray and porosity logs. Porosity changes are linked to the major diagenetic phases following deposition of alternating thin, low-energy lagoonal intervals with volcanic ash beds and thick intervals of high-energy grainstone. Detailed log and core correlation shows that lagoonal interval and ash beds are not always associated and/or continuous between well locations, and cycles may vary slightly in thickness over kilometers distance. Three important diagenetic stages that affect the reservoir quality and distribution are observed. First, porosity curves with a blocky shape are the result of early-burial processes, including low porosity around cycle boundaries related to the presence of thin ash beds and corrosion and cementation related to meteoric diagenesis (Figure 30A). Locally thick grainstone intervals have low porosity and show the presence of elevated levels of dispersed ash concentrated in frequent stylolites. Second, a

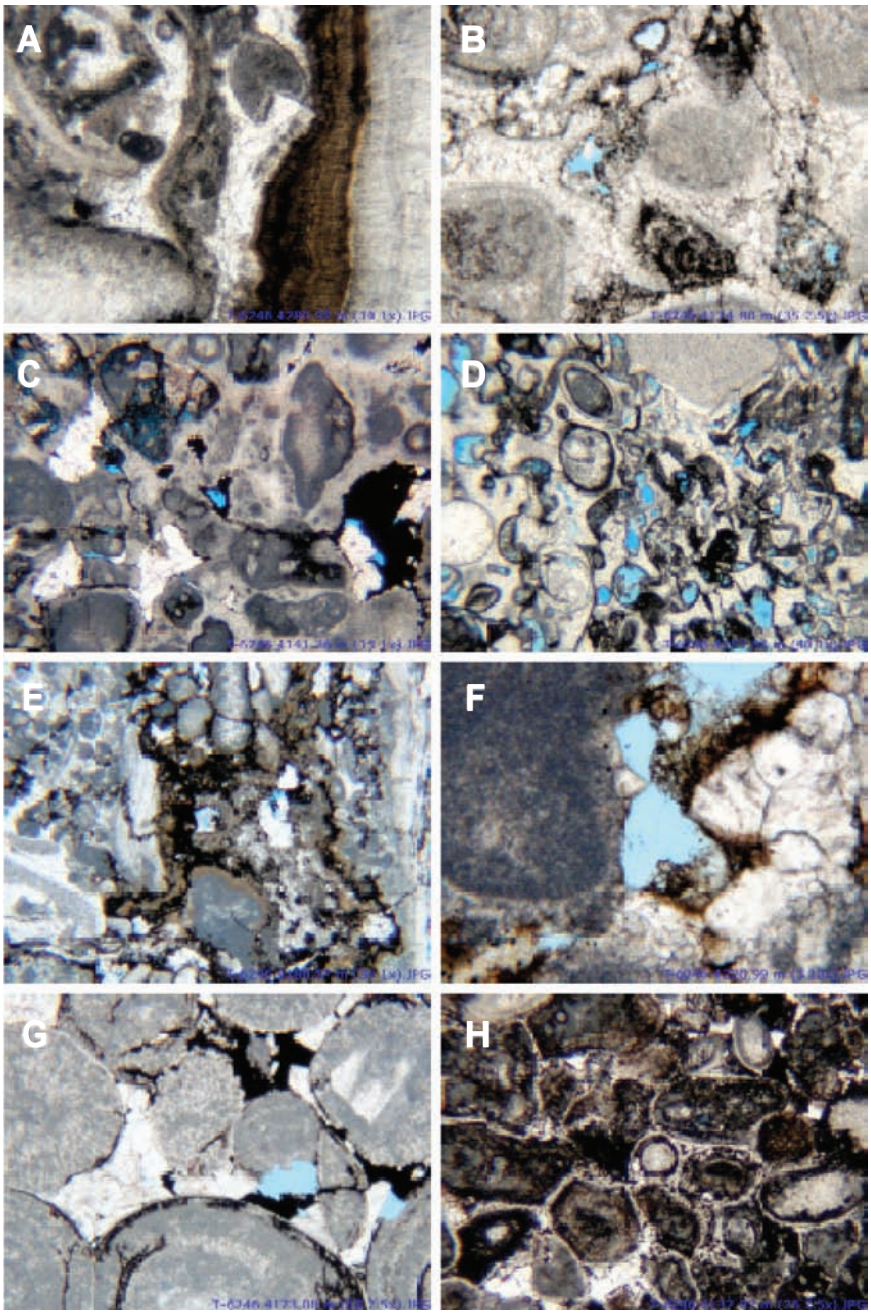

FIGURE 28. Photomicrographs illustrating some of the dominant cement types in the central platform area. (A, top to the right) Brown fibrous pendant cement attached to lower part of brachiopod fragments is interpreted as the result of meteoric diagenesis and, therefore, suggests subaerial exposure above. (B) Mycrostalactitic or pendant cements, which are commonly associated with vadose diagenesis, are observed to several meters below a suspect exposure surface. (C, D) Meniscus and pendant cements, indicating vadose to marine vadose diagenesis occlude much of the primary porosity in these samples. Burial dissolution and/or corrosion of preserved interparticle porosity are followed by blocky calcite cement and bitumen. (E) Possible example of alveolar fabrics indicating soil formation below exposure surface. (F) Possible vadose cementation followed by enhanced corrosion or dissolution of grain boundaries and cement, blocky calcite cement, and bitumen. (G, H) A combination of minor cementation and compaction leads to fitted fabrics or overpacked fabrics. Here, a thin cement rim is included in the compaction process and followed by burial blocky calcite spar cement and bitumen. Width of photomicrographs is 4.20 mm (0.16 in.) (A, C, D, E, F) and 1.58 mm (0.06 in.) (B, G, H). See text for discussion.

burial event led to corrosion and enhanced blocky porosity curves in the interior central platform and porosity reduction in the exterior central platform; alternatively, corrosion in the exterior central platform was lower compared to the interior central platform (Figure 30B). Finally, bitumen that was emplaced during a late-burial event acts as cement and reduces porosity (Figure 30C). Bitumen volume increases from the interior to the exterior central platform and margin and obscures correlation using the porosity curves. Some evidence suggests that another corrosion phase is associated with the bitumen emplacement; in the rim and flank area, observations indicate a corrosion event following the bitumen cement (Collins et. al., 2006).

Packstone to mudstone intervals around the cycle boundaries in the central platform wells typically display significantly lower porosity and permeability relative to the overlying grainstone-packstone lithofacies (Figure 31, sequences between Lvis10.5_csb-Lvis9.5_csb in wells T-5246 and T-220). The latter have porosity ranges between 0 and 24% with a mean of 10.5 and 11.0% (Table 2). The packstone to mudstone intervals are generally associated with gamma-ray spikes caused by the presence of volcanic ash and are generally tight with a mean porosity of 3.5%. Within the central platform, the cyclic signature of alternating blocky high-porosity and low-porosity zones associated with gamma-ray spikes is dominant. Lateral and

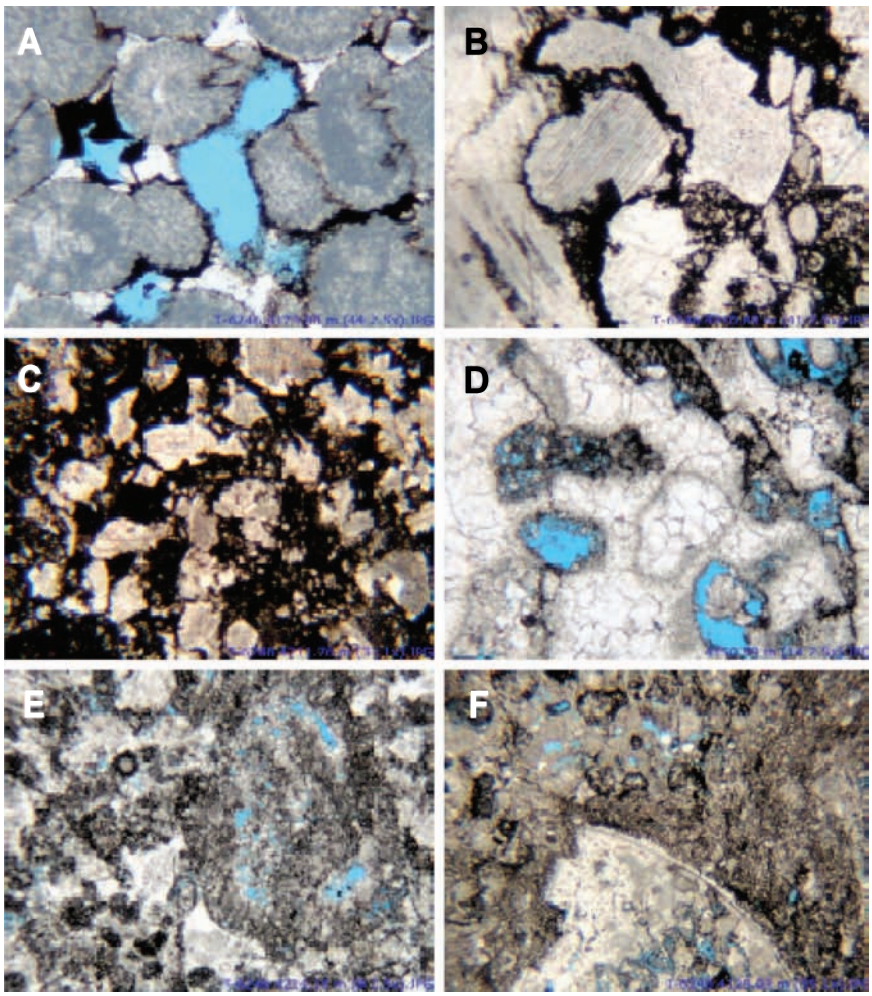

FIGURE 29. **Photomicrographs illustrating additional pore types of the central platform area. (A) Enhanced late-burial(?) dissolution joining interparticle pores into larger vugs prior to bitumen lining the pore walls. The primary grain boundaries appear to have been corroded by the dissolution. In addition, following bitumen emplacement, grains were partially dissolved by an additional dissolution event. (B) Bitumen corroding both the crinoid ossicle boundaries as well as those of the syntaxial overgrowth cement. (C) As in (B), but advanced stage of bitumen emplacement corroding grain boundaries and leading to pseudopackstone to wackestone fabric. (D) Recrystallization is a dominant process in the central platform diagenesis. Here, an example where the grainstone fabric was recrystallized to equant and blocky spar following early partial cementation of interparticle porosity and followed by late dissolution generating the moldic porosity. Note that early moldic porosity was occluded by blocky calcite (see micrite envelop), whereas a later dissolution phase generated the open molds that are lined by bitumen. (E, F) Finely recrystallized fabrics associated with intercrystalline and minor moldic porosity, as well as the presence of scattered bitumen, are very common in the central platform. Although the recrystallization phase seems to postdate (corrode and truncate) blocky calcite cementation, the exact timing remains unclear because of the destructive nature of the process. Width of photomicrographs is 4.20 mm (0.16 in.) (C, F) and 1.58 mm (0.06 in.) (A, B, D, E). See text for discussion.**

vertical changes in distribution and type of the intermediate grainstone to packstone lithofacies have only a minor effect on the present-day porosity. The interval on Figure 31 in well T-5246 represents high-energy grainstone, and although the interval in well T-220 is lower energy packstone-grainstone facies, no visible difference is observed on the porosity log.

A remarkable deviation in the central platform occurs in the lower part of the Bash1_csb, where mostly well-sorted ooid grainstone is invaded and cemented by bitumen all across the platform. The resulting porosity range is 0–10%, with a mean of 4%, whereas in bitumen-poor ooid grainstone, the porosity ranges between 0 and 21%, with a mean of 12% (Table 2). The fact that bitumen (as much as 3.5%

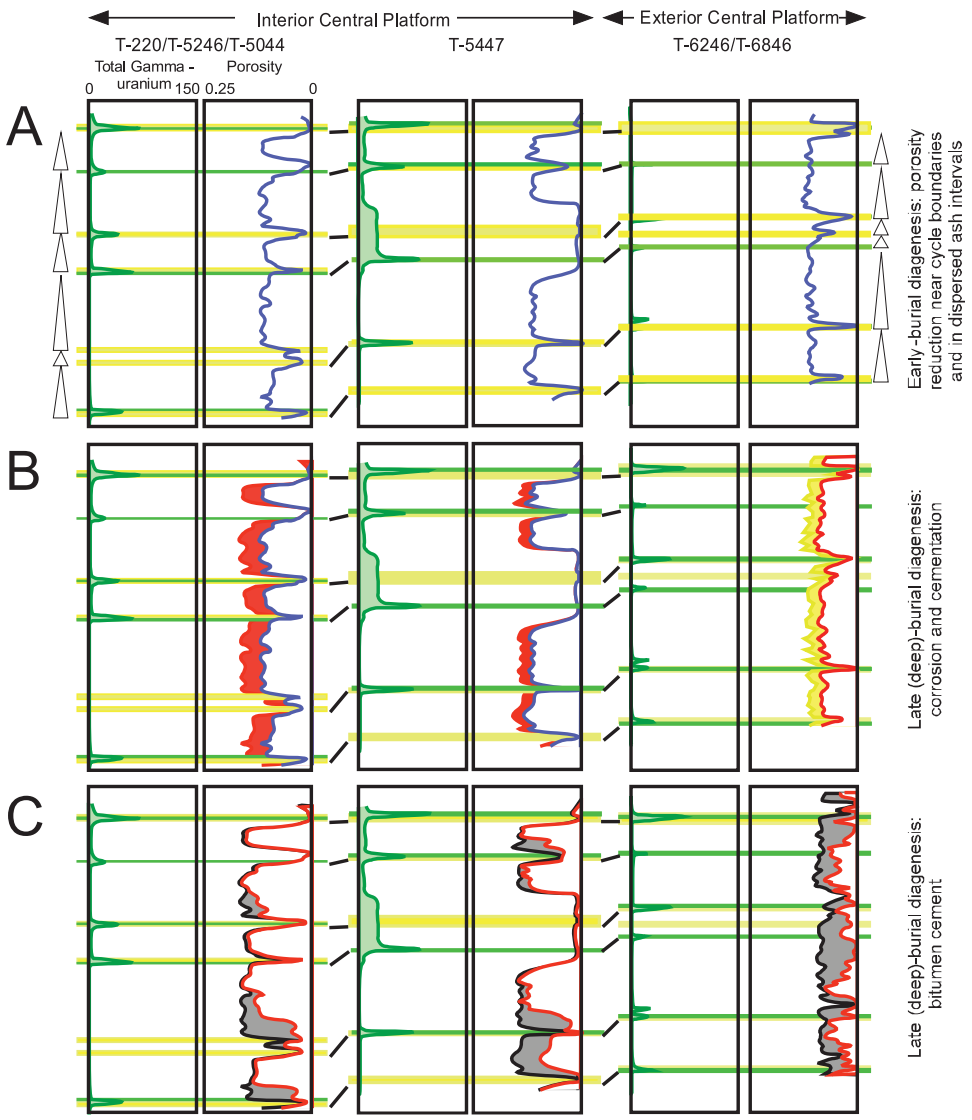

FIGURE 30. Hypothetical log correlation scenarios in the central platform, with gamma ray shown on the left and porosity on the right for each well(s). Porosity generation and reduction events that are linked to the major diagenetic phases are indicated for a stratigraphy that includes thin, low-energy lagoonal intervals alternating with volcanic ash beds (yellow and green horizons) and thick intervals of high-energy grainstone (white). Detailed correlation shows that lagoonal intervals and ash beds are not always associated and/or continuous between well locations, and cycles (triangles) may vary slightly in thickness over kilometers distance. (A) Porosity curves with a blocky shape are the result of early-burial processes, including porosity loss around cycle boundaries related to the presence of thin ash beds and corrosion and cementation related to meteoric diagenesis (porosity is blue). Locally thick grainstone intervals have low porosity and show the presence of elevated levels of dispersed ash concentrated in frequent stylolites. (B) Late-burial events leading to corrosion and enhanced blocky porosity curves in interior central platform (red) and porosity reduction in the exterior central platform (yellow); alternatively, corrosion in the exterior central platform was lower compared to the interior central platform. (C) Bitumen, which is emplaced during late burial, acts as cement and reduces porosity. Bitumen volume increases from the interior to the exterior central platform and margin and obscures correlation using the porosity curves.

rock volume) invaded this far into the central platform may be related to the continuous underlying pressure baffle, at the Serp_SSB, which preexisted prior to the bitumen and associated dissolution phase (Figure 32A).

Bitumen occurs within fine matrix and as a pore-filling phase, and two spatial trends are observed (see Figure 5, 25): (1) a general increase from exterior to interior central platform wells and (2) elevated bitumen levels near the base of grainy facies between

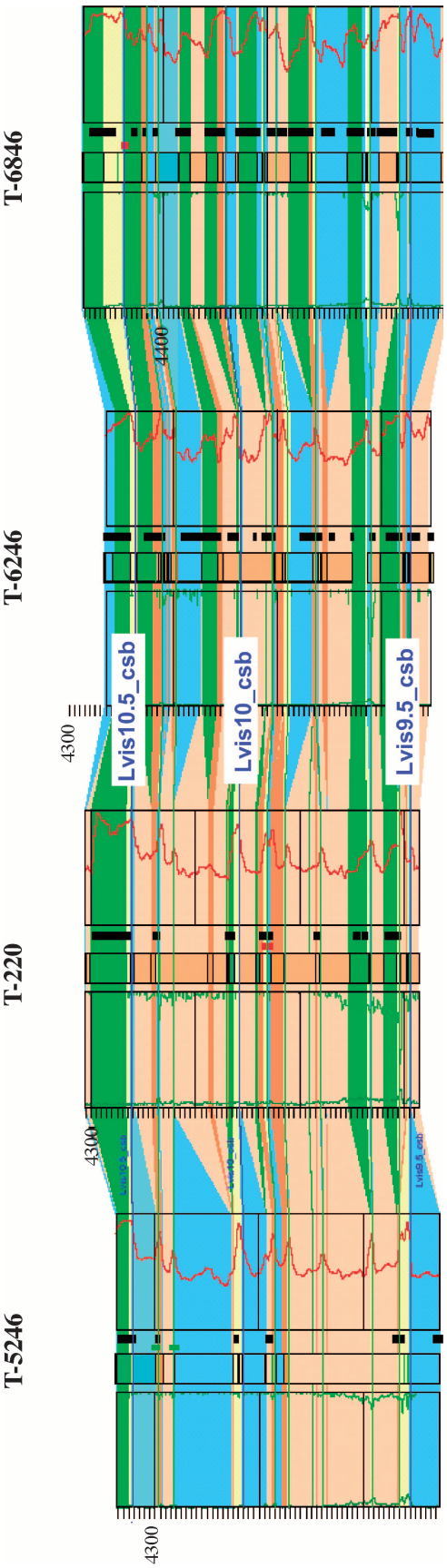

FIGURE 31. Cross section showing lithofacies, gamma-ray (left), and porosity (right) logs; well locations are shown in Figure 4, and lithofacies legend is shown in Figure 5. The lateral facies and thickness continuity of the sequences between Lvis10.5_csb and Lvis9.5_csb are shown between the T-5246, T-220, T-6246, and T-6846 wells. The cyclic and blocky high-low porosity character is visible in nearly bitumen-free wells (T-5246 and T-220) and represents, respectively, alternating grainy facies and lagoonal mud intervals with volcanic ash. Although the interval in T-5246 represents high-energy and essentially mud-free grainstone, and that in T-220 is lower energy and packstone-grainstone facies, no visible difference is observed on the porosity log. See text for discussion.

tight lagoonal intervals. In addition, some ooid grainstone (right above the Serp_SSB) and crinoid grainstone-packstone intervals (mostly between the Lvis_SSB and Serp_SSB) show increased bitumen content all across the central platform. The late timing of bitumen relative to other diagenetic overprint suggests the introduction through the flanks and into the platform part of the Tengiz buildup, with the largest lateral extent in the most permeable units and residual deposition controlled by gravity, that is, on top of the immediate underlying impermeable cycle boundary (see also Figure 26). Additional intervals with elevated bitumen extend to T-220 but disappear upsection and in the direction of T-5246 (Figures 5, 32B).

In the north (well T-5044) and southwest (wells T-6246 and T-6846) parts of the central platform, overall bitumen content in the Lvis_SSB to Bash_SSB grainy facies reduces porosities to a mean of 5.8–7.6%, which is significantly reduced from the 10.6–11.2% recorded in well T-220 (Figure 5). In general, increased bitumen content is commonly confined to the lower part of a cycle. The bitumen-cemented interval exhibits a sharp, lower contact with underlying, well-cemented peloid packstone-wackestone lithofacies, has a gradational upper contact, and appears dark gray to black in core. Although the blocky log character changes to a more irregular and spiky shape with increasing bitumen content, no obvious relationship exists between the amount of porosity reduction and primary lithofacies type. Instead, the presence of the tight peloid packstone-wackestone baffles seems to control the occurrences of bitumen-cemented interval (see Figures 31, and 33, well T-220 versus well T-6246, no bitumen but lateral facies change). The bitumen effect progressively increases away from the platform center and, at the scale of the plug sample, reduces the porosity and permeability as suggested by the relationship shown in Figure 24.

In addition to porosity and permeability reduction by bitumen and volcanic ash layers, the presence of dispersed volcanic ash in high-energy grainstone facies locally also has an effect (Figure 34). Volcanic ash dispersed in the well-sorted skeletal grainstone and coated-grain grainstone-rudstone lithofacies of the Serp1_csb sequence at well T-5447 reduces porosity to nearly zero and generates a nearly flat porosity curve, whereas the same facies interval at well T-220 retains high porosity. Similarly, the tight and laterally continuous interval associated with the Serp_SSB is probably also associated with elevated levels of dispersed volcanic ash (see Figure 5).

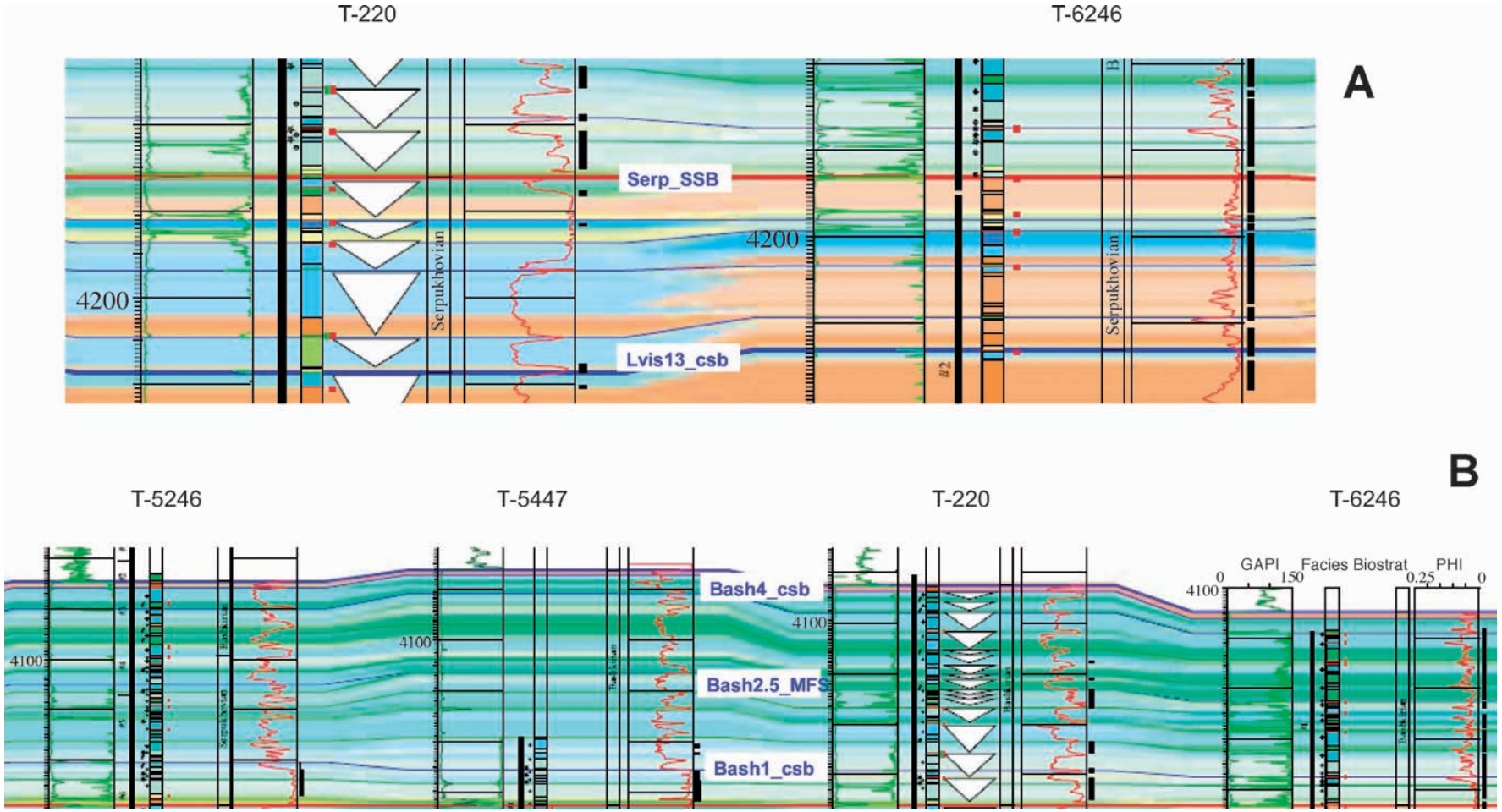

FIGURE 32. Cross sections showing lithofacies, gamma-ray (left), and porosity (right) logs; well locations are shown in Figure 4, and lithofacies legend is shown in Figure 5. The lateral facies and thickness continuity of sequences between the Serp_SSB and Lvis13_csb are shown for the T-220 and T-6246 wells in (A) and between the Bash2.5_MFS to Bash4_csb for the T-5246, T-5447, T-220, and T-6246 wells in (B). The lower part of the Bash1_csb, mostly well-sorted ooid grainstone (OG), is invaded and cemented by bitumen all across the platform. Additional intervals with elevated bitumen extend to T-220 but disappear upsection and toward T-5246. See text for discussion.

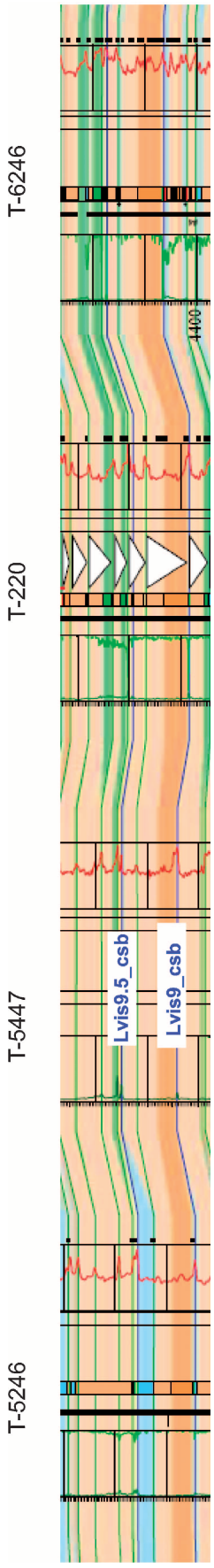

FIGURE 33. Cross section showing lithofacies, gamma-ray (left), and porosity (right) logs; well locations are shown in Figure 4, and lithofacies legend is shown in Figure 5. The lateral facies and thickness continuity of sequence Lvis9.5_csb to Lvis9_csb are shown for wells T-5246, T-5447, T-220, and T-6246. Toward the southwestern (interpreted as outer platform) margin and away from the central platform to the north (T-5044), overall bitumen in the Lvis_SSB to Bash_SSB section increases (as much as 2–4% rock volume bitumen in some parts of T-6246), and generally, elevated levels of bitumen are commonly confined to the lower part of the cycle. See text for discussion.

IMPLICATIONS FOR RESERVOIR MODELING

The stratigraphic framework introduced for the central platform part of the Tengiz buildup in the preceding sections is the basis for the layering scheme that is being used in reservoir models for the field. Full-field models use the layering portrayed on Figure 4, whereas more detailed models focusing on parts of the platform incorporate more detailed layers as shown in Figures 5 and 25. The lithofacies summarized in Table 2 have been grouped and used to subdivide layers in the reservoir models into regions where porosity and permeability might be expected to vary. The complex diagenesis that occurs in the central platform and the outer platform has overprinted the original (depositional) porosity to an extent, as summarized in Figure 30, that it cannot be ignored when trying to interpret reservoir quality from wire-line logs and correlate it within a reservoir model. Ongoing studies of the detailed analysis of the types and amounts of porosity, as well as pore-filling agents are being used to better understand the log signatures of porosity and improve porosity-permeability transforms. Much work remains in the detailed characterization of the Tengiz reservoir and in correctly portraying the significant geologic characteristics of the Tengiz platform in reservoir models.

SUMMARY AND CONCLUSIONS

An integrated (and ongoing) study of core, well logs, and discrete petrophysical measurements provided a first comprehensive assessment of depositional evolution and reservoir quality in the late Visean to Bashkirian interval in the Tengiz central platform. The study resulted in the following observations and tentative conclusions.

Depositional cycles (=higher frequency sequences) are up several to tens of meters in thickness and made up of a succession of lithofacies overlying a sharp base with variable evidence for subaerial exposure. At the base of the cycles, tight peloidal mudstone and volcanic ash beds are associated with sequence boundaries and represent flooding events. They are overlain by brachiopod- and crinoid-dominated intervals that represent maximum marine flooding and near the top by skeletal-peloidal grainstone that are interpreted as the highstand-shoaling phase. Nonskeletal grainstones are most common in the Bashkirian. Visean and Serpukhovian cycles are generally easy to correlate laterally, whereas Bashkirian cycles are best explained by the transition to high-frequency icehouse sea level

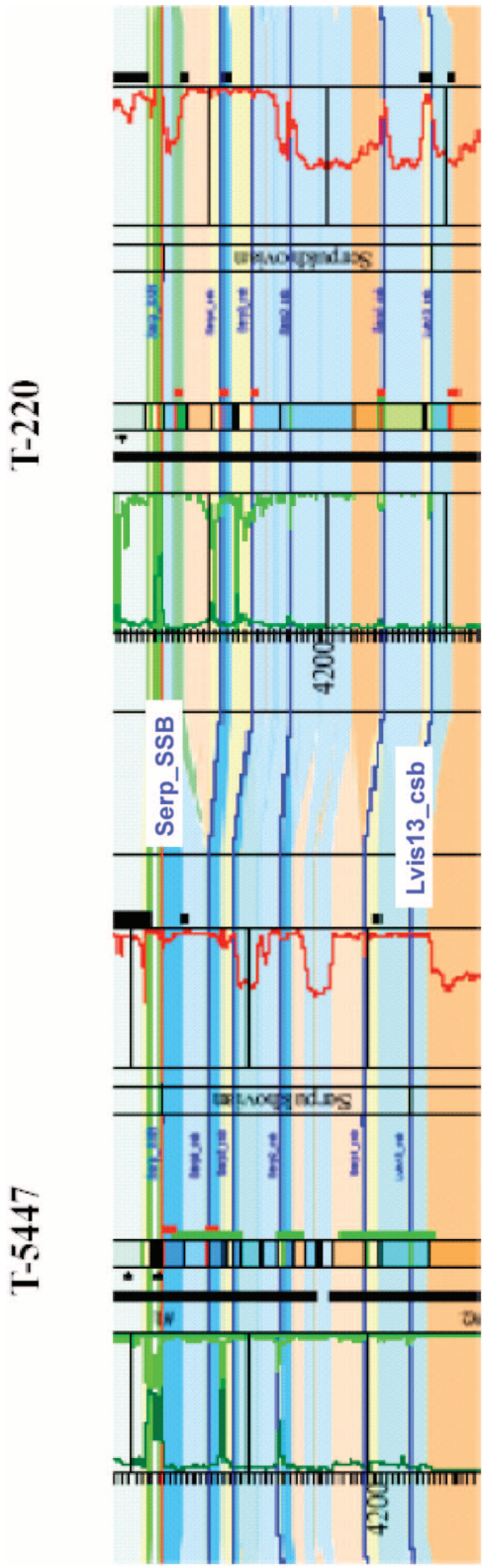

FIGURE 34. Cross section showing lithofacies, gamma-ray (left), and porosity (right) logs; well locations are shown in Figure 4, and lithofacies legend is shown in Figure 5. The lateral facies and thickness continuity of sequences between Serp_SSB and Lvis13_csb are shown for wells T-5447 and T-220. In addition to bitumen-reducing porosity, dispersed volcanic ash in high-energy grainstone facies locally has an even greater effect on porosity in the central platform. Volcanic ash dispersed in the SPG and CgPR lithofacies in the Serp1_csb sequence at T-5447 reduces porosity to nearly 0%, generating a flat porosity curve, whereas the same facies interval at T-220 retained high porosity. See text for discussion.

fluctuations, which generate incomplete cycles and complex lateral facies changes.

The distribution of reservoir quality in the central platform was initially determined by early diagenesis associated with cyclic deposition, which resulted in a stacked system of high-porosity intervals bordered by tight higher order sequence boundaries with reduced dissolution associated with the presence of volcanic ash. This diagenetic phase includes low-porosity, thick (discontinuous and not platformwide) grainstone intervals with high amounts of dispersed volcanic ash. The lateral continuity of tight cycle boundaries probably greatly affected later fluid flow as well as the ultimate distribution of cements, dissolution, and bitumen in the central platform reservoir. Burial diagenetic overprint, an initial corrosion phase followed by a pore-filling phase, and finally, bitumen invasion and associated corrosion, produced an overall porosity reduction toward the exterior central platform. Bitumen content decreases from the exterior to the central platform and is highest near the bases of the cycles. This suggests that the first fill of hydrocarbons migrated through the flanks laterally into the platform cycles. Both corrosion and bitumen emplacement flattened the initial cyclic porosity variations and further complicated porosity and permeability relationships.

ACKNOWLEDGMENTS

The authors thank the following individuals, who provided insightful comments or suggestions and, in some cases, data to greatly improve this manuscript. Perhaps most importantly, Michael Clark (Chevron) is thanked for initiating an intense coring and core analysis program that formed the basis for most of our geologic studies and for his strong support of the sequence-stratigraphic framework. Ben Robertson (Chevron) provided important discussion during the continued coring program and supporting geological analyses of outcrop analogs and literature reviews. Numerous coworkers in Chevron, ExxonMobil, and TengizChevroil assisted with our core and log studies and participated in lively discussions on many topics. Giovanna Della Porta (Cardiff University) and Frans van Hoeflaken (independent consultant) are acknowledged for critically reviewing the petrographic and lithofacies descriptions. Steve Jenkins (TengizChevroil) offered numerous comments and observations, which tested the ideas expressed in this study in their practical application for three-dimensional

geologic modeling of the Tengiz platform. Comments by AAPG reviewers helped to greatly improve the manuscript. Finally, we thank TengizChevroil and its shareholder companies (Chevron, ExxonMobil, Kazmunaigaz, and BPLukArco) for permission to publish this study.

REFERENCES CITED

Brenckle, P. L., and N. V. Milkina, 2001, Foraminiferal timing of carbonate deposition on the Mississippian–early Pennsylvanian Tengiz platform, Kazakhstan: Paleoforams 2001— International Conference on Paleozoic Benthic Foraminifera, Abstracts, Ankara, August 20–24, p. 2001.

Choquette, P. W., and L. C. Pray, 1970, Geologic nomenclature and classification of porosity in sedimentary carbonates: AAPG Bulletin, v. 54, p. 207–250.

Collins, J. F., J. A. M. Kenter, P. M. Harris, G. Kuanysheva, D. J. Fischer, and K. L. Steffen, 2006, Facies and reservoir-quality variations in the late Visean to Bashkirian outer platform, rim, and flank of the Tengiz buildup, Precaspian Basin, Kazakhstan, *in* P. M. Harris and L. J. Weber, eds., Giant hydrocarbon reservoirs of the world: From rocks to reservoir chacracterization and modeling: AAPG Memoir 88/SEPM Special Publication, p. 55–95.

Cook, H. E., W. G. Zempolich, V. G. Zhemchuzhnikov, and J. J. Corboy, 1997, Inside Kazakstan: Cooperative oil and gas research: Geotimes, v. 42, no. 11, p. 16–20.

Esteban, M., and C. Taberner, 2003, Secondary porosity development during late burial in carbonate reservoirs as a result of mixing and/or cooling of brines: Journal of Geochemical Exploration, v. 78–79, p. 355–359.

Gradstein, F. M., J. G. Ogg, and A. G. Smith, 2004, A geologic time scale: International Commission on Stratigraphy (ICS) under: www.stratigraphy.org.

Lucia, F. J., 1995, Rock-fabric/petrophysical classification of carbonate pore space for reservoir characterization: AAPG Bulletin, v. 79, p. 1275–1300.

Lucia, F. J., 1999, Carbonate reservoir characterization: New York, Springer-Verlag, 222 p.

Moore, C. H., 2001, Carbonate reservoir-porosity evolution and diagenesis in a sequence stratigraphic framework: Developments in Sedimentology, v. 55, p. 444.

Ross, C. A., and J. R. P. Ross, 1985, Carboniferous and Early Permian biogeography: Geology, v. 13, p. 27–30.

Sattler, U., V. Zampetti, W. Schlager, and A. Immenhauser, 2004, Late leaching under deep burial conditions: A case study from Miocene Zhujiang carbonate reservoir: South China Sea: Marine and Petroleum Geology, v. 21, p. 977–992.

Weber, L. J., B. P. Francis, P. M. Harris, and M. Clark, 2003, Stratigraphy, lithofacies, and reservoir distribution, Tengiz field, Kazakhstan *in* W. M. Ahr, P. M. Harris, W. A. Morgan, and I. D. Somerville, eds., Permo-Carboniferous carbonate platforms and reefs: SEPM Special Publication 78 and AAPG Memoir 83, p. 351–394.

Zampetti, V., W. Schlager, J. H. Van Konijnenburg, and A. J. Everts, 2003, Architecture and growth history of a Miocene carbonate platform from 3D reflection data: Luconia Province, offshore Sarawak, Malaysia: Marine and Petroleum Geology, v. 21, p. 517–534.